Three-Dimensional Imaging of the Solid-Liquid Interface with High-Resolution Atomic Force Microscopy

Dissertation zur Erlangung des Grades

"Doktor der Naturwissenschaften"
im Promotionsfach Chemie

am Fachbereich Chemie, Pharmazie und Geowissenschaften
der Johannes Gutenberg-Universität Mainz

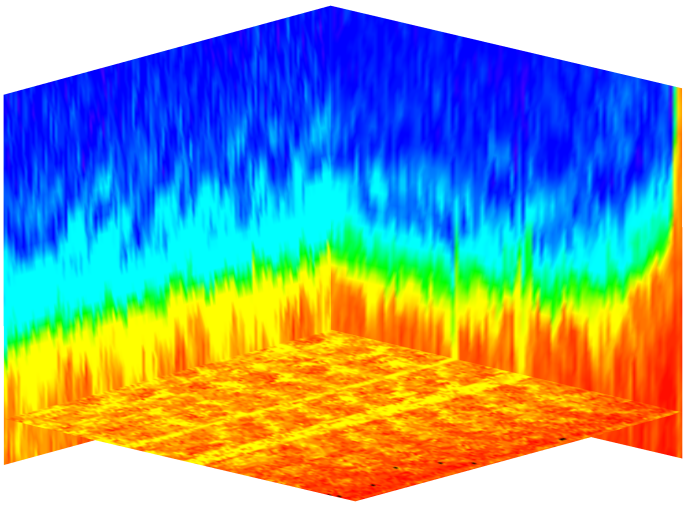

Christoph Peter Marutschke

geboren in Offenbach am Main

Mainz, den 05. November 2015

This dissertation was supervised by [redacted] and was carried out at the Johannes Gutenberg-Universität Mainz from March 2012 to November 2015.

D77 (Dissertation Johannes Gutenberg-Universität Mainz)

Dean of the faculty	[redacted]
1st report	[redacted]
	Johannes Gutenberg-Universität Mainz
2nd report	[redacted]
	Max-Planck-Institut für Polymerforschung
Submitted:	05.11.2015
Oral examination:	08.12.2015

Contents

Dieser Keks wird kein weicher sein ...
Otto Waalkes

1 Introduction and Motivation

In this dissertation the implementation of a three-dimensional (3D) atomic force microscopy (AFM) mapping routine is demonstrated. Subsequently, this 3D technique is employed for investigating the solid-liquid interface. The development of high-resolution *in-situ* AFM is subject to many difficulties and is still a relatively young discipline within surface science [1]. Constant improvements in the AFM instrumentation have pushed the high-resolution capabilities of AFM to achieve true atomic resolution in liquid environments [2, 3]. This level of resolution is required to investigate the most important and basic questions concerning the solid-liquid interface at the atomic scale. While standard AFM imaging provides lateral information, exclusively 3D mapping can reveal the entire, distance-dependent information of the interaction between the surface, the interfacial solvent molecules and other (organic) molecules. Consequently, 3D mapping with the AFM is the best choice for direct imaging of water molecules above a surface and is the method used in this work (introduced in chap. 2).

In chap. 3, I report about the successful implementation of a 3D data acquisition routine using a commercial AFM. To meet the interest and demands of a large scientific community, the emphasis in the development was on an easy-to-use operability based on the amplitude modulated (AM) mode, which allows for reliable data acquisition at high scan speeds. The performance of this mapping routine is demonstrated by presenting 3D maps of the hydration layers at the solid-liquid interface on the most stable cleavage plane of calcite [4]. Furthermore, common difficulties in high-resolution amplitude modulation atomic force microscopy (AM-AFM) mapping, such as the “forest of peaks”, the determination of the surface position and hysteresis are addressed in detail.

The precise description of the solvent molecules’ arrangement at the interfaces is the key to understanding fundamental reactions at the solid-water interface. Depending on the specific surface and solvent properties, the presence of a surface often induces an ordered arrangement of the interfacial water as compared to bulk water. When considering interfacial processes, natural carbonates are of major importance since they are highly abundant in nature. Among them, calcite is the most thoroughly studied mineral which is relevant in numerous fields, such as biomineralization [5] and geochemistry [6]. The related minerals dolomite and magnesite exhibit the same crystal structure as calcite, but differ in their cation composition. This results in slightly different lattice constants of the unit cell on their most stable cleavage plane, providing an ideal model system to systematically study the influence of the lattice

constant on the arrangement of interfacial water molecules. In chap. 4, the herein implemented 3D routine is used for high-resolution 3D mapping on all three carbonates. The experimental data allow for the identification of the structure of the hydration layers above all three carbonates, and for the influence of different lattice parameters on the observed structures.

Most studies in the field of hydration layer mapping have only focused on water on pristine surfaces, and comparatively little is known about the arrangement of other solvent molecules. In chap. 5 a study is presented, which addresses the arrangement of other simple solvent molecules on the (10.4) surface of calcite by means of 3D mapping. Three linear alcohols, namely, methanol, ethanol and propan-1-ol are chosen as model systems to study the interaction of organic/bio- molecules, which often contain hydroxyl groups (-OH) and hydrophobic functionalities [7, 8].

Alongside the investigation of direct solvent-mineral interactions, two minor topics haven been examined in this thesis. In chap. 6 the interesting example of the molecular structure formation of the Alizarin Red S (ARS) molecule at the surface of calcite is studied. The understanding of the complex interactions between organic additives, surface and solvent molecules is the next logical step to explore natural processes, and first results obtained with standard AM-AFM imaging and 3D mapping at the water-calcite interface in the presence of ARS molecules are shown. In chap. 7, a particularly challenging sample system, namely lithium niobate (LN) has been studied by frequency modulation atomic force microscopy (FM-AFM) mapping in the group of [redacted] at the Kyoto University in Japan. Here, the very basic question of the X-Cut surface interaction with water molecules is explored, and preliminary results obtained with high-resolution FM-AFM imaging and two-dimensional (2D) FM-AFM mapping are presented.

2 The Technique of Atomic Force Microscopy

Binnig and Rohrer were awarded the Nobel Prize for introducing the first scanning probe microscope (SPM) in 1982 [9]. The scanning tunnelling microscope (STM) examines the electronic surface states by applying a bias between a conductive probe and a conductive surface resulting in a measurable tunnelling current. In order to extend the application to non-conducting surfaces, they invented the atomic force microscopy (AFM) [10] and characterised surfaces by monitoring the force acting between the tip of a probe and a surface. Since its introduction, the AFM has become an indispensable tool for surface science as it provides unique, real space information about various surface properties [11]. True atomic resolution has been achieved for many surfaces, first under ultra high vacuum (UHV) conditions [12–14] and later in liquid environments [1, 15–17]. Furthermore, submolecular resolution [18, 19] and chemical identification at the nanoscale [20] have been demonstrated. Even single chemical bonds have been investigated by the combination of different scanning probe microscopy (SPM) techniques [21, 22]. The exploration of molecular structure formation from simple polycyclic aromatic hydrocarbons [23] to complex molecules, such as deoxyribonucleic acid (DNA) [24], has greatly benefited from the use of high-resolution AFM. Furthermore, the field of high-speed AFM has attracted significant attention in the scientific community by capturing biological processes, like protein folding [25, 26].

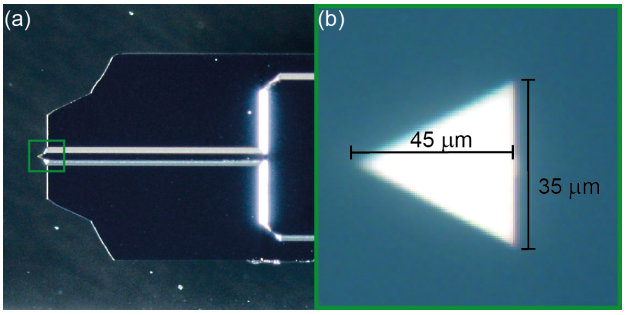

Figure 2.1.: (a) An Arrow UHF cantilever chip from Nanoworld - the small cantilever (within the blue box) is barely visible to the naked eye. The photograph is kindly provided by Robert Lindner. (b) A magnification of the green box - the cantilever imaged from above with the internal camera of the Cypher AFM.

The key element of the AFM is a (sharp) tip at the edge of a probe, which is "sensing" the surface. The sensor design can be made with a variety of options concerning shape, materials and tip functionality. This allows for the most appropriate probe and tip combination to be used in any given experiment [27]. The cantilever, a beam anchored at one end, is the most widespread design for AFM sensors used today. For

example, pictures of the cantilever used in this work are shown in fig. 2.1 ((a) the cantilever chip and the (b) the cantilever). In order to achieve high-resolution with the AFM, especially true atomic-resolution, the tip has to be very sharp; the tip apex should consist of a single atom or a small cluster of atoms [28]. The sample is characterised by scanning the probe above the surface or vice versa, depending on the actual design of the AFM instrument. The stable and precise positioning of the tip in all three dimensions is crucial for the imaging process and realised by piezoelectric elements [29].

Several systems have been developed to detect the manifold interactions between a tip and a surface, such as interferometric [30] and piezo-resistive[31] methods, and self-sensing systems like tuning forks [32]. However, in this work, the most common method- the beam deflection technique- is used [33]. Here, a laser beam is reflected by the back of a cantilever and directed via an optical system to a position sensitive photo diode (PSD) that converts the light into an electrical signal. The PSD has four quadrants to detect horizontal and vertical motions of the cantilever.

The possibility to study samples without complex preparation is a significant advantage of AFM when compared to other tools for "seeing" on the nano scale [34]. It further allows for the study of interesting sample-systems in their natural, often liquid, environments. To perform AFM measurements in liquid, the design of the AFM has to be adopted, e.g., the actuation piezo must be protected in order to prevent a short circuit. Additionally, for the beam deflection detection method, the set-up must allow the laser to propagate without much scattering to the PSD [27]. Furthermore, the strong hydrodynamic damping of the cantilever oscillation in all kinds of liquids (often expressed in terms of a significantly reduced quality factor Q) severely hinders the use of dynamic atomic force microscopy (dAFM) modes. The force sensitivity is decreased and the thermal noise of the cantilever becomes more prominent. It was not until the signal to noise ratio (SNR) was greatly improved through the introduction of an optimized optical beam deflection system that true atomic resolution in liquids became possible [3, 35].

2.1 Probing the Solid-Liquid Interface

The solid-liquid interface plays a decisive role in a wide range of natural and technological processes [36, 37]. For instance, mineral dissolution, growth and weathering are pivotal within geochemistry and environmental science [6]. Nucleation and growth on a molecular scale at the solid-liquid interface govern biomineralization and biomimetic crystallisation processes, that are known to result in highly sophisticated, tailor-made materials [38–40]. In each of these fields, fundamental reactions take place at the solid-liquid interface. For understanding, modelling and predicting these interfacial processes, the accurate knowledge of the atomic structure of the surface and the local arrangement of the water molecules at the interface is an inevitable prerequisite. Only recent developments in AFM instrumentations have enabled high-resolution measurements at the solid-liquid interfaces and allow for the investigation of the local water structure.

In an AFM experiment the distance and geometry dependency of the different contributions often result in a complex force. The influence and occurrence of a particular force contribution depends on the actual tip, the surface and the environmental conditions of the AFM measurement. An approach to describe the tip-sample interactions in a liquid environment is the Derjaguin-Landau-Verwey-Overbeek (DLVO) theory, which only considers van-der-Waals (vdW) forces and electrostatic double layer (EDL) forces [11, 41].

The vdW forces originate from electric dipole interactions between individual atoms (or molecules) [42]. Consequently, the resulting net vdW force consists of these individual interactions between tip and surface atoms. For different materials under UHV conditions, the vdW force is always attractive, whereas in a liquid environment the vdW force may be attractive or repulsive, depending on the relative optical properties of the materials involved [43].

The EDL forces result from the charging of tip and surface in (polar) liquids. There exists a number of material-dependent explanations for the charging mechanisms, such as ionisation or dissociation of surface groups, the specific and unspecific adsorption or binding of ions and/or particles, isomorph substitutions in the surface lattice, reconstruction of the surface termination, etc. Independent from the charging mechanism, the charges are balanced by counter ions in close proximity to the surface, forming the electric double layer [43]. In an *in-situ* AFM experiment the EDL force emerges upon the overlapping of the electric double layers from tip and sample. Due to the polarity of tip and sample the resulting force may be repulsive or attractive. The EDL force decreases roughly exponentially at a large distance and can be estimated based on continuum theories, such as the Debye-Hückel [44] or

the Gouy-Chapman theory [45, 46]. The length scale of the electrostatic interaction varies between ~0.2 nm and hundreds of nanometres and can be reduced (increased) by increasing (reducing) the concentration of the electrolytes in the solution [47]. The EDL force is generally considered to impede the imaging with the AFM and effects the oscillation of the cantilever as a background force [34]. Thus, it is a common approach to increase the concentration of the electrolytes in liquid AFM experiments to improve the imaging conditions [48]. This can be easily done using high concentrations of (poly-valent) electrolytes that help to suppress the EDL force. This concept has been used successfully for imaging biological samples [49] and mineral surfaces [50].

The DLVO theory has been used with great success in the description of colloidal systems; however, the simple model does not consider all forces that occur in a liquid environment. For instance, the DLVO theory breaks down when the distance between tip and sample is reduced to only a few diameters of the solvent molecule [51]. The most important class of non-DLVO forces is called solvation forces, and in aqueous systems, hydration forces [27]. They are directly related to the structure of the solvent at the solid-liquid interface that often deviates from the bulk structure [52]. These forces can be monotonically or oscillatory and at small tip-sample distances, much larger than vdW or EDL forces [43]. The identification of different contributions to the solvation forces and their origin is largely based on experiments. The entire field of solvation forces was, and still is, an active field of research [51, 53, 54].

The best understood and most general type of solvation force is the so-called structural or oscillatory force that originates from the specific structure of the liquid as discrete, ordered solvent molecules. In the small region above the surface, the solvent molecules are often ordered into layer(s) which give(s) rise to an oscillatory behaviour in the average density of the solvent [55]. The approaching AFM tip squeezes out layer after layer of solvent molecules between tip and sample, resulting in an oscillatory contribution to the tip-sample force. The layering of solvent molecules has been first shown by surface force apparatus (SFA) experiments with octamethylcyclotetrasiloxan on mica [56] and later by numerous dAFM experiments [57–67]. The reported distance-dependence of the structural force scales with the molecular dimensions of the solvent molecules [43]. The solvation forces are often approximated as an exponential decaying oscillation function [11, 68].

The site-specific nature of the solvation forces can be probed in high-resolution AFM experiments and reflects the corrugation and/or the solvophobic/solvophilic properties of the surface [69, 70]. Still, the interpretation of AFM data measured at the solid-liquid remains difficult since the contrast strongly depends on the complex interaction between sample, cantilever tip termination and the surrounding solvent molecules. Several theoretical studies about probing hydration layers with the AFM at the solid-liquid interface agree on the fact that the forces acting on the cantilever tip originate from both direct interactions between tip and surface and water-mediated contributions [71–74]. Furthermore, one study indicates that the force measured with an AFM is, under specific but realistic experimental conditions, directly proportional to the solvent density at the solid-liquid interface [75]. The aforementioned theoretical study supports the qualitative correlation of AFM data with interfacial water densities.

2.2 Operation Modes

The AFM is a versatile instrument with a great variety of operation modes. A simple and straightforward distinction based on the technical implementation is made between static atomic force microscopy (sAFM) and dynamic atomic force microscopy (dAFM). In the case of static modes, the cantilever is simply scanned over the surface, whereas in dynamic modes, the cantilever is also externally excited during the scan motion. There are three dynamic modes, the amplitude modulated (AM) (also known as Tapping Mode™) [76], the frequency modulated (FM) [77] and the phase modulated (PM) mode [78]. The latter has not reached the importance and widespread use of the other two dAFM modes. Within the literature one can also find the terminology of non-contact and contact AFM. The first term is often implicitly employed for frequency modulation atomic force microscopy (FM-AFM) experiments under UHV conditions in the attractive regime, or if the operator of the AFM believes that there is no contact between tip and sample during the experiment [79]. However, if the tip makes physical contact with the surface strongly depends on the conditions of the experiment [80].

AFM operation modes can be used in combination with a distance feedback loop. The displacement of the piezo controlling the distance between tip and sample (often simply named “z-piezo” signal or topography channel) is recorded in AFM experiments [29]. The importance of the feedback loop for the interpretation of any experimentally acquired AFM data is illustrated in fig. 2.2. If the feedback loop is switched off, the voltage of the z-piezo is constant during the AFM experiment and the entire information of the tip-surface interaction appears in the channels capturing the de-

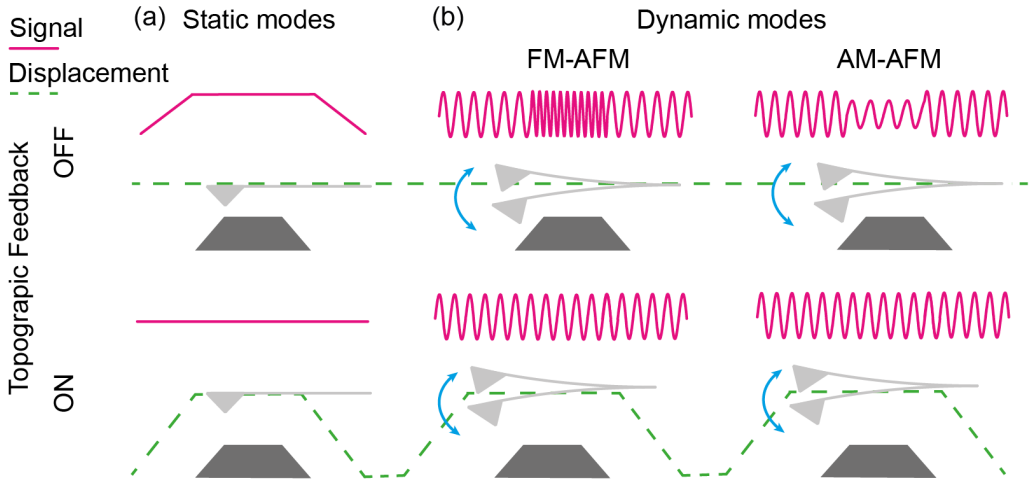

Figure 2.2.: A simplified (no artefacts considered) comparison of the most popular AFM modes, namely the static and the two dynamic modes (AM and FM), with and without active feedback loop.

flection (sAFM) or the parameters of the oscillation (dAFM), e.g, the amplitude and phase (AM-AFM) or the frequency shift and dissipation signal (FM-AFM). When the AFM is used with an active feedback loop, the tip-sample distance is adjusted to match a certain setpoint, e.g., a constant cantilever deflection (sAFM) or a fixed oscillation parameter (dAFM). For a perfectly working feedback loop every change in the tip-sample interaction is only displayed in the topography channel. However, these two extreme cases almost never match the experimental conditions. Without a feedback loop the tip is likely to crash into the surface and causes severe damage to the sample or itself. On the other hand, due to intrinsic technical limitations, a feedback loop can never work perfectly. Therefore, every AFM measurement may contain artefacts, particularly when sudden changes during the measurement occur (e.g. large protrusions). For the investigation of (atomically) flat surfaces the feedback loop is often set to very slow response times, thus, it still accounts for small changes of the surface position but allows for quasi constant-height data acquisition.

Static AFM

The easiest way to operate an AFM is to press the sensor, e.g., the cantilever, onto the surface and measure the bending of the cantilever (also called the static deflection) that can be directly converted into force by Hooke's law. Even this simple approach can provide great resolution, but is limited when it comes to achieving "true atomic resolution". True atomic resolution is characterised by the possibility to resolve defects such as single-point defects or step edges on the atomic scale

(fig. 2.3). Hence, the interaction between the foremost tip atom and a single surface atom is often proposed to be the main contributor for high resolution. In sAFM the scanning motion in the contact regime creates high sheer forces that reduces the image quality. Due to the direct contact of the cantilever tip with the surface, the tip apex easily degrades and will be covered with sample material.

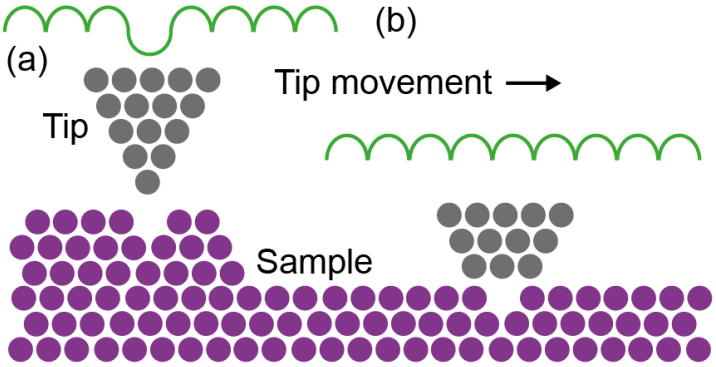

Figure 2.3.: An illustration of the tip scanning the surface (a) with and (b) without an atomic-size tip. A blunt tip in contact mode will only generate grid-like resolution. Only a sharp tip is capable of true atomic resolution.

Therefore, the resolution is limited to at best, a grid-like resolution. The lattice of the surface atoms is still visible, but atomic defects cannot be resolved since the radii of the tip apex directly determines the imaged area. However, there is one example for a static AFM experiment, performed by Ohnesorge *et al.* [81], claiming to achieve true atomic resolution. In this experiment they made use of the constant-height mode (distance feedback loop switched off) in the non-contact regime and used a rather stiff cantilever to prevent mechanical contact between tip and surface. However, this approach is experimentally very challenging and sAFM is rarely used for high-resolution AFM imaging.

Dynamic AFM Modes

A more sophisticated variant of AFM modes are the dynamic modes, where the cantilever is externally excited and the change in its oscillation behaviour due to the tip-sample interactions is monitored. As a control parameter for the AFM operation either amplitude, frequency or phase shift can be used. The relationship between the acting force and the measured oscillation parameter is not straightforward. Several theoretical formalisms compete for the proper description of the cantilever motion trying to link AFM observables to the acting tip-sample force [47]. This section introduces an essential approach based on the driven harmonic oscillator with damping to provide an understanding of the cantilever motion [82]. In a dAFM experiment the cantilever is driven by an external sinusoidal force $F_D(t)$ (eq. 2.1).

$$F_{\mathrm{D}}(t) = F_0 \cos(\omega_{\mathrm{D}} t + \varphi) = kA_0 \cos(\omega_{\mathrm{D}} t + \varphi) \tag{2.1}$$

Here, F_0 is the excitation force and A_0 is the excitation amplitude of the cantilever, respectively; φ is the phase shift between the excitation and the resulting oscillation of the cantilever, while ω_{D} is the angular frequency of the external excitation. The relevant equation of motion of the cantilever is a second order differential equation (eq. 2.2).

$$0 = m\ddot{q}(t) + \delta\dot{q}(t) + kq(t) - F_{\mathrm{D}}(t) \tag{2.2}$$

The cantilever is considered an ideal spring with a spring constant k, driven with the external force $F_{\mathrm{D}}(t)$, damped by a constant δ. Here, the instantaneous cantilever displacement $q(t)$ is considered with respect to its zero position. The mass m is often referred to as "effective mass" and should not be confused with the actual mass of the cantilever [83]. The proper approximation of the effective mass of the oscillating cantilever depends on its geometry and also on the environment [84, 85]. For the sake of simplicity, higher harmonics of the cantilever oscillation are omitted. They are difficult to detect and are often hidden in the experimental noise floor, although they offer an interesting route to explore surface properties [86]. The equation of motion (eq. 2.2) can be easily solved by the ansatz given in (eq. 2.3).

$$q(t) = A\cos(\omega_{\mathrm{D}} t) \tag{2.3}$$

This approach yields a general solution consisting of a transient solution and a stationary solution. The transient solution is mainly of importance during the settling or the re-swing after a significant disturbance, e.g., by a sudden change in tip-sample interactions. However, the stationary solution (given eq. 2.4) is of major interest, since standard AFM experiments are typically done with an active feedback control that prevents the cantilever from such significant disturbance.

$$\tan(\varphi) = \frac{\frac{\delta}{m}\omega_D}{\left(\frac{k}{m}\right) - \omega_D^2} \qquad A = \frac{\frac{F_0}{m}}{\sqrt{\left(\omega_D^2 - \left(\frac{k}{m}\right)\right)^2 + \left(\frac{\delta\omega_D}{m}\right)^2}} \tag{2.4}$$

The use of the quality factor Q and the eigenfrequency ω_E instead of the effective mass, the spring constant and the damping constant, as given in eq. 2.5, is a very common way to express the stationary solution within the literature.

$$\tan(\varphi) = \frac{\omega_D}{Q\omega_E\left(1 - \frac{\omega_D^2}{\omega_E^2}\right)} \qquad A = \frac{A_0}{\sqrt{\left(1 - \frac{\omega_D^2}{\omega_E^2}\right)^2 + \frac{\omega_D^2}{Q^2\omega_E^2}}} \tag{2.5}$$

The angular eigenfrequency ω_E, is the angular frequency of the (undamped and not externally excited) harmonic oscillator and not to be confused with the angular resonance frequency ω_R, which is the angular frequency at the maximal amplitude response (eq. 2.6).

$$\omega_E = \sqrt{\frac{k}{m}} = \text{const.} \qquad \omega_R = \omega_E\sqrt{1 - \frac{1}{2Q^2}} \tag{2.6}$$

The quality factor Q is defined as the ratio between the energy stored in the oscillation and the energy dissipated in each oscillation cycle at the angular eigenfrequency ω_E. There is a simple relationship (eq. 2.7) to the damping coefficient δ [87].

$$Q = 2\pi\frac{E_{\text{stored}}}{E_{\text{loss}}} = \frac{\omega_E m}{\delta} \tag{2.7}$$

In a dAFM experiment the cantilever may undergo dissipative and conservative interactions due to a complex tip-sample force. All interactions acting between cantilever tip and sample are modelled within this approach by introducing a single term for the tip-sample force F_{TS} in the equation of motion. However, it is a common approach to approximate the tip-sample force with effective parameters for the spring constant and the damping constant. Thus, the solution of the perturbed system has the same form as the solution of an unperturbed harmonic system. In the dAFM modes, the

oscillation characteristics of the cantilever are measured as time-averaged, distance-dependent quantities and the signal is averaged over a whole oscillation cycle [88]. Therefore, it is justified that the effective parameters for the spring constant k and for the damping constant also represent averaged quantities and not momentary values [82]. This parameter substitution is only valid for weak tip-sample forces. In this approach the cantilever motion is an (sinusoidal) approximation of the real cantilever motion [82].

Amplitude Modulation Mode

In the case of amplitude modulation atomic force microscopy (AM-AFM), the amplitude and the phase of the cantilever motion are directly measured. The experimental set-up of AM-AFM is summarised in fig. 2.4. A signal generator is used to sinusoidally excite the cantilever with a fixed drive amplitude A_0 and drive frequency ω_D. During the scanning process the dynamic deflection signal of the cantilever is captured by a PSD. The amplitude and phase of the deflection signal are detected by a lock-in amplifier. In constant amplitude-mode the amplitude signal is used as a control parameter for the distance feedback loop which ensures the stable operation of the AFM experiment, e.g., preventing the cantilever from crashing into the surface. In the AM-AFM mode, only one feedback loop is required. The excitation frequency ω_D is often chosen close to, or at, the angular eigenfrequency ω_0 to ensure a large amplitude signal.

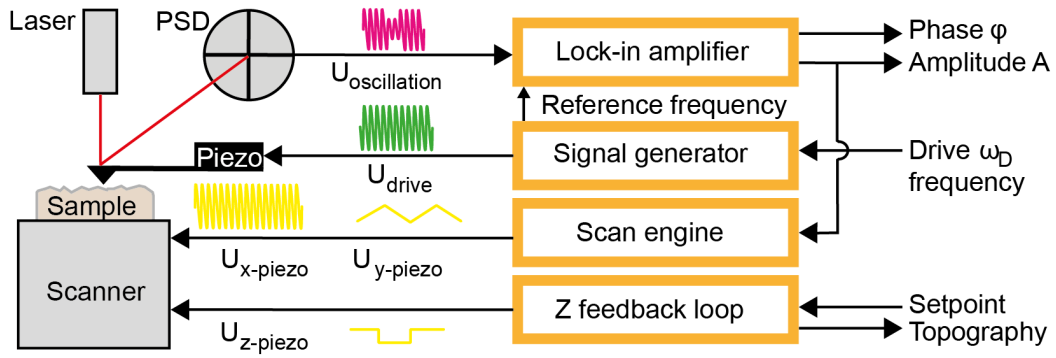

Figure 2.4.: Block diagram of an AM-AFM setup. The cantilever is excited at a fixed frequency. The cantilever deflection is detected by a PSD. Amplitude and phase of this signal are commonly detected with a lock-in amplifier. A feedback loop maintains a constant amplitude based on the user set-point.

A large and growing body of literature is dedicated to the phase signal of AM-AFM, because it often provides images with an impressive contrast. "Phase imaging" is currently widely used to investigate the surface composition of heterogeneous materials and is generally accepted to be sensitive to material properties [89–91].

A breakthrough in understanding the physical basis for the contrast formation of AM-AFM was made when an analytic expression between energy dissipation (or power loss per cantilever oscillation cycle) and phase shift at the eigenfrequency was derived [92–95]. However, the phase signal contains no information about the mechanisms involved in the energy transfer or the time scale of the processes involved in the dissipation [96]. Furthermore, when inspecting eq. 2.4 it becomes clear that both, dissipative and conservative forces contribute to the contrast formation in both amplitude and phase signal [97–99]. Therefore, different contrasts in the phase signal are always due to the presence of both conservative and dissipative (material-dependent) interactions [82]. The quantitative capabilities of AM-AFM are limited, and the development of a technique to calculate the interaction force (based on amplitude and phase) is still an ongoing process [100]. Thus, to present the full information of an AM-AFM experiment, both signals, amplitude and phase, are shown.

Frequency Modulation Mode

In the case of FM-AFM the frequency shift $\Delta\omega$ (as given in eq. 2.8), often simply called detuning, and the dissipation signal Γ are captured instead. The frequency shift $\Delta\omega$ is a function of the tip-sample distance z and relates the actual eigenfrequency ω'_{E} (the eigenfrequency at a given tip-sample interaction) to the angular eigenfrequency of the cantilever far away from the surface ω^0_{E} (without any tip-sample interactions).

$$\Delta\omega = \omega'_{\mathrm{E}} - \omega^0_{\mathrm{E}} \tag{2.8}$$

The FM-AFM mode is a challenging technique because it requires three feedback loops to control the phase, the amplitude and the tip-sample distance. The technical implementation of FM-AFM is shown in fig. 2.5. Like in AM-AFM, the cantilever is sinusoidally excited by a signal generator and the dynamic deflection signal of the cantilever is captured by a PSD during the scanning process. The signal of the PSD is demodulated by a phase-locked loop (PLL) to determine the frequency shift between the undisturbed cantilever and the cantilever scanned above the surface. The PLL also provides a reference signal for the signal generator to always excite the cantilever at the actual eigenfrequency by keeping the phase shift between the cantilever excitation and response at 90°. Furthermore, the dynamic deflection signal is fed into a lock-in amplifier that is part of the amplitude-control circuit, which

ensures that the oscillation amplitude is always constant within the experiment. In the constant frequency shift mode, the difference in the eigenfrequency between far away from the surface and close to the surface is used as a control parameter for the z-piezo feedback loop.

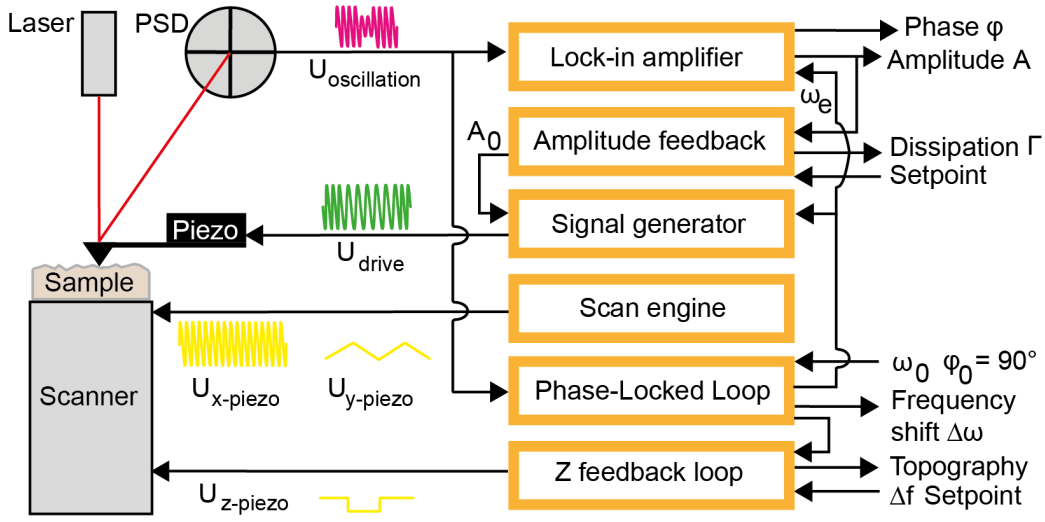

Figure 2.5.: Block diagram of an FM-AFM setup. The cantilever is excited at a fixed frequency. The cantilever movement is detected by a PSD. Amplitude and phase of this signal are commonly detected with a lock-in amplifier and the actual eigenfrequency is detected by a PLL. Three feedback loops controlling amplitude, phase and z-piezo voltage.

The separation of conservative and dissipative forces is of major interest for all kinds of dAFM experiments because different interaction processes and surface properties are linked to these different contributions. The experimental set-up of FM-AFM allows for a separation of conservative and dissipative forces acting on the cantilever tip because their mixing is avoided [101].

$$\varphi(\omega_D) = \frac{\pi}{2} \qquad |A(\omega_D)| = QA_0 \tag{2.9}$$

This becomes evident from eq. 2.5, which further simplifies to eq. 2.9 in the case of FM-AFM, because the driving frequency ω_D is equal to the eigenfrequency ω_E. It is crucial that the AFM instrument is capable of keeping the phase offset at 90° so the decoupling of the conservative and dissipative forces a given at any time [63].

$$\Delta\omega(z) = \frac{\omega_E^0}{\pi k A^2} \int_{-A}^{A} F_{ts}(z+A-q) \frac{q}{\sqrt{A^2-q^2}} dq \tag{2.10}$$

The frequency shift is directly related to the tip-sample forces (see eq. 2.10) as a function of the tip-sample distance z. If the amplitude is much smaller then the force interaction range, the force gradient is constant and simply proportional to the frequency shift [42]. A model of the change in the cantilever response of the amplitude and phase due to different tip-sample forces is shown in fig. 2.6. However, this simplified model is only valid for one particular amplitude (depending on the interaction potential) [102]. Two techniques to calculate the force (based on eq. 2.10) are well established for FM-AFM: the Sader-Jarvis method [103] and the Matrix method by Giessibl [104]. The energy, which has to be applied to the cantilever for the excitation of a constant amplitude, is proportional to the dissipated energy during the oscillation of the cantilever and can be calculated from the dissipation signal Γ [105].

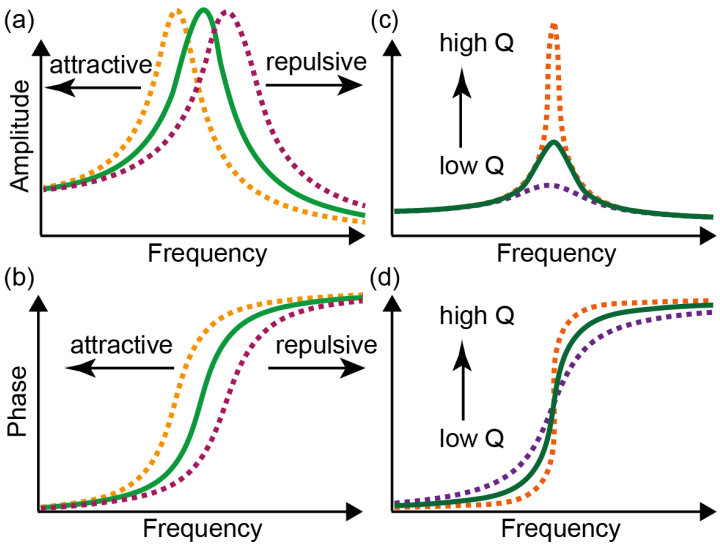

Figure 2.6.: The cantilever response when disturbed by purely conservative forces (attractive or repulsive) for (a) the amplitude and (b) the phase as well as the response on solely damping (dissipative forces) for (c) amplitude and (d) the phase.

In all dAFM modes, the very same physical concepts contribute to the contrast formation on an atomic scale. They share the shift of the eigenfrequency and the damping caused by tip-sample forces, the competition between attractive and repulsive forces and the presence of several oscillation states [106]. The relationship between the recorded cantilever oscillation quantities and the effective parameters depends on the period of the oscillation. From an experimental point of view, this dependence in time transfers to a dependence in space. Therefore, the recording of the oscillation parameters in dependency of the tip-sample distance is a prerequisite for the recovering of the acting tip-sample forces. An extensive introduction in the AFM technique is given in the textbooks of Morita *et al.* [107] or García [47] and in the excellent reviews from Giessibl [29], García *et al.* [106], and Hofer *et al.* [108].

The so-called "forest of peaks"

For the dynamic AFM modes in liquid, the standard excitation method is the piezo acoustic excitation [109, 110]. The cantilever is vibrated by a shake piezo that is mounted close to the cantilever holder. However, the piezo actuator often does not only shake the cantilever itself but also the cantilever holder and the surrounding liquid. This method is responsible for the so-called "forest of peaks" that is caused by the motion of the fluid close to the cantilever. The "forest of peaks" depends only on the cantilever module, the shake piezo actuator and the fluid, but not on the geometry of the cantilever. The term "forest of peaks" refers to various additional peaks in the resonance (red) curve shown in fig. 2.7 (a) [111]. To eliminate the "forest of peaks", further excitation systems based on magnetic [112], electrostatic [113] or photothermal [114, 115] methods have been developed. For the photothermal excitation an additional (often times a blue) laser is used to induce the cantilever oscillation by the absorption of the laser light on the back of the sensor. This concept is one of the most sophisticated solutions available so far, and it provides a very reliable option for stable measurements in a liquid environment. The photothermal excitation yields a cantilever response that is very close to the theoretical response of an excited, damped harmonic oscillator. Within this thesis both the piezo acoustic and the photothermal excitation methods are used.

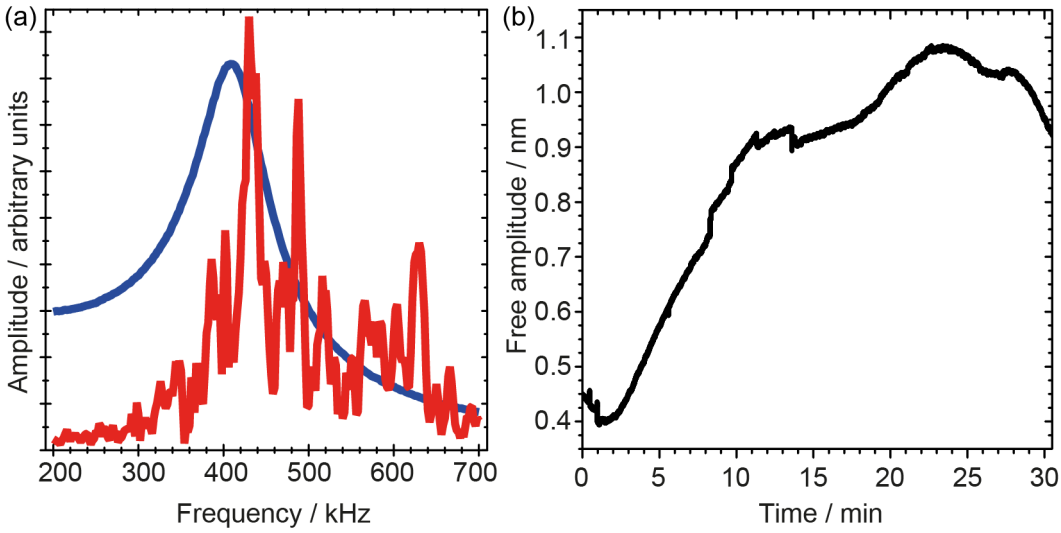

Figure 2.7.: (a) Typical frequency sweep curves of a cantilever in water with piezo acoustic (red line) and photothermal excitation (blue line). (b) The temporal change of the free amplitude at a constant excitation amplitude when the cantilever is positioned far away from the surface and immersed in oversaturated calcium carbonate solution at 301 K.

The distortion caused by the "forest of peaks" compared to the expected and desired cantilever response is illustrated by a direct comparison of piezo acoustic (red) and photothermal excitation (blue) in (fig. 2.7 (a)). The additional resonances within the "forest of peaks" constantly change their frequency upon tiny changes in, e.g., the amount of liquid in the cell which causes the cantilever resonance to drift and distort throughout the experiment [116]. When using piezo excitation, the free amplitude is subject to changes caused by this drifting "forest of peaks" which causes significant difficulties in maintaining a constant amplitude over time [110, 117]. When inspecting the change in the free amplitude over time (fig. 2.7 (b)), it becomes evident that this effect has to be taken into account when aiming at stable experimental conditions on the time scale of the AFM experiment.

2.3 The AFM Mapping Technique

Despite the impressive results of high-resolution dAFM imaging in both UHV and liquid, horizontal two-dimensional (2D) images only reflect planes of the observed quantities in dependence of the feedback settings. However, for a deeper insight into contrast formation and the involved (atomistic) processes, it is essential to collect the distance-dependent tip-sample interaction. To overcome the limitation of standard AFM operation, a mapping technique has been developed to record data also in the vertical direction.

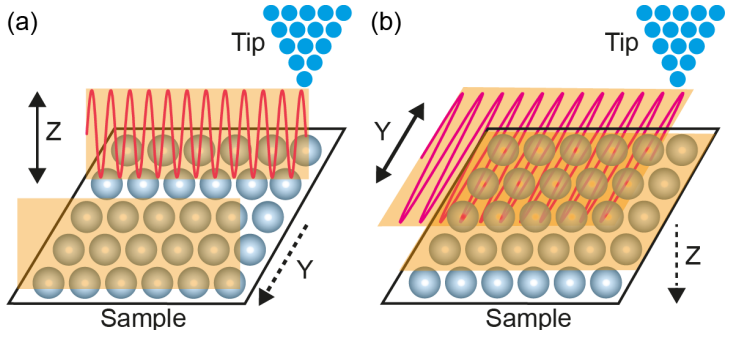

Figure 2.8.: The two typical implementations of three-dimensional (3D) mapping in the AFM. In (a) the "curve-by-curve" approach and in (b) the "layer-by-layer" approach is shown.

For 3D mapping, the cantilever is scanned both vertically and laterally above the surface and two different data acquisition protocols can be distinguished, i.e., the "curve-by-curve" approach [118, 119] (fig. 2.8 (a)), performing a set of force curves; and the "layer-by-layer" approach [120] (fig. 2.8 (b)), imaging the surface at different tip-sample distances. The "curve-by-curve" approach was first realised as a consecutive development of the early sAFM experiments with a one-dimensional (1D) data sampling. After a single force distance curve, the tip is positioned at the new start position for the next curve which introduces a little pause between them.

A faster approach presented by Fukuma *et al.* [70] omits this repositioning in the mapping routine by a sinusoidal modulation of the tip-sample distance that allows for much shorter data acquisition times. This is an important step to perform 3D mapping in a liquid environment with large thermal drift at ambient conditions. The development of 2D- and 3D mapping techniques has attracted a lot of attention within the AFM community because it offers a route to recover the distance-dependent and site-specific surface forces.

The first 3D dAFM map was reported on the pristine NiO(001) surface under UHV conditions [121] and was followed by numerous 2D [122–126] and 3D [127, 128] mapping experiments. On the calcite(10.4) surface, the first 3D map under UHV conditions was presented in 2011 by Rahe *et al.* [129]. The use of high-resolution mapping techniques in liquid provides an unique route for investigating the solid-liquid interface, especially the solvation force. 2D and 3D mapping experiments in water have been performed on pristine surfaces such as mica [48, 70], α-Al_2O_3 [130] and graphite [131]. These studies have later been extended to molecular crystals [132], layers of organic molecules [133], surfactant liquid [134], biological systems, such as lipid layers [135, 136], and long-chain alkanes as solvent [137, 138].

3 Implementation of 3D AM-AFM Mapping Routine - A Case Study on Calcite

Calcite, the most stable modification of calcium carbonate $CaCO_3$, is an abundant mineral in nature. It has been studied extensively due to its importance in various fields, such as biomineralization [39], the biogeochemical cycle of carbon [139], and oil recovery [140]. Knowledge of calcite's surface structure and reactivity of the most stable cleavage plane, the (10.4) plane, is pivotal for understanding its role in these diverse areas. The unit cell on the calcite(10.4) surface is rectangular with dimensions of 0.80×0.50 nm as shown in fig. 3.1. It contains two carbonate groups that are rotated with respect to each other, forming a "zigzag" pattern along the $[010]$ direction. With respect to the surface, one oxygen atom of each carbonate group is in the plane, one oxygen atom protrudes the surface, and one is pointing into the bulk. The detailed surface structure has been elucidated using atomic force microscopy (AFM) operated in air [141], in vacuum [142] and under aqueous conditions [81, 141, 143–145]. Rode *et al.* [16] have studied the (10.4) plane by using frequency modulation atomic force microscopy (FM-AFM) on a modified commercial instrument with a very small signal to noise ratio (SNR) and achieved true atomic resolution in a liquid environment for the first time.

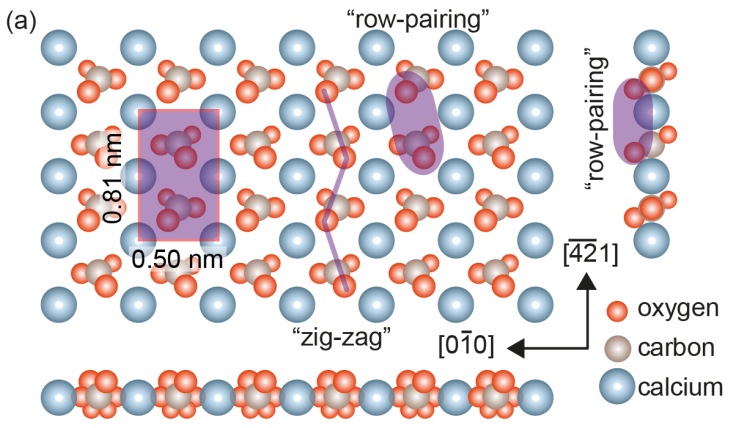

Figure 3.1.: Bulk truncated structure of the calcite(10.4) surface [146]. The surface unit cell and projections along the $[010]$ and the $[4\bar{2}1]$ are given. The most prominent features such as the "zigzag" and the "row-pairing" reconstruction are indicated.

Since most biological processes and technical applications take place in an aqueous environment, perhaps the most basic question addresses the interaction of water molecules with the calcite(10.4) surface. The interaction of water with the calcite surface has been studied experimentally by X-ray scattering [147–149] and, only

very recently, using FM-AFM [150–152]. Based on FM-AFM data, two groups have identified distinct water patterns above the calcite. Imada *et al.* have reported a "checker-board" pattern along the [010] direction [150]. Kobayashi *et al.* have seen "diamond-like" and "line-shaped" patterns along [010] [151], which are tentatively ascribed to the two different orientations of the carbonate groups on the surface. Among the theoretical studies addressing the water-calcite interaction [73, 153–156], the work of Reischl *et al.* [73] is especially interesting because it takes the cantilever tip into account.

The aforementioned experimental and theoretical studies suggest that water forms well-ordered structures above the calcite(10.4) surface and at least three hydration layers have been identified. It is believed that the first water layer is adsorbed with its oxygen atoms on top of the surface calcium ions, while the second water layer is ascribed to water molecules forming hydrogen bonds with the protruding oxygen atoms of the carbonate groups. The third hydration layer is considered to be only weakly bound and with less lateral order compared to the first and second hydration layer.

To study the formation of solvent molecules above the calcite(10.4) surface, a three-dimensional (3D) data acquisition protocol was developed to overcome the limitation of standard (two-dimensional (2D)) AFM imaging. For the ease of implementation, amplitude modulation atomic force microscopy (AM-AFM) is the operation mode of choice. In comparison with FM-AFM, AM-AFM only requires one feedback loop (sec. 2.2) while the amplitude and the phase are directly used as the imaging signals. The following section reports on the implementation of the newly developed 3D scanning routine. The performance of the set-up is demonstrated by mapping the hydration layers above the calcite(10.4) surface. The results presented in this chapter has been also published as an article in (the journal) nanotechnology from IOPs science [4].

3.1 The 3D Data Acquisition Protocol

The 3D routine is implemented in a commercially available Cypher AFM with an ARC 2 controller from Asylum Research, an Oxford Instruments Company (United Kingdom) (fig. 3.2). The instrument is operated using the data evaluation software Igor Pro (WaveMetrics, USA), that allows users to write their own control routines. The implementation of the 3D mapping routine in the Cypher AFM was done using this interface and existing routines from Asylum Research.

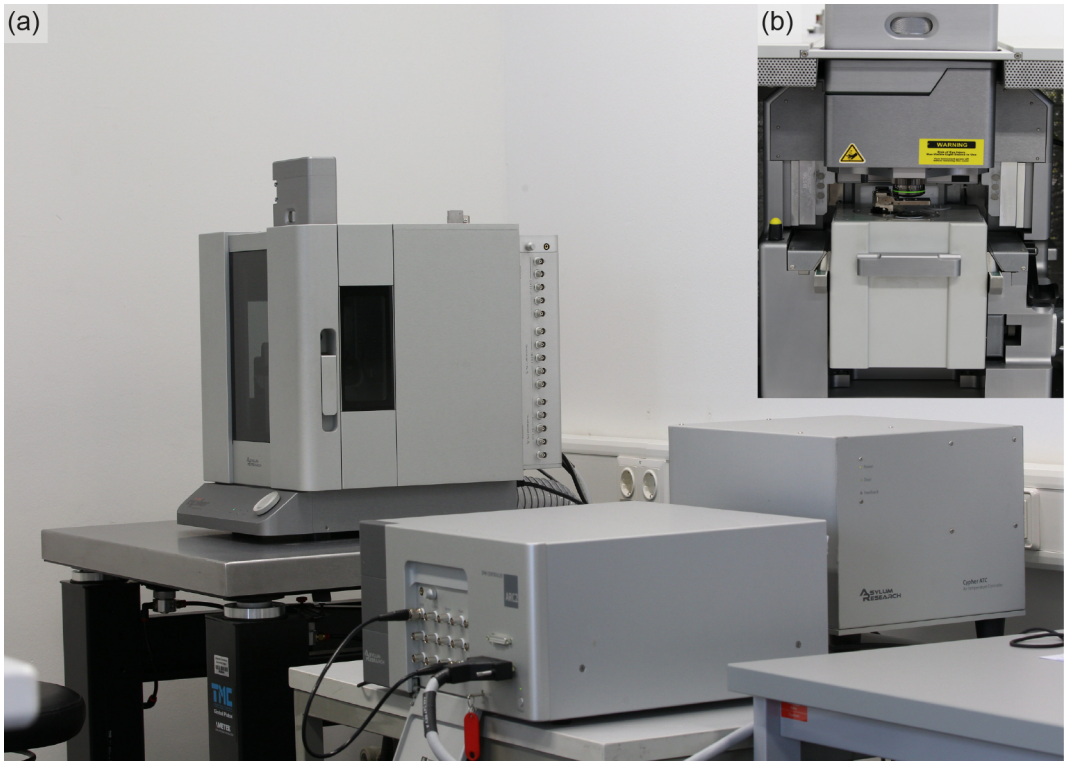

Figure 3.2.: Photograph (from left to right) of (a) the Cypher AFM, the Asylum Research Controller (ARC) (version 2) and the Air Temperature Control (ATC) box. Inlet (b) shows the scanner and the "liquid cell" of the Cypher AFM. The pictures are kindly provided by Holger Adam.

The 3D protocol is integrated into the standard scanning routine by applying an additional, sinusoidal modulation to the z-piezo voltage, causing a modulation of the tip-sample distance ("curve-by-curve" approach) [157]. Due to the sinusoidal movement of the z-piezo, more data points are acquired around the turning points. No threshold or abort condition for the oscillation amplitude or the phase is implemented in the routine. Hence, the volume of the 3D map is precisely determined by two parameters: the average tip-sample distance and the modulation range as shown in fig. 3.3. The average tip-sample distance is determined by the oscillation amplitude set-point expressed as a fraction of the free oscillation amplitude that remains unchanged during the modulation of the z-piezo voltage. A small amplitude

set-point corresponds to a small tip-sample distance, whereas a large set-point means a large tip-sample separation. The distance-feedback loop operates very slowly during the data acquisition. It is too slow to compensate for the applied z-modulation, but fast enough to compensate for z-drift effects and tilt caused by misalignment of the sample. Before the data acquisition starts, the routine adjusts the phase shift between excitation and cantilever response to 90°, which allows for easy comparison of data acquired in different experiments. To control the tip condition it is helpful to perform normal AFM images in between the 3D maps. The 3D acquisition protocol is capable of capturing the four relevant signals, i.e., amplitude, phase, static cantilever deflection, and the output of the z-piezo feedback loop (topography channel). The static deflection signal is obtained by applying a 25 kHz low-passfilter to the photodiode signal (dynamic deflection signal).

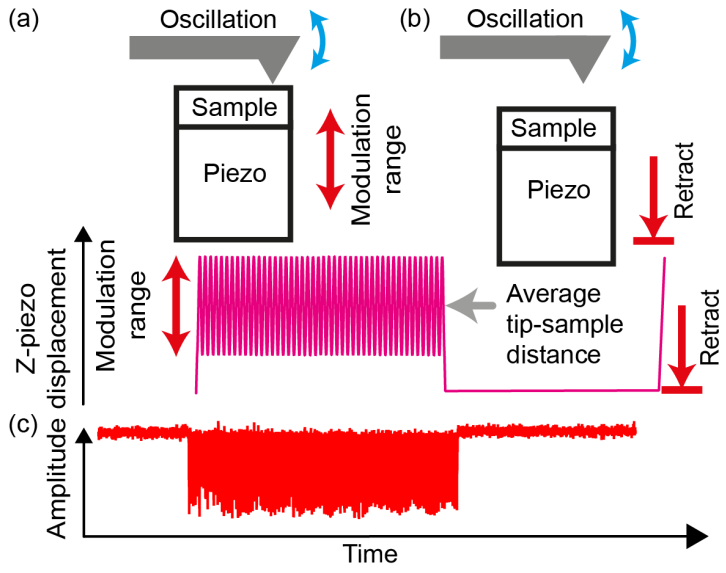

Figure 3.3.: The 3D data acquisition protocol collects valid 3D mapping data only during the retrace movement (a). Here, the average tip-sample distance is determined by the oscillation amplitude set-point. In the trace movement (b), the sample is retracted and a feedback loop adjusts the excitation to keep the free amplitude of the cantilever constant.

As I started the development of the 3D routine, the used Cypher AFM was equipped with piezo-acoustic excitation only. Furthermore, the standard scanner used for the experiments was and still is not shielded against evaporation (in the following referred to as open liquid cell). Consequently, a major difficulty in this AFM set-up was the drifting "forest of peaks" and without compensation, the free amplitude is subject to significant changes on the time scale required for one 3D map (sec. 2.2). To compensate for this effect, the excitation needs to be adjusted regularly to keep the free amplitude constant. Therefore, a feedback loop that adjusts the excitation amplitude during the 3D data acquisition is implemented in the 3D routine. The amplitude and phase data are only collected during one half of each scan line (usually the retrace movement). Here, the sample is in close vicinity to the tip and the z-piezo modulation voltage is applied (fig. 3.3 (a)). In the second half of each scan line (usually

the trace movement), the sample is pulled away from the tip, no z-modulation takes place and no 3D mapping is done (fig. 3.3 (b)). Instead, the excitation feedback adjusts the excitation amplitude to maintain a constant free amplitude throughout the entire measurement. During the adjustment procedure the distance feedback loop is switched off. The technical implementation of the excitation feedback consists of a lock-in amplifier for measuring the free amplitude of the cantilever and a built-in feedback loop of the Cypher AFM that is used for regulating the excitation amplitude. The extent of the necessary adjustment of the excitation amplitude depends crucially on the shape of the "forest of peaks" and on the drift conditions of the specific measurement, both being unpredictable. In fig. 3.3 (c) a typical example of the recorded oscillation amplitude during an entire scan line is shown, illustrating the working principle of the free amplitude adjustment.

To suppress thermal drift effects, the 3D mapping experiment needs to be performed with very high scan rates compared to those typically applied in ultra high vacuum (UHV). The modulation frequency of the z-voltage has to be considerably higher than the scan rate and significantly lower than the oscillation frequency of the cantilever. In the experiments, scan rates between 2 Hz and 4 Hz, and modulation frequencies between 500 Hz and 750 Hz proved to be very efficient. In the set-up , the full potential of the AFM electronics is exploited by using the maximum sample rate of 50 kHz to process the signal from the photodiode. Therefore, a 3D map of $96 \times 240 \times 68$ pixel (x $\times$ y $\times$ z pixel), which includes overscanning (25%), approach, retract and free amplitude adjustment, requires approximately 30 s. To simplify the use of the 3D routine, the experimentalist only needs to enter the scan rate and the number of points in the x-direction (fast scan direction) for the 3D routine to calculate the appropriate number of points in the z-direction according to eq. 3.1. A more detailed description of the 3D code is given in appendix A.

$$\text{Points in Z} = \frac{50\text{kHz}}{\text{Points in X} \times 2.5 \times \text{Scan Rate}} \tag{3.1}$$

The obtained 3D data volumes were analysed with a self-written framework within the Igor Pro software. The focus during the development was set on user-friendly usability. Therefore, the framework provides basic features such as import and export functions for the 3D data sets, display functions, and data validation; but also advanced features, such as the possibility to display arbitrary slices of any of the captured channels using the Bresenham Line Algorithm [158]. The framework also allows for analysis of any channel at any surface site of interest.

Experimental Preparation

Instrumental Set-up

For the measurements, Arrow UHF cantilevers (Nanoworld, Switzerland) are used with a resonance frequency in liquids of around 350 kHz. The cantilever oscillation properties were characterised by the thermal noise method [159]. Here, the constant excitation of the cantilever by the Brownian motion of the surrounding medium is captured as a function of the frequency (thermal noise spectra) and fitted to the equation of motion for a weakly disturbed harmonic oscillator.

The Cypher AFM can monitor the displacement of all piezos with in-buildlinear variable displacement transformer (LVDT) sensors. These low-noise sensors provides more accurately information about the true extend and retract distance of the piezos relative to the piezo voltage signal due to the hysteresis and creep of all piezos. With the help of these sensors the (XY-) scan piezos were calibrated once, on an appropriate scale for the 3D mapping experiments. The conversion factor between the actual cantilever deflection and the change in the photo-detector voltage, the inverse optical lever sensitivity (InvOLS), is measured by a force-distance curve (FDC) in the static atomic force microscopy (sAFM) mode. Here, the tip is in direct contact with the sample and the static deflection is linearly related to the piezo displacement. However, this procedure may cause severe tip degradation, therefore, this procedure is always performed after the 3D mapping experiments.

For the spring constant k values in the order of 4 $\frac{\mathrm{N}}{\mathrm{m}}$ are obtained and for the quality factor Q of the first resonance values between 4 and 7. Both parameters were measured from time to time for individual cantilevers. For cantilevers originating from the same batch, no large deviations were observed. An average sensitivity of 22 $\frac{\mathrm{nm}}{\mathrm{V}}$ was used to calculate the oscillation amplitude in the data presented in the following section. Using an average value for the InvOLS increases the error in the specification of the oscillation amplitude, however, for a qualitative evaluation of the data, this is of minor importance. For the free amplitude, we usually used values between 0.3 nm and 1.0 nm. Typical amplitude set-points were between 0.7 and 0.9, i.e., 70 %-90 % of the free amplitude. Z-modulation range values between ±0.5 nm and ±1.0 nm were chosen. The air fan of the ATC was set to 60 % and below to avoid the introduction of noise into the AFM imaging.

Sample Preparation

Calcite $CaCO_3$ crystals (Iceland Spar) were purchased from Wards Science (USA) with large surface areas of about $1 \times 1\,cm^2$ up to $1.5 \times 1.5\,cm^2$. The absolute orientation of the crystal directions were obtained before every experiment by optical means [160, 161]. To avoid dissolution of the calcite sample during data acquisition, the measurements were taken in a highly oversaturated solution of calcium carbonate $CaCO_3$ ($2\,\frac{mmol}{l}$). This solution was prepared by mixing corresponding quantities of sodium bicarbonate $NaHCO_3$ ($\geq 99.5\,\%$ from Carl-Roth) and calcium chloride $CaCl_2$ (*pure analysis* from Sigma-Aldrich) with Milli-Q water from a system by Millipore GmbH (Germany). The solution was degassed for half an hour using a water-jet vacuum pump. Calcite crystals were freshly cleaved before every measurement and immediately immersed into the oversaturated $CaCO_3$ solution. The actual temperature of the scan head during the 3D collection was recorded for each experiment.

3.2 Results and Discussion

High Resolution AFM Imaging

The (10.4) surface of calcite was imaging with the Cypher AFM using high-resolution AM-AFM. A series of merged AFM images, shown in fig. 3.4, demonstrate the capability of the instrument to image with atomic resolution. The AFM images are drift-corrected by the approach described by Rahe *et al.* [162]. Here, the drift velocity is determined by tracking a feature (an atom) through a consecutive series of AFM images. The correction is performed by a linear image distortion. If a reliable feature can be tracked over a series of images, it is very advantageous to use this approach because it does not rely on an initial assumption on the surface structure. The images in fig. 3.4 are corrected for sample tilt by applying a plane subtraction. The effect of sudden tip chances is minimised by a line-wise levelling based on the mean value of a line in the fast scan direction with the scanning probe microscopy (SPM) analysis software Gwyddion [163]. The unit cell dimensions obtained from the corrected images are $(0.78 \pm 0.05) \times (0.52 \pm 0.05)\,nm$ which agree within the errors to the lattice dimensions predicted from the bulk structure.

In the AFM images shown in fig. 3.4, the known surface characteristic "zigzag" and "row-pairing" along the [010] are very prominent. The "zigzag" (fig. 3.1) is ascribed to the protruding oxygen atom of the carbonate groups [141, 145]. The "row-pairing" describes the appearance of paired protrusions often combined with

a different brightness of the two protrusions. This distortion of the surface has been tentatively explained by a rotation of every second carbonate group [164]. The observed contrast on the calcite(10.4) and the magnitude of the surface characteristics strongly depend upon the imaging conditions, and differ from experiment to experiment. These findings nicely reproduce the FM-AFM result reported in the literature [16], and provide the basis to investigate the solid-liquid interface of (10.4) calcite with the developed 3D routine.

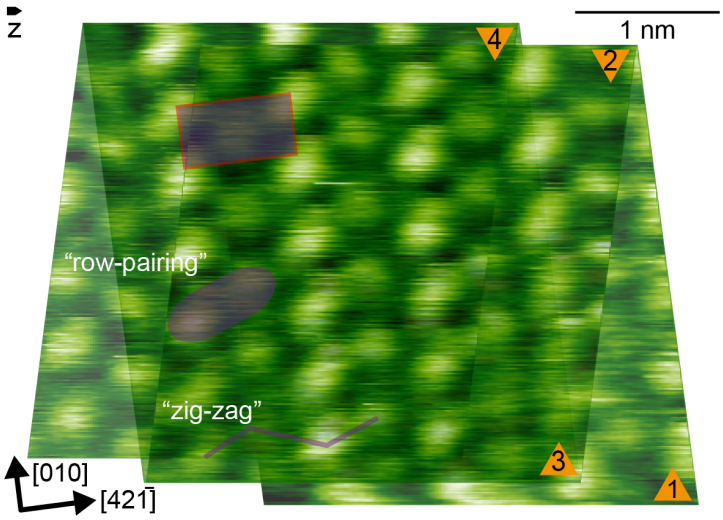

Figure 3.4.: A series of merged high-resolution AFM trace images corrected for lateral drift showing the calcite(10.4) surface. The AFM images are obtained with the Cypher AFM in Milli-Q water. The surface unit cell, the typical "zigzag" feature and the "row-pairing" reconstruction are marked.

3D Mapping Experiments

The performance of the 3D data acquisition routine is demonstrated by AM-AFM mapping of the hydration layers above the calcite(10.4) surface. The data are presented as 2D data slices along high-symmetry surface directions that are extracted from these 3D data sets. A grey colour scale is used, where dark areas represent low values, and bright areas high values, of the shown quantity, respectively. In fig. 3.5 (a,b), a representative slice along the [010] direction is shown. Although great care was taken to align the crystal such that the fast scan direction coincides with the [010] direction, slight misalignments always remain. Furthermore, drift effects may distort the AFM imaging in an unpredictable fashion. Here, 3D data collection has a clear advantage compared to 2D data acquisition because it allows for extracting 2D slice in any desired direction from the data volume in a post-imaging process. The slice in fig. 3.5 (a,b) shows data obtained during approach, i.e., when the sample moves towards the cantilever. The retract data of amplitude and phase signal (not shown) does not differ notably from the approach data. The

z-axis in the 3D maps corresponds to the change in tip-sample distance, which is induced by the sinusoidal movement of the z-piezo.

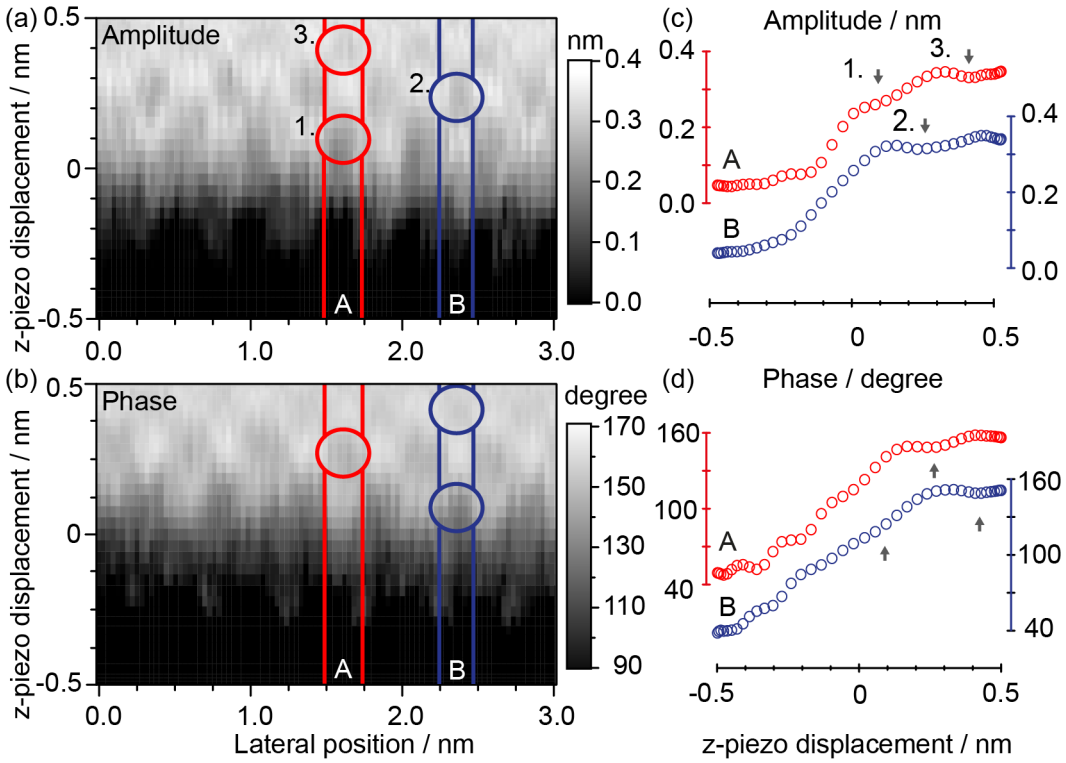

Figure 3.5.: Oscillation amplitude (a) and phase (b) 2D AM-AFM slices of the calcite(10.4) surface along the [010] direction. Two regions of interest are marked with red (A) and blue (B) boxes. Here, oscillation amplitude (c) and phase (d) one-dimensional (1D) data were extracted via averaging over the indicated areas. Modulations within the signals are marked with circles (a, b) and arrows (c, d). The corresponding 3D map was acquired at a temperature of 299 K, with a free amplitude of 0.4 nm, a set-point of 0.7 and a modulation range of ±0.5 nm.

As can be seen in fig. 3.5, high-resolution both laterally and perpendicularly to the surface was achieved and the 2D slices display a detailed image of the solid-liquid interface. When inspecting the amplitude signal (fig. 3.5 (a)), three distinct minima can be identified above the surface in two site-specific areas (A and B). These minima are periodically repeated parallel to the surface, which results in a characteristic "checker-board" pattern. A similar pattern is visible in the phase signal (fig. 3.5 (b)), however, here maxima are observed where the amplitude signal shows minima and *vice versa*. The modulations within amplitude and phase signal are ascribed to the three hydration layers above the calcite surface, in line with previous experimental findings [150, 151].

Contrast formation in AFM is generally very complicated since it strongly depends on the complex interaction between sample, cantilever tip and the surrounding environment, such as UHV [102, 142, 165] or water [71]. As usual for AFM experiments

in liquids, the tip termination is crucial for the contrast formation but impossible to be controlled precisely. Hence, a *quantitative* understanding of the observed contrast is not easily accessible. However, the contrast in the data can be *qualitatively* understood since the characteristic "checker-board" pattern is typically observed in the experiments.

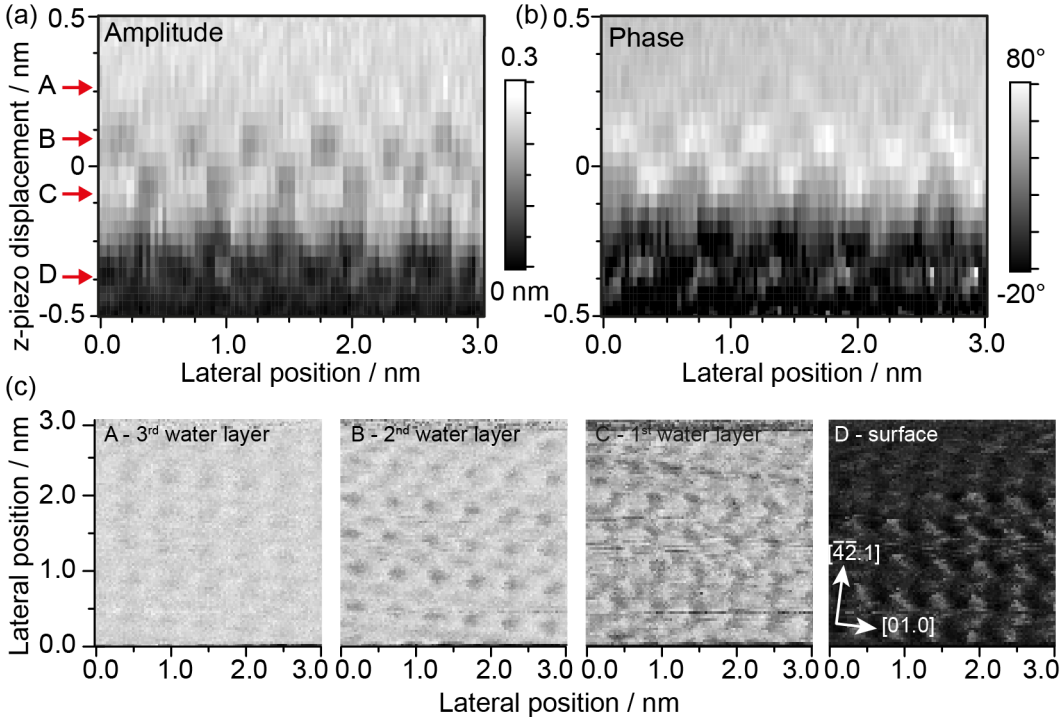

Figure 3.6.: Corresponding 2D slices of (a) the oscillation amplitude, (b) the phase along the [010] surface direction and (c) parallel to the surface extracted from the same 3D map. The positions of the images in (c) are indicated by arrows labelled A-D. All slices in (c) show amplitude data depicted in the same colour scale. Here, the temperature was 304 K, the free amplitude was 0.3 nm, and we used a set-point of 0.7 and a modulation range of ±0.5 nm.

Based on theoretical work, the first hydration layer is assigned to strongly bound water molecules above the calcium ions, while the second layer is attributed to water molecules forming hydrogen bonds towards the surface carbonate groups. Therefore, well-ordered hydration layers in registry with the surface periodicity but with differing contrast are expected. In fig. 3.6, a further AM-AFM measurement of calcite in oversaturated solution is presented. In the 2D slice along the [010] surface direction (fig. 3.6 (a)), the same "checker-board" pattern is visible as in fig. 3.5(a). Besides the strongly bound first and second layer, we can clearly identify a third hydration layer. However, a comparison between the data shown in fig. 3.5 and fig. 3.6, reveals the strong dependence of the visibility of the "checker-board" pattern on the tip and imaging conditions. The third layer is found to be more or less pronounced depending on the (unknown) tip termination and the experimental settings.

The z-axis in the 3D data shown in fig. 3.5 and 3.6 only corresponds to the change in tip-sample distance, which only results from the sinusoidal movement of the z-piezo. The true tip-sample distance change, however, is determined by many more effects, e.g., tip and surface relaxations. Therefore, absolute tip-sample distance distances are experimentally not accessible and only apparent distances can be measured. For the comparison with recent experimental and theoretical work, the apparent distance between the hydration layers in several 2D slices is determined. It is about 0.14 nm between the first and the second hydration layer and about 0.15 nm between the second and the third hydration layer. Imada and co-workers [150] have measured distances of 0.14 nm (between first and second layer) and 0.16 nm (between second and third layer). Kerisit and co-workers have calculated the separation between hydration layers starting from the first layer as follows: 0.10 nm, 0.18 nm, 0.28 nm [153].

2D slices were extracted parallel to the surface (equivalent to constant-height images) at different tip-sample distances from the same 3D map (fig. 3.6 (b)). This allows for a direct comparison of the calcite surface with the first, second and third hydration layer. As expected, all four images in fig. 3.6 (b) show a periodic, rectangular structure commensurate to the surface unit cell of calcite(10.4), as introduced in fig. 3.1. This observation illustrates the strong templating effect of the calcite surface causing the formation of ordered hydration layers.

Identification of the Surface Position

Within the presented data, the three minima are easily identified in the amplitude and phase signal (fig. 3.5 and 3.6). However, an unambiguous assignment of the identified hydration layers requires knowledge about the vertical position of the calcite surface within the 3D map. For this assignment, the amplitude and phase signal are not sufficient to identify the surface in a liquid environment. Typical criteria for physical contact between cantilever tip and surface are usually derived from analysing the damping (FM-AFM) [166] or the static deflection signal (AM-AFM) [80]. To gain detailed insight into the surface position, the relationship between the static deflection signal and the oscillation amplitude as a function of the tip-sample distance is evaluated. The static deflection signal is not monitored within typical dynamic atomic force microscopy (dAFM) experiments, but it contains valuable information about the tip-sample distance [167]. The behaviour of the static deflection in two 3D maps with similar experimental parameters, except for different modulations ranges, is shown in fig. 3.7.

According to Burnham *et al.* [80], three different regimes (I to III in fig. 3.7 (a)) can be distinguished when the tip approaches the sample. Far away from the surface, and regardless of the medium, both amplitude and static deflection are independent of the tip-sample distance (regime I). In regime I, the static deflection is zero. When the tip starts to interact with the surface (regime II), the amplitude decreases. In regime II, the static deflection behaves differently in water and in air. In air, the static deflection remains zero within regime II. In water, the static deflection starts to increase as soon as the amplitude decreases due to interaction between tip and hydration layers. In regime III, upon further approach to the sample, the amplitude remains at a constant low value, while the static deflection increases linearly according to the increasing z-piezo displacement. The same behaviour is displayed in the data (fig. 3.7 (a)).

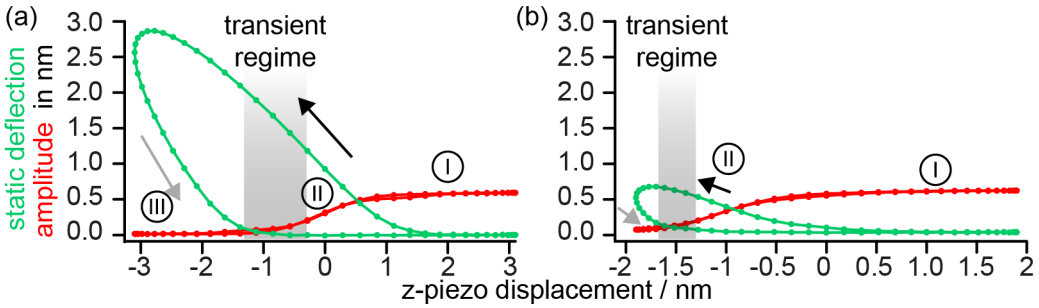

Figure 3.7.: Static deflection and oscillation amplitude curves as a function of the z-piezo displacement. Approach and retraced are indicated by arrows, in black and grey, respectively. The curves are averaged over 120 single curves, i.e., the entire retrace part of a scan line. The corresponding 3D experiments were performed on calcite at ambient conditions with a free amplitude of around 0.5 nm, a set-point of 0.9, a modulation frequency of around 735 Hz and (a) a modulation range of ±3.1 nm and (b) a modulation range of ±1.9 nm.

While in air, the onset of the static deflection coincides with the collapse of the amplitude. Such a clear identification criterion for the surface position is not available in liquid, because the static deflection increases in regime II and in regime III. Nevertheless, it is fair to expect the interaction in regime II to be dominated by the interaction between tip and solution, while in regime III the interaction between tip and surface is dominant. As indicated in fig. 3.7 (a), the transient regime between regime II and regime III may spread over a considerable tip-sample distance range. The amplitude, however, does not change a lot within this transient regime. For the example given in fig. 3.7 (a), the transition between liquid and surface interaction is located at an amplitude of (0.05 ± 0.03) nm. Although the border between regime II and III is hard to locate precisely in z, the determination of the surface position via this method is good enough to assign the hydration layers without any doubt within the amplitude slices. However, this determination is certainly not precise enough to allow for measuring the separation between the surface and the first hydration layer.

In fig. 3.7 (b), the static deflection is shown with a modulation range of 1 nm as typical for the experiments in this thesis. Here, the transient regime is just reached and the static deflection is much smaller as compared to the experiments shown in fig. 3.7 (a). Although the distinct knowledge of the surface position is important information, the direct tip-surface interaction within and after the transient regime is very likely to degrade the tip apex. Furthermore, since the sinusoidal modulation of the z-piezo during the 3D mapping results in closely spaced data points (pixels) around the turning points, a permanent penetration of the tip in regime III is not desirable for high-resolution imaging of the hydration layers. For these reasons, the investigation of hydration layers with the 3D routine typically includes the mapping of the solid-liquid interface with different modulation ranges to ensure both high-resolution imaging and a proper assignment of the hydration layers.

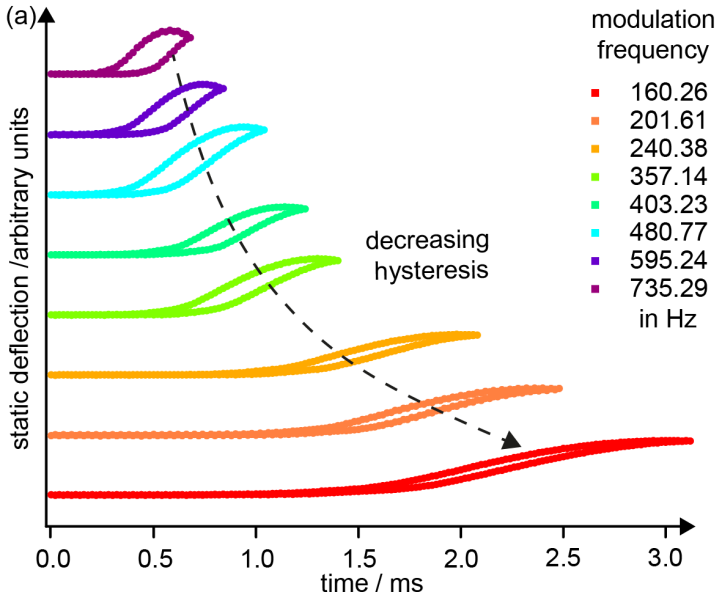

Figure 3.8.: Averaged static deflection data captured with different modulation frequencies, which corresponds to different velocities. The curves are averaged over the first 120 curves. The corresponding 3D experiments were performed on calcite in ambient conditions with a free amplitude of 0.3 nm, a set-point of 0.6 and a modulation range of ±2.0 nm.

The fast data acquisition in the 3D mapping routine leads to a notable hysteresis in the static deflection between approach and retract data (fig. 3.7). When comparing the measurements in fig. 3.7 (a) and (b) that are recorded at the same modulation frequency, it is clear that the observed hysteresis depends on the tip-sample distance. However, mapping experiments with different modulation frequencies clearly indicate that the extent of this hysteresis further depends on the velocity of the cantilever tip (see fig. 3.8). The sinusoidal fashion of the z-movement in the 3D routine leads to a reduction of this hysteresis around the turning points because the z-modulation speed is smallest there. This is the origin of the decrease of static deflection around the point of closest approach.

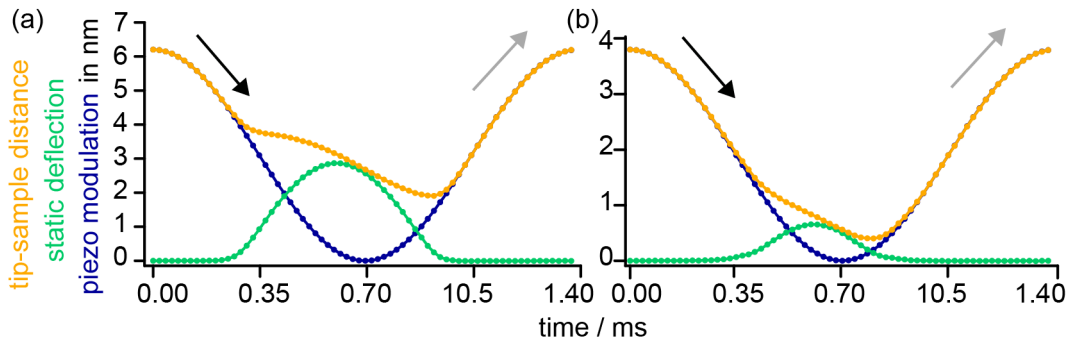

Figure 3.9.: (a) The static deflection, the applied piezo modulation and the corresponding tip-sample distance as a function of time. Approach and retraced are indicated by arrows, in black and grey, respectively. The curves are averaged over 120 single curves, i.e., the entire retrace part of a scan line. The corresponding 3D experiments were performed on calcite at ambient conditions with a free amplitude of around 0.5 nm, a set-point of 0.9, a modulation frequency of around 735 Hz and a modulation range of (a) ±3.1 nm and (b) ±1.9 nm.

Due to the strong hysteresis in the static deflection signal at the used modulation frequencies the tip-sample approach and retract are not symmetric (see fig. 3.9). Additionally, a uncertainty concerning the actual tip-sample distance is introduced by the static deflection [167]. This particular error in positioning can be properly considered in the data evaluation. For the experiments presented in chap. 4 and 5, the spatial position of every single data point is determine by taking the applied z-piezo modulation and the measured static deflection signal into account. Here, linear interpolation is the tool of choice to place the data point precisely at the correct tip-sample distance (a detailed description of this procedure can be found in appendix A).

3.3 Summary and Conclusion

In this section, a straightforward implementation of a state-of-the art 3D mapping technique featuring the most prominent AM-AFM mode is presented. The 3D routine runs on a commercial Cypher AFM and is capable of capturing up to four different channels at high scan speeds. This allows for high-resolution 3D mapping in liquid in ambient conditions. The issue of free amplitude variations due to the drifting "forest of peaks" is addressed and solved by periodically adjusting the excitation amplitude during data acquisition. This opens up a route for the investigation of solvation forces at the solid-liquid interface on various surfaces.

The performance of the set-up is demonstrated by presenting 3D data taken in an aqueous solution on the calcite(10.4) surface. Our data reproducibly reveal hydration layers with distinct patterns with atomic resolution. We can clearly distinguish three hydration layers with a periodic structure commensurate to the calcite surface. The observed "checker-board" pattern as well as the spacing between the hydration layers is in excellent agreement with previous experimental and theoretical results.

From the images in fig. 3.6(c) it is further evident why 3D mapping is clearly superior to standard AFM imaging: From a single AFM image alone it is impossible to deduce whether the surface or one of the hydration layers is imaged. This result further suggests that the occasionally observed sudden changes in contrasts when measuring high-resolution dAFM in liquid on pristine surfaces [136, 168] are simply due to the imaging of different hydration layers.

4 Hydration Layer Mapping on Three Different Carbonates

Naturally occurring carbonates are particularly important as these minerals are highly abundant in the earth's crust [169]. Besides calcite, these are the closely related carbonates: dolomite ($CaMg(CO_3)_2$) and magnesite ($MgCO_3$). The crystal structure of these carbonates is trigonal ($R\bar{3}c$), and their most stable cleavage plane is also the (10.4) surface. Due to the different cation composition, the structure of theses three carbonates differ slightly in the dimensions of the crystal and surface unit cell (see fig. 4.1 and 4.2).

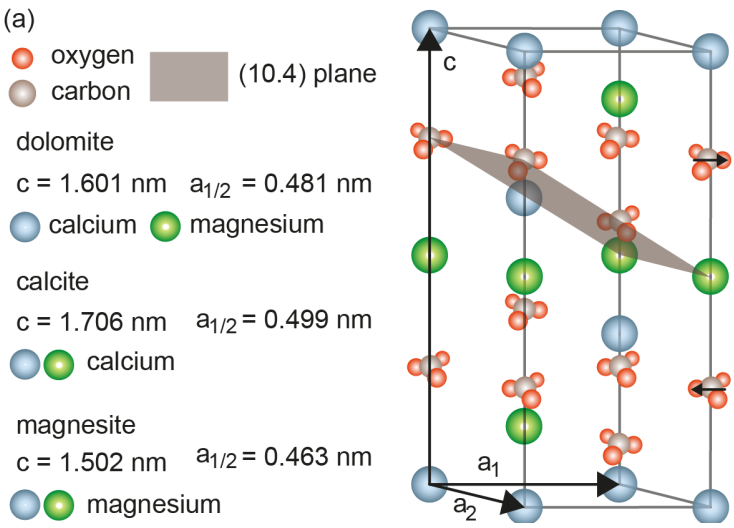

Figure 4.1.: The crystal lattice of the investigated carbonates calcite, magnesite and dolomite. In magnesite and calcite only the correspondent cations form the lattice. For dolomite, both, calcium and magnesite cations occur in the crystal and the different lattice positions are marked with different colours. The lattice constants are take from Graf [146].

Interestingly, while calcite is easily precipitated in the laboratory, the low-temperature, low-pressure synthesis of dolomite and magnesite have virtually proven to be impossible [170–172]. The origin for sedimentary dolomite (and magnesite) therefore remains a puzzle in the literature [173–175]. This so called "dolomite problem" or "dolomite question" quickly arose after its discovery by the French geologist Déodat de Dolomieu [176]. It has been speculated, controversially, that magnesium hydration might play a role in this puzzle [171, 174]; thus, the precise knowledge of the hydrated structures at the solid-water interface might add relevant insights for elucidating the crystal formation process.

Consequently, the behaviour of carbonate minerals in aqueous solution has been studied extensively. Besides atomic-scale imaging [16, 81, 141, 143, 177], a main focus in research is on the kinetic aspects of the dissolution and growth control of carbonate surfaces in a certain (natural) environment [178–180], for instance calcite in saline water [181, 182]. In particular, AFM experiments have largely contributed to understanding these kinetic processes through the direct observation of the carbonate surfaces at the nanoscale. Several AFM studies have addressed the growth and dissolution of calcite [112, 183, 184] and magnesite [185–187]. However, interest is now growing to investigate dolomite in an effort to disclose the secrets of its origin. The surface reactivity of dolomite is even more complicated in comparison to calcite and magnesite due to the different behaviour of calcium and magnesium ions at the solid-liquid interface [188, 189]. The interaction and competition of the hydration shell of the ions with the hydration layer at the carbonate mineral surface is assigned as a basic step within the kinetic of surface morphology [178], which is exemplified in the work by Xu *et al.* [171] and Ruiz-Agudo *et al.* [190].

More recently, the structure of the hydration layers on the (10.4) surface of calcite has been investigated using electrophoretic and streaming potential measurements [149] and surface X-rayscattering [147, 148, 191]. In this context, 3D mapping experiments carried out with the AFM have elucidated molecular-level details of the hydration layers on calcite(10.4) [4, 150, 192]. A so-called "checkerboard" pattern above the surface has been revealed by these studies, providing experimental evidence for *vertical* ordering of the interfacial water into hydration layers that exhibit an additional *lateral* order commensurate with the underlying calcite lattice. No 3D mapping experiments in liquid exist so far for the (10.4) surfaces of dolomite and magnesite.

From the theoretical side, the structure of water on the (10.4) cleavage plane of calcite has recently been studied by molecular dynamics (MD) simulations [73, 153, 155, 192] or other atomistic simulation methods [193]. These studies indicate the formation of three water layers above the (10.4) surface of calcite, in excellent agreement with the experimental results. The simulations further elucidate that the first layer is bound to the calcium cations while the water molecules in the second layer form a hydrogen bond to the protruding oxygen atoms of the carbonate groups. Compared to calcite, only little is known about the adsorption of water on dolomite and magnesite. A comparative theoretical study above the water-carbonate surfaces reveals an increased surface stability relative to the anhydrous surface by the formation of hydrogen bonds between the surface cations and a monolayer of water [193].

In this chapter a high-resolution AFM hydration layer mapping study is presented, which elucidates the atomic-scale details of the water arrangement at the interface of the most stable (10.4) cleavage planes of calcite, dolomite and magnesite. These three mineral surfaces constitute an ideal model system to investigate the influence of changing the lattice dimensions on the resulting interfacial water structure, thus shedding light on the delicate balance of intermolecular and molecule-surface interaction on the formation of interfacial water networks. The presented 3D experiments and complementary molecular dynamics (MD) simulation (provided by P. Spijker *et. al.*) are in preparation for submission as a scientific article [4].

Experimental Preparation

Instrumental Set-up

The AFM experiments are performed under ambient conditions on the Cypher AFM with the very same set-up as described in chap. 3. The free amplitude is calculated by using the sensitivity determined after the experiments. During the study, the Cypher AFM was updated with photothermal excitation (BlueDrive™). As described in sec. 2.2, photothermal excitation is a sophisticated method to drive the cantilever and further improves the stability of the 3D mapping experiments. Therefore, some experiments were performed with piezo-acoustic excitation while others used photothermal excitation.

Sample Preparation

The calcite crystals were purchased from Korth Kristalle GmbH (Germany) and cut into cuboids with a base of $2 \times 4\,\mathrm{mm}^2$ by Vario Kristallbearbeitung GmbH (Germany). Dolomite and magnesite crystals were purchased and cut by SurfaceNet GmbH (Germany). The direction of the crystals was determined by the birefringence of the carbonates prior to each measurement [161]. This allows for an unambiguous assignment of the crystal direction in the acquired AFM images.

All measurements shown here were taken in a solution of 0.5 $\frac{\mathrm{mol}}{\mathrm{l}}$ lithium chloride. The lithium chloride was purchased (*pure analysis*) from Sigma-Aldrich. The deionized water used for preparing the solutions was taken from a system by Millipore GmbH (Germany). The crystal samples were freshly cleaved before each measurement and immediately immersed into the lithium chloride solution.

4.1 Results and Discussion

High-resolution Imaging

The unit cell of the three carbonates has a rectangular shape and the lattice dimensions decrease from calcite 0.81×0.50 nm, to dolomite 0.77×0.48 nm to magnesite 0.73×0.46 nm (fig. 4.2). The systematically changing unit cell originates from the smaller ionic radius of the magnesium cation compared to the calcium cation. An atomic-scale investigation of the dolomite(10.4) surface in pure water with sAFM [177] and in UHV [194] has confirmed the rectangular unit cell, while no atomic resolution has been presented within the literature for magnesite.

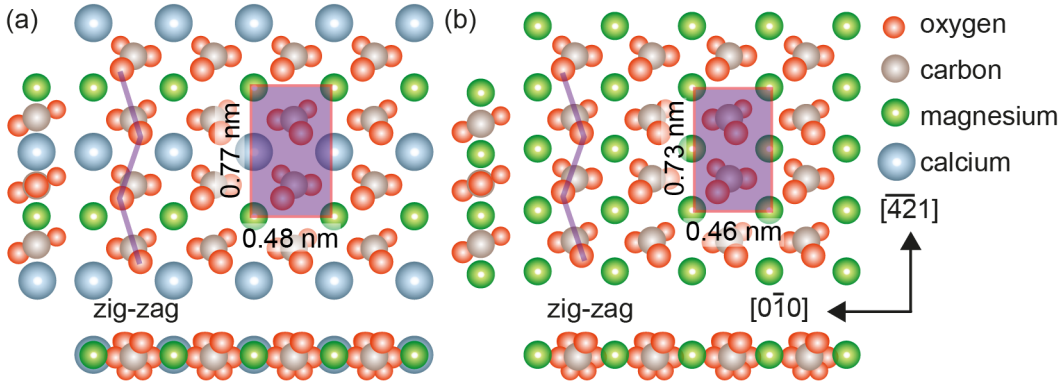

Figure 4.2.: Bulk truncated structure of (a) the dolomite(10.4) and (b) the magnesite(10.4) surface. The unit cell, several surface characteristics and surface projections along the $[010]$ and the $[42\bar{1}]$ are indicated.

Prior to the 3D mapping experiments, the surfaces of dolomite (a) and magnesite (b) are imaged with high-resolution AM-AFM (fig. 4.3). The images are post processed by applying a plane subtraction and a line-wise levelling based on the mean value of a line in the fast scan direction to account for the sample tilt and typical AFM image artefact. The images are obtained on a small scan size of 3×3 nm^2, which is typically used for 3D mapping. The rectangular unit cell can be easily identified and the unit cell dimensions are obtained by a Fast Fourier transformation (FFT) analysis that takes a consecutive series of AFM images into account. The obtained unit cells are $(0.73 \pm 0.05) \times (0.49 \pm 0.05)$ nm for dolomite and $(0.77 \pm 0.05) \times (0.48 \pm 0.05)$ nm for magnesite. The obtained values match the expected values from the bulk structure quite nicely. However, the difference in the atomic lattice for the carbonates is on this small scan scale within the error of the FFT based drift correction. Therefore, the three carbonates cannot be distinguished based on the images presented in fig. 4.3.

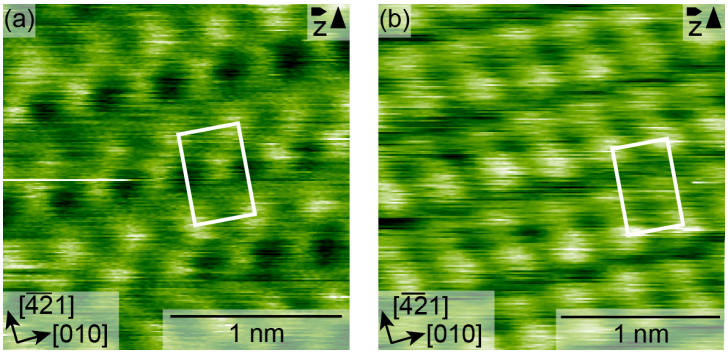

Figure 4.3.:
High-resolution images of dolomite (a) and magnesite (b) in 0.5 $\frac{\text{mol}}{\text{l}}$ lithium chloride solution. The rectangular box marks the surface unit cell.

The "zigzag" structure that is well-known from calcite is only clearly visible for dolomite (fig. 4.3 (a)) but only weakly pronounced for magnesite (fig. 4.3 (b)). However, the "row-pairing" feature along the [010] direction is directly visible within the AFM images of both carbonates. These data display a typical contrast that was obtained with AM-AFM on the Cypher AFM before the 3D mapping experiment.

Mapping Experiments

For each carbonate surface, 3D hydration layer maps were acquired in 0.5 $\frac{\text{mol}}{\text{l}}$ LiCl solution. From these 3D data, vertical (XZ) slices along the $[0\bar{1}0]$ direction are extracted. Representative slices are shown in fig. 4.4 for both the amplitude (left column) and the phase (right column) channel (the point of closest approach is arbitrarily set to zero distance). The graphs next to the amplitude and phase data show the line profiles taken at the position indicated by the blue and red arrows. The occurrence of extrema in the line profiles and the modulation of the intensity in the amplitude and phase slices suggest the existence of an ordered structure of the water molecules above all three surfaces. While the third (topmost) and the second hydration layers can be identified from the occurrence of extrema in the line profiles, the first (closest to the surface) hydration layer is not obvious from the line profiles. However, the first hydration layer is often more visible in the XZ slices. Thus, the combination of XZ slices and the line profiles suggests the existence of *vertical* ordering of the water molecules into three hydration layers for all carbonates. In addition, distinct periodic protrusions in the lower part of the slice indicating the surface according to the criterion derived in sec. 3.2 can be observed, and a *lateral* order is revealed that is commensurate to the underlying carbonate crystal. Hence, the results suggest that the so-called "checker-board" pattern obtained before on calcite [150, 192] is also present on dolomite and magnesite, as regions of large and small amplitude alternate both vertically and laterally (indicated by the blue and red circles).

(a) Calcite

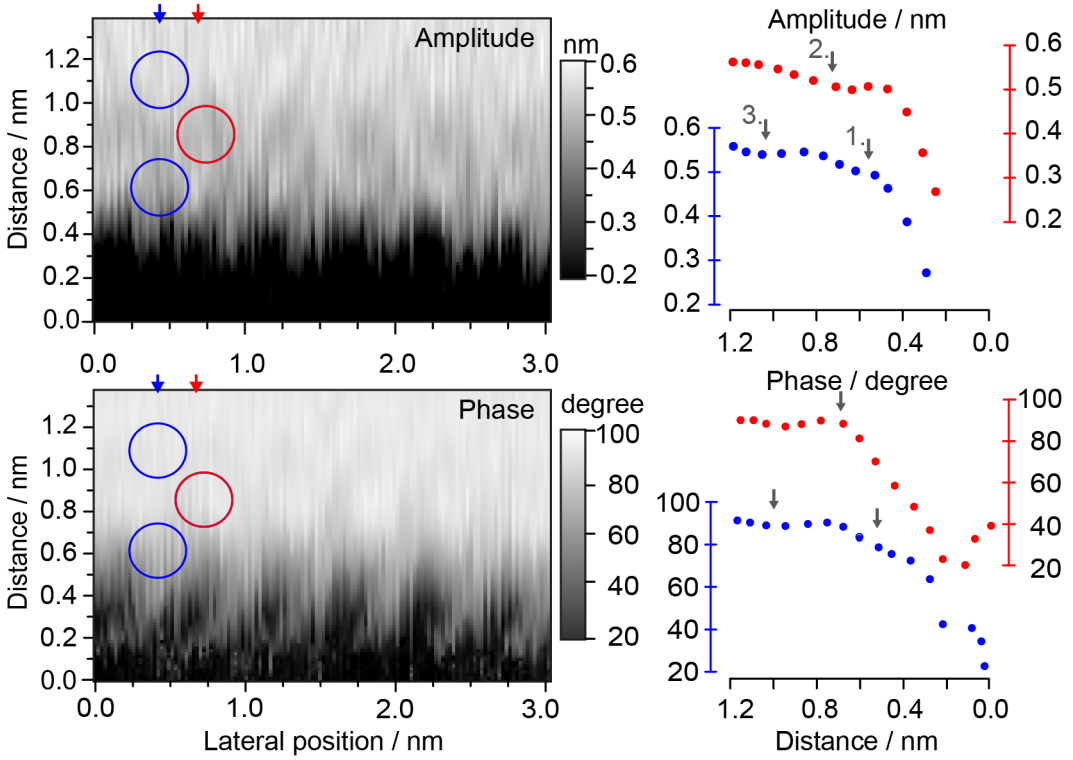

(b) Dolomite

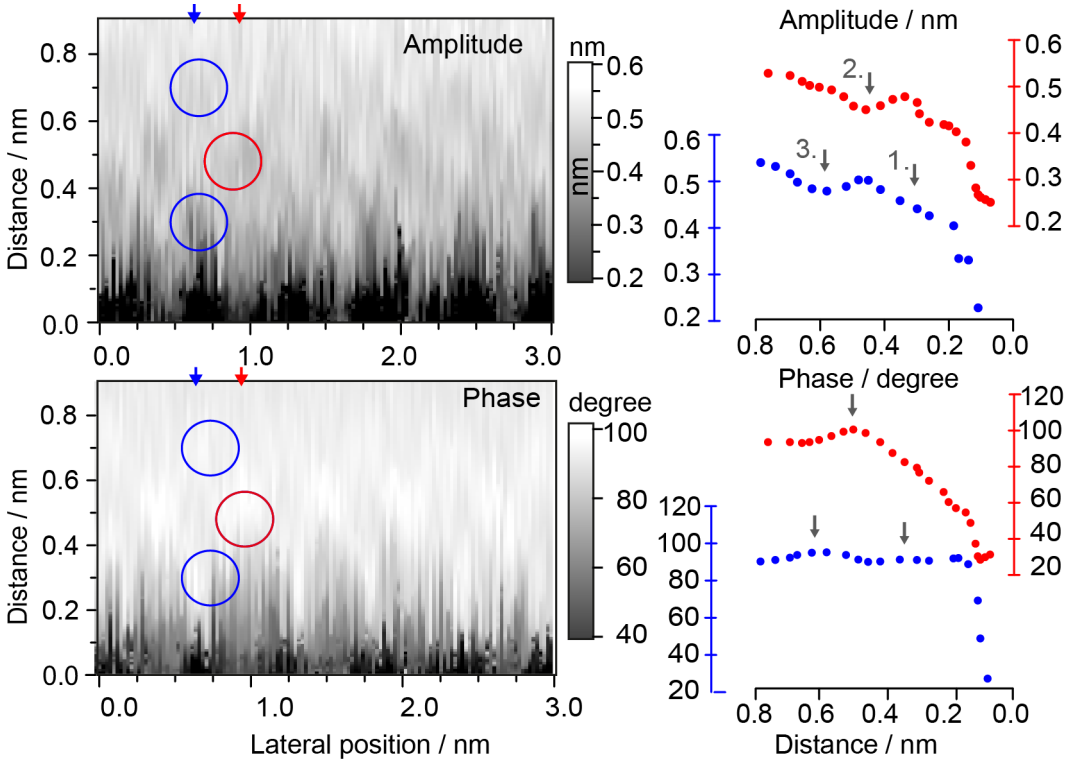

(c) Magnesite

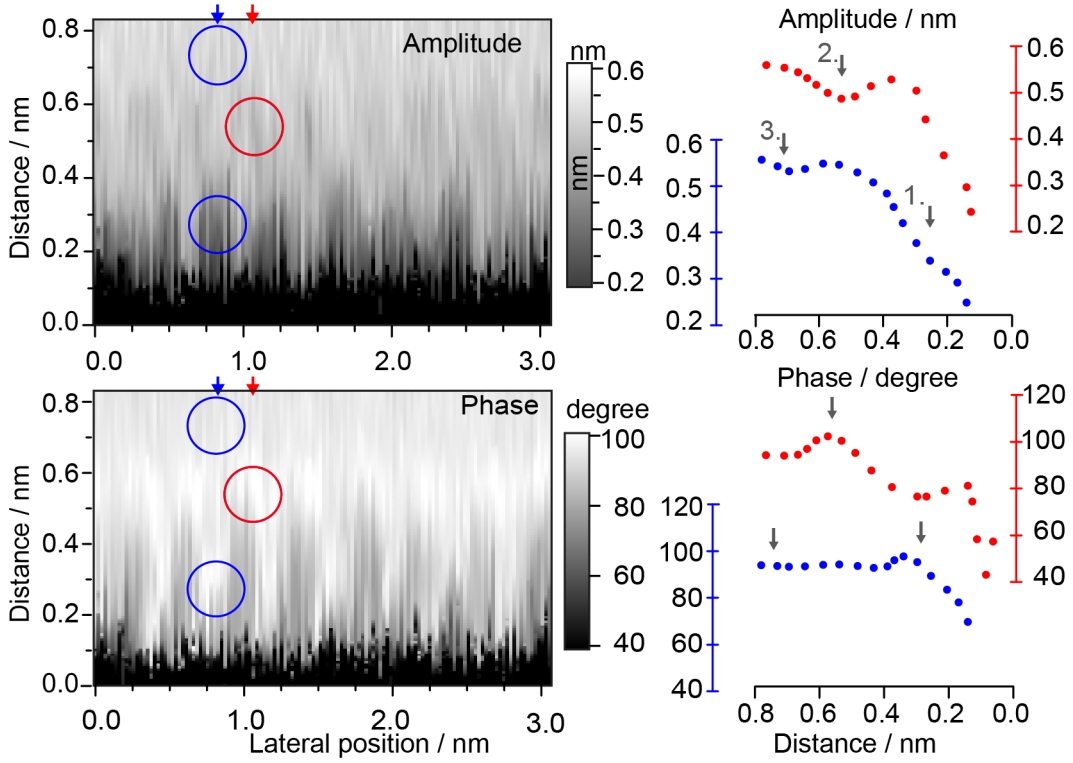

Figure 4.4.: Vertical (XZ) slices along the $[0\bar{1}0]$ direction on the (10.4) planes of (a) calcite, (b) dolomite (piezo-excitation) and (c) magnesite. The line profiles in the panels next to the (XZ) slices are taken at the position indicated by the red and blue arrows. The numbers in the line profiles indicate the hydration layer assignment. The red and blue line graphs are offset with respect to each other to enhance visibility (note their individual axes). The displayed tip-sample distances were corrected for the measured static deflection (sec. 3.2).

It is interesting to compare the contrasts in the amplitude and phase slices for each of the individual carbonates in detail. For instance, in the case of the amplitude and phase line profiles for calcite (blue lines in fig. 4.4 (a), both the first and third extrema are contrast minima. The same line profiles on dolomite (blue lines in fig. 4.4 (b) show minima in the amplitude and maxima in the phase. For the magnesite data, the same situation is obtained as for calcite. In AM-AFM, phase and amplitude changes reflect both dissipative and conservative forces, making an intuitive quantitative understanding difficult and the assignment of water molecules to dark/bright features in amplitude and phase remains ambiguous. This is why the question, as to where the water molecules are positioned, cannot be addressed. However, both vertical and lateral modulation are clearly visible in the data, which allows to unambiguously deduce vertical and lateral ordering of the interfacial water molecules.

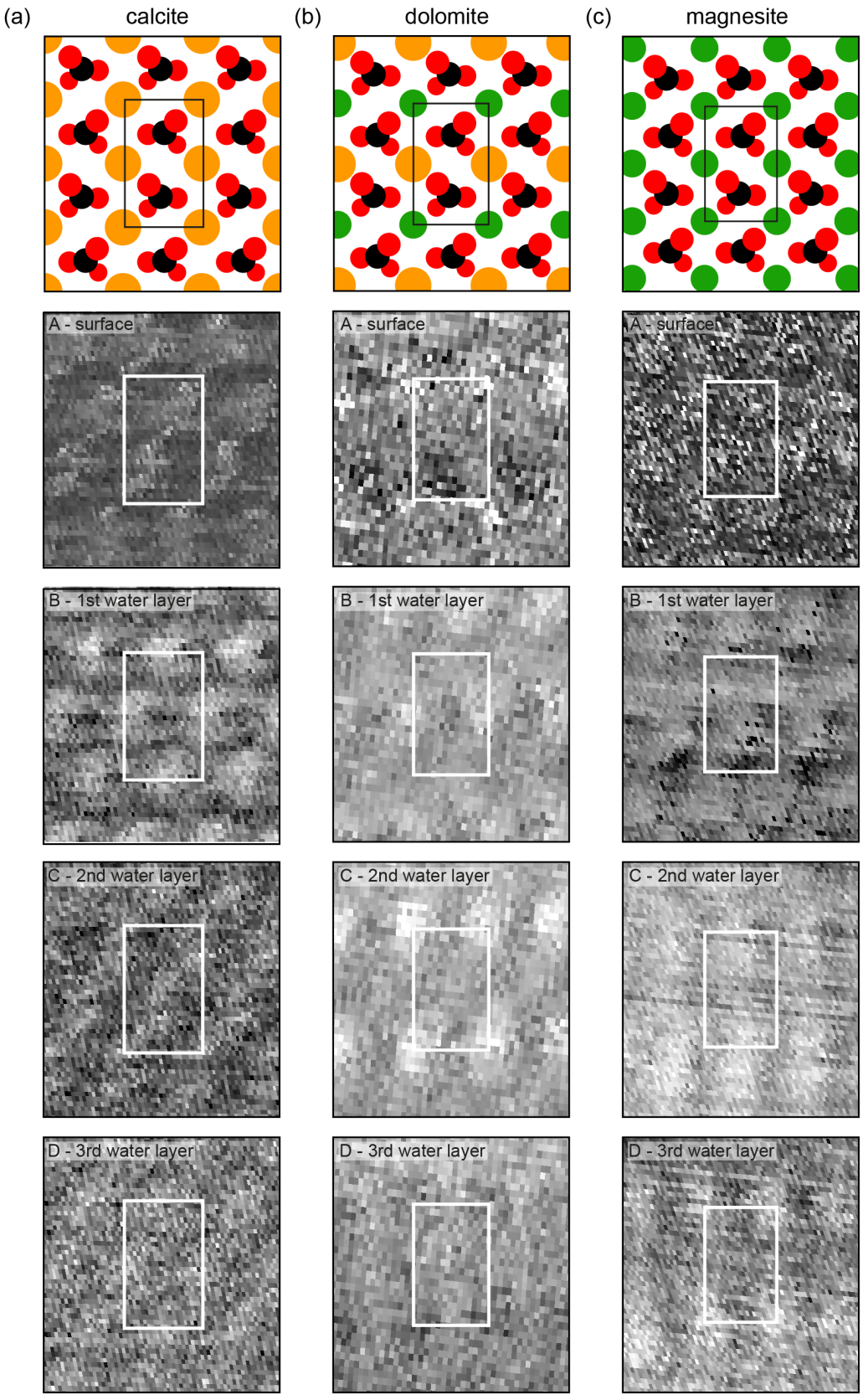

Figure 4.5.: Drift-corrected lateral (XY) slices from the phase signal for (from up to down) the surface and each of the hydration layers as extracted parallel to the (10.4) surface for (a) calcite, (b) dolomite, and (c) magnesite. On top, the schematic structure of the (10.4) surface for each carbonate mineral is shown, including the surface unit cell. The lateral phase slices are corrected for thermal drift based on the known lattice dimensions. The slices are sections of 3D data, originality taken with a scan range of $3.0\,\text{nm} \times 3.0\,\text{nm}$.

Based on the assignment of the surface position and the different hydration layers indicated in fig. 4.4 (small grey arrows), XY slices parallel to the carbonate surfaces at the position of the surface and each hydration layer are extracted. For an easier comparison between theory and experimental data, the XY slices (i.e., images parallel to the surface) shown in fig. 4.5 cover the same area as the schematic surfaces shown in the leftmost column. Furthermore, the experimental data are corrected for thermal drift based on the known lattice dimension of the three carbonates; i.e., the vectors of the measured unit cell are adjusted to coincide with the unit cell dimensions of the respective carbonate mineral. It is important to note that this correction does not change the relative position of the hydration layers with respect to the surface because the thermal drift does not affect the structures relative to each other. Therefore, the observed periodic structure in all three hydration layers demonstrates the strong templating effect of the underlying structure, enforcing a commensurate pattern that is seen for all carbonates even in the third hydration layer.

Molecular Dynamic Simulations

To provide further insights into the arrangement of the water molecules on the different carbonates, a collaboration with the group of [redacted] (SIN, Aalto University, Finland) was established. The following MD simulations represent the current status of this collaboration and are kindly provided by [redacted] [195].

The simulations consists of a box with a seven-layer crystal (of the respective carbonate) solvated on either side of the (10.4) surface by ample water, such that far away from the surface bulk properties can be reached. For all simulations, the large scale molecular dynamics code LAMMPS [196] was used. The simulations were run in parallel on a typical Linux commodity cluster, and analysis was performed visually using VMD [197] or numerically using the Python library MDAnalysis [198]. An accurate force field for calcite simulations has been used [155] in combination with a recently developed extension, which allows for the modelling of dolomite and magnesite [199]. For water, the single point charge flexible model was used (SPC/Fw) [200]. Each simulation consists of a similar protocol. First, the seven-layer crystal is modelled as if it is a bulk crystal in order to relax the initial scaling. Subsequently, the crystal is placed in a larger box with the water molecules. In the next step, the entire system is allowed to relax for at least 50 ps (using a 1 fs time step) at ambient conditions (310 K and 1 atm). After that, a longer run (0.5 ns) is performed to allow for the hydration layers to form. The next 8 ns are the simulation production run, where each 2.5 ps a snapshot of the system is saved to the hard drive and used for subsequent analysis.

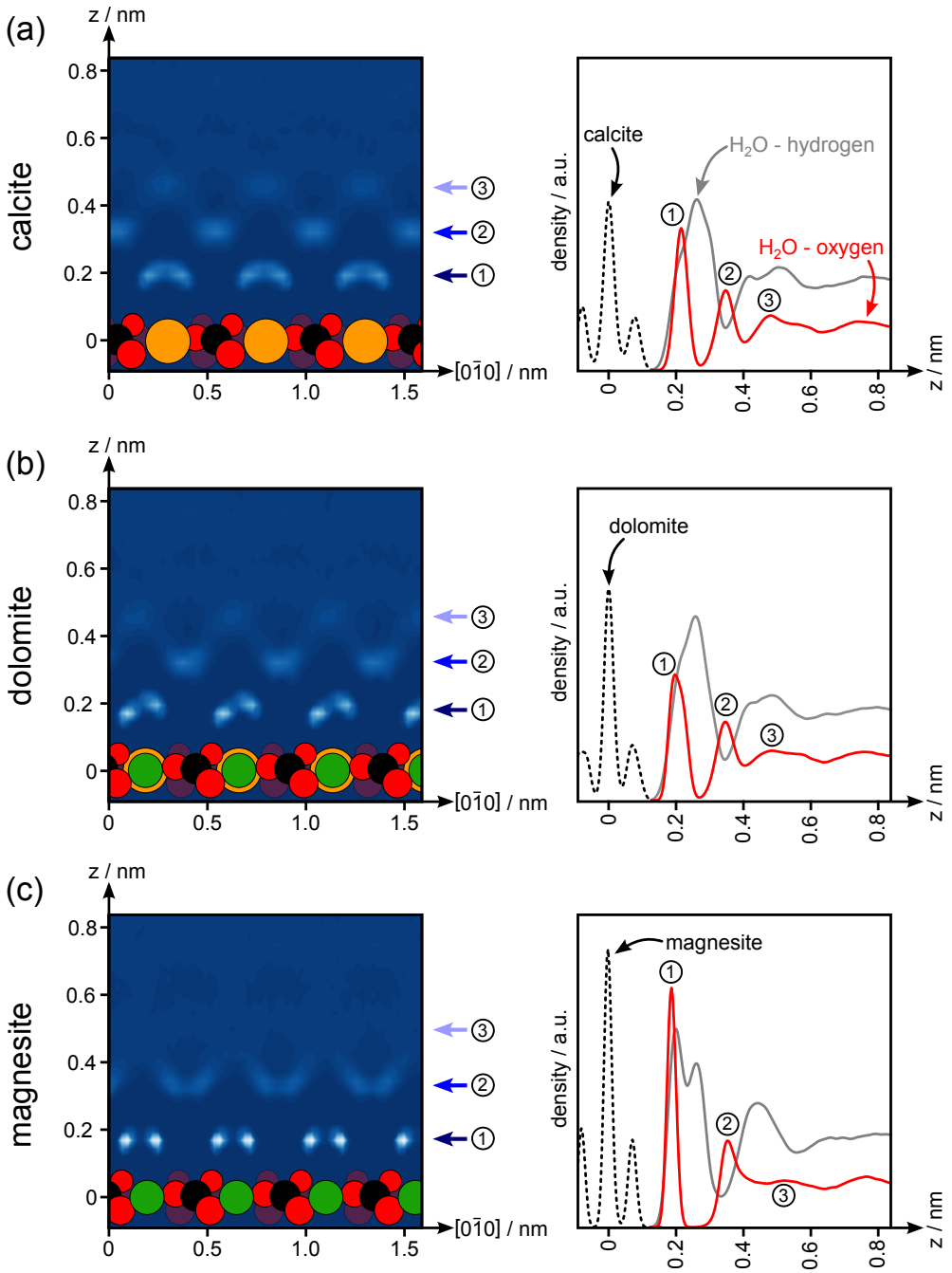

Figure 4.6.: The water oxygen density distribution from the MD simulations in an (XZ) slice along the $[0\bar{1}0]$ direction (left panels) and for the entire (10.4) plane (right panels) is shown for (a) calcite, (b) dolomite, and (c) magnesite. The colour scale for both the XZ density distributions and line graphs for all carbonate surfaces is the same, with white indicating a high density and dark blue a low density. For each carbonate surface, the three hydration layers are indicated in both the (XZ) density distributions and line graphs.

Similar to the experimental XZ slices for the amplitude or phase, density slices along the same $[0\bar{1}0]$ direction can be calculated for each of the carbonates (see fig. 4.6). In contrast to the experimental slices, in the simulations the exact position of the surface atoms is known and indicated in the density plots. Furthermore, the theoretical slices are an average over five unit cells (in the $[42\bar{1}]$ direction), whereas the experimental slices are roughly 0.3 nm thick. From these simulated density slices the same "checker-board" pattern (especially clear for the second and third hydration layer) as in experiments can be observed. When comparing the density slices for each of the carbonates, the influence of the change from calcium to magnesium for dolomite and magnesite is clearly visible.

For calcite (fig. 4.6 (a)), the water molecules in the first hydration layer are located above the calcium ions but also follow the zigzag of the of the carbonate groups along the $[42\bar{1}]$ direction. This is because the single water molecules are oriented towards the protruding oxygens of the carbonate groups, explaining the two "tails" these higher density areas contain. In the dolomite case (fig. 4.6 (b)) the appearance of the magnesium breaks the symmetry of the first hydration layer, with the water molecules above magnesium slightly closer to the surface (left "tails"). This small difference in the vertical displacement above calcium and magnesium should, in principle, be accessible with the AFM. However, such small differences in the vertical displacement might be extremely difficult to detect. For magnesite (fig. 4.6 (c)) the symmetry is restored, but the density spots are more localised than for calcite. This stronger localisation for magnesite can also be observed from the perpendicular density line graphs (right panel in fig. 4.6) as the water-oxygen density peaks are much higher and less wide than for calcite (the area under the curve remains the same though, indicating that the same number of water molecules is bound to the surface). From the same line graphs, the three different hydration layers can also be inferred by identifying three extrema of the water-oxygen density profile.

From the MD simulations, the XY water density distributions parallel to the (10.4) surface is extracted for each of the three identified hydration layers (see fig. 4.7). These densities are calculated for the final 5 ns of the simulation, with a focus on the location of the oxygen atoms only. In order to be able to clearly see the underlying crystal in fig. 4.7 the zero density is drawn transparent. As a consequence of the surface templating, for each of the carbonates the typical zigzag pattern induced by the alternating protruding carbonate oxygens is clearly visible in the first hydration layer.

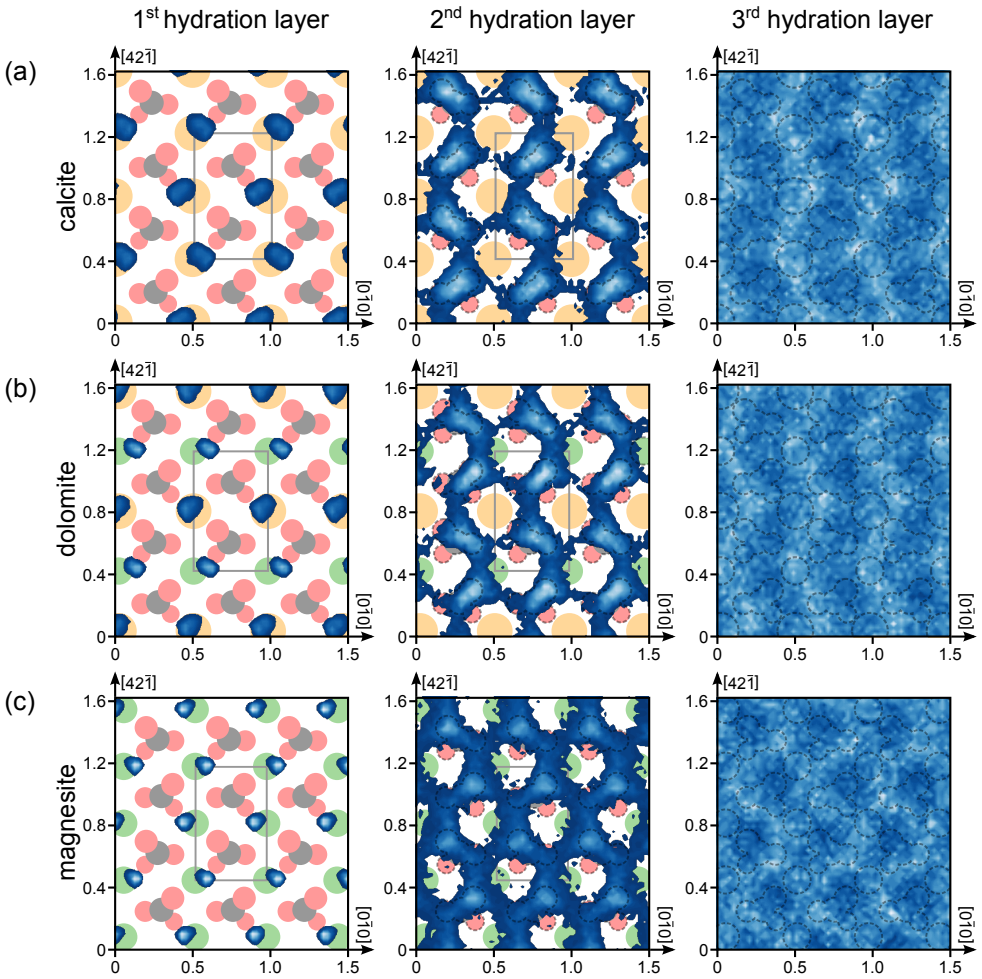

Figure 4.7.: The water (oxygen atoms only) density distribution from the MD simulations for (a) calcite, (b) dolomite, and (c) magnesite showing the first (left), second (middle) and third (right) hydration layer. Here, white indicates a high density and dark blue a low density (the zero density is drawn transparent). However, for each subsequent hydration layer the colour scale is renormalised in order to show significant contrast. The underlying crystal structure is also shown (either in colour or as dashed lines).

In previous work on monolayers of water, the zigzag structure has been observed on each of the carbonate surfaces, but for magnesite, a pairwise structure has been observed [174]. In the latter work, arguments to describe this difference have been based on the fact that the water molecules on the carbonate surfaces with a larger surface unit cell (calcite and dolomite) cannot form hydrogen bonds between themselves, but only with the surface; whereas, intermolecular hydrogen bonds should be possible for magnesite. Clearly, the presence of bulk water changes this hydrogen bonding behaviour, making it now possible for magnesite to remain in the zigzag structure, but has consequences for the other hydration layers where a different structure is observed for magnesite.

In all cases, it is clear that the crystal structure templates the water structure above it. From the intensity of the density it can also be seen that the water is more localised on magnesite (bright white peaks) than it is on calcite (similar to the observations from fig. 4.6), but also that the first layer is a lot more confined in space than the third layer. Furthermore, in the dolomite case, two different absorption spots can be identified for water in the first hydration layer: A) near magnesium and B) near calcium. The same spot assignment can be used for both calcite and magnesite, but as these two carbonate surfaces are formed by one type of the cation exclusively, the difference between the spots is based on the direction of the in-plane carbon-oxygen bond from the nearby carbonate. For spot A this bond is pointing in the $[010]$ direction and for spot B in the $[0\bar{1}0]$ direction.

So far, the simulation data presented focused on local or global density distributions based on the oxygen atoms from the water only. However, this does not give direct insight into the orientation of the water molecules because the hydrogen atoms need to be taken into account as well. For each water molecule in the first layer (at any given time during the entire simulation) the molecule dipole was computed and projected onto the (10.4) surface. To elucidate the orientation of the water molecule, the probability of the angle of this projection with respect to the $[010]$ direction was extracted (fig. 4.8). Here, a dipole-surface angle of $0°$ means the dipole vector is pointing along the $[010]$ direction, whereas an angle of $-180°$ or $180°$ means it is pointing in the opposite direction (see the left most inset in fig. 4.8 (a)).

From the lateral (XY) density distribution (fig. 4.7), the two different absorption spots A and B (see inset in fig. 4.8a) can be easily assigned. When separating the dipole-surface angle based on these absorption sites, we can clearly see how the water changes its orientation depending on which ion it is nearest to. As is not unexpected, the angle distribution for both calcite and magnesite is symmetrical with respect to zero degrees; for dolomite it can be observed that the water molecules near spot B (calcium) behave exactly like as they do on calcite, but the water molecules near spot A (magnesium) try to reach the same orientation as for magnesite, but due to the larger unit cell and the surrounding water molecules they cannot fully achieve this. It also follows from this graph that the water on magnesite is more confined as compared to calcite and dolomite. This follows from the fact that in the case of calcite and dolomite the region around $0°$ shows a significant angle probability, but not in the case of magnesite. In other words, in these examples a larger surface unit cell results in more orientation freedom for water.

Even though the analysis of the dipole-surface angle gives us some insight into the orientation of the water molecule, it does not give us the full picture. Thus, in fig. 4.8 (b)) the average, most probable, orientation for each water molecule in the first or second hydration layer above a surface unit cell is schematically depicted. However, because of the thermal oscillations in the system, water molecules can adopt many possible configurations, even in the first and second hydration layers. It can be seen that in the case of calcite and dolomite the water molecules in the first hydration layer have one OH-bond more or less parallel to the (10.4) plane and one pointing at an angle of approximately 30° along the surface normal. These in-plane hydrogen atoms can choose two possible equally likely locations on either side of the $[010]$ vector, and is flipping between them during the dynamics. For magnesite, on the contrary, the water molecule lies entirely parallel to the (10.4) plane, preventing any flipping behaviour, and as such, it makes the water more confined. The water molecules in the second hydration layer all have one of their hydrogen atoms pointing towards the surface to form a hydrogen bond with the protruding surface oxygen atom. Around this downward-pointing hydrogen bond, the water molecules in the second layer experience almost complete rotational freedom in the case of calcite and dolomite. Again, this is different for magnesite, where a slight favour is found for the direction indicated in fig. 4.8(d)). The water molecules in the third layer (not shown in fig. 4.8) are still confined in z-direction (see fig. 4.6), but have no preference for any orientation (as would be the case in bulk water).

From the MD simulations, the average binding energy can be extracted for the water molecules towards the surface and towards the other water molecules within the layer. These values allow for elucidating the influence of the subtle balance between intermolecular and molecule-surface interactions on the resulting hydration layer structure. As mentioned before, the MD simulations indicate that the water molecules are more strongly localized above the magnesium as compared to the calcium ions; indeed, a 30% higher adhesion energy for water towards magnesite ($-114.3\ \frac{\text{kJ}}{\text{mol}}$) than towards dolomite ($-88.76\ \frac{\text{kJ}}{\text{mol}}$) and calcite ($-81.64\ \frac{\text{kJ}}{\text{mol}}$) is found.

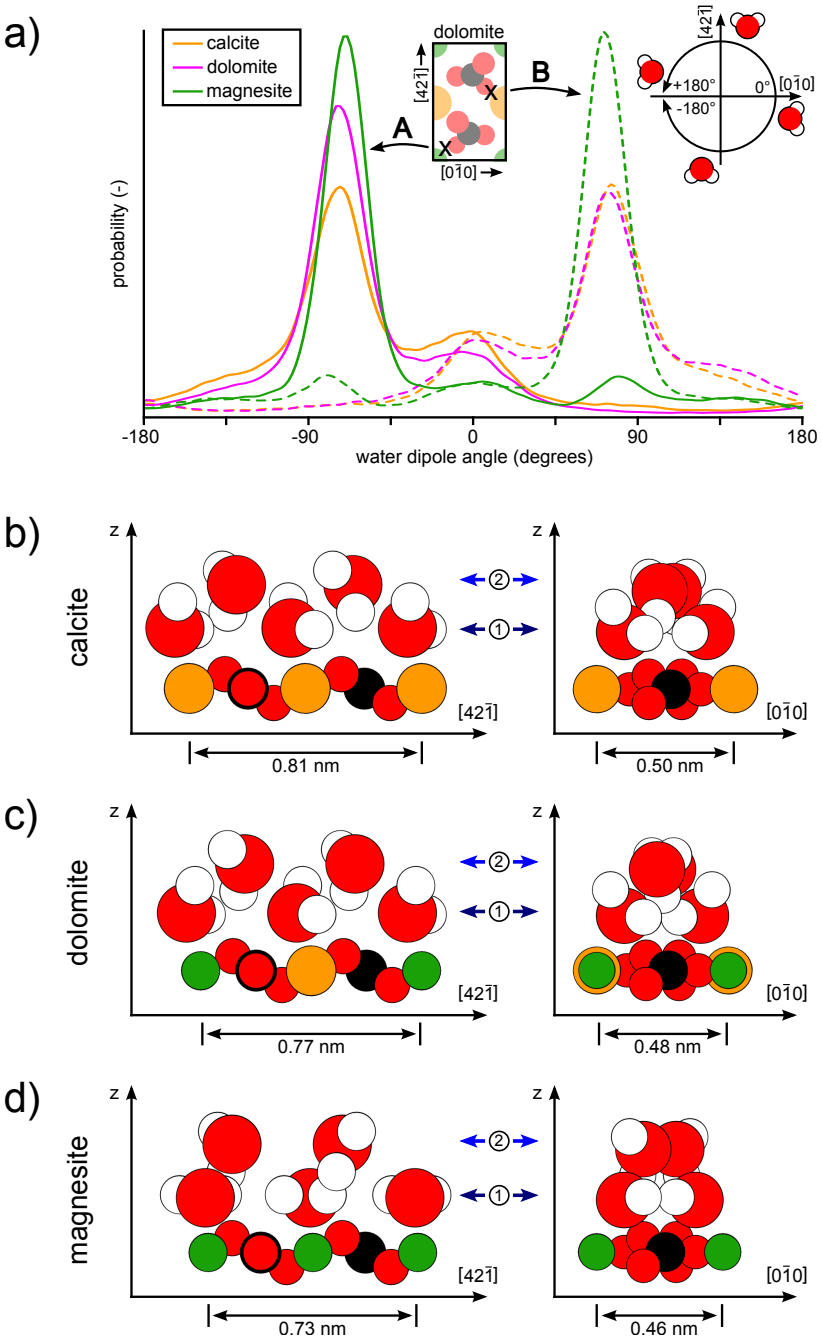

Figure 4.8.: Analysis of the orientation of the water molecules near the carbonate surfaces. In (a) the probability distribution of the angle the water dipole vector makes with the surface normal is shown for each carbonate. The two different spots A and B (see text) on the surface are indicated by the solid or dashed lines, respectively (and also explained by the centre inset). The definition of the angles with respect to the surface orientation is depicted in the upper left hand corner. In (b)-(d) cartoon representations (side views along the two principal unit cell directions) of the average, most probable, orientation of the water molecules for the first and second hydration layer are shown for each of the three carbonates. The size of the unit cells and the hydration layer are indicated.

4.2 Summary and Conclusion

High-resolution AFM images demonstrate a rectangular unit cell with lattice dimensions that corresponds to the bulk truncated structure. Furthermore, using 3D hydration layer mapping, we present experimental evidence for the existence of three hydration layers on the (10.4) surfaces of calcite, dolomite and magnesite. Moreover, besides this *vertical* ordering, a *lateral* order is obtained, which is commensurate to the underlying crystal lattice. These results demonstrate that the so-called "checkerboard" pattern observed earlier on calcite also forms on dolomite and magnesite, despite their different surface unit cell dimensions.

The existence of these hydration layers is confirmed by MD simulations. The simulations elucidate that on both calcite and dolomite the water layers resemble the zigzag pattern of the protruding oxygen atoms of the surface even in the second and third layer. Interestingly, due to the surface unit cell dimensions, intra-layer hydrogen bonds are largely prohibited for these two surfaces. On magnesite, in contrast, this situation is qualitatively different. Here, the arrangement of the water molecules in the first layer is dictated by the position of the protruding oxygen atoms of the surface. However, due to the smaller surface unit cell the molecules are now able to also form intra-layer hydrogen bonds.

In conclusion, this work unravels the decisive influence of the underlying crystal lattice dimensions on the formation of hydration layer networks. It is demonstrated that a strongly bound network is possible only in case of matching lattice dimensions and breaks down as long as strong molecule-surface interactions dominate the water arrangement.

5 Solvation Layer Mapping in Different Alcohols

The interplay between solvent molecules, calcite surface and organic/bio- molecules in a natural environment has attracted considerable interest as an area of research due to the importance of calcite in a range of fields, such as biomineralization [39], geochemistry [139] and oil recovery [140]. In particular, the interaction of (bio)molecules with the calcite surfaces in a natural environment is pivotal for understanding the processes that govern the function of calcite in these fields. Consequently, the interaction of various organic molecules with these surfaces has been studied extensively, and AFM imaging has been used to obtain real-space information on molecule adsorption and structure formation both under UHV [201–204] and liquid conditions [205, 206]. An important group of biomolecules that are known to interact with the calcite surface are polysaccharides, such as coccolith, [7] and fatty acids, such as stearic acid [8]. In order to study these biomolecules with hydroxyl groups (-OH) and hydrophobic functionalities, 3D mapping with AM-AFM is used with three simple model molecules, namely, ethanol, methanol and propan-1-ol. To simplify the experimental conditions for the 3D mapping set-up, the alcohols are used directly as the solvent to study the molecular arrangement at the interface.

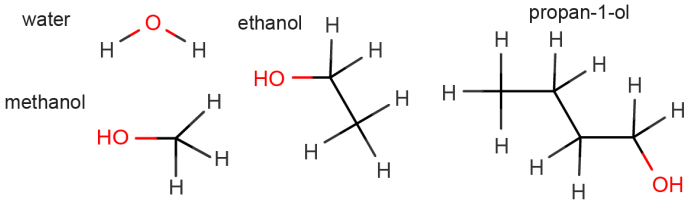

Figure 5.1.: The chemical structures of the investigated alcohols: methanol, ethanol, propan-1-ol in comparison to water.

The arrangement of water molecules on the natural cleavage plane of calcite has been studied extensively, both by theoretical [73, 153–156] and experimental methods [147–152]. However, only a few studies, often in combination with MD simulations, report about experiments on the interface of calcite and ethanol using X-ray reflectivity (XR) [207], X-ray photoelectron spectroscopy (XPS) [208] and AFM [209–211]. Their results suggest the formation of a single and well-defined adsorption layer of ethanol above the calcite surface. A less ordered and less strongly bound second ethanol layer has not been confirmed experimentally, although theoretical calculations suggest its existence [207, 210, 211]. More recently, two studies investigated the arrangement of other alcohols at the calcite surface, namely, Bovet *et al.* [208] for methanol, pentanol tert-butanol by XPS and MD simulations; and Imada *et al.*

[212] for iso-propanol by the means of high-resolution FM-AFM mapping. Their results show that all studied alcohols arrange in the same orientation on the surface, following the example of ethanol, suggesting the very same kind of interaction. However, due to the difference in their dimensions, the surface coverage decreases from the small to the larger alcohols [208].

Experimental Preparation

Instrumental Set-up

The AFM experiments are performed under ambient conditions with the Cypher AFM in the same set-up as described in chap. 3. Due to the fast evaporation of the alcohols, the AFM measurements were interrupted from time to time and the liquid cell was refilled with fresh solvent. The level of the solvent was carefully checked during the measurement time to protect the mineral surface from completely drying out. The evaporation times range from 15 to 20 min for methanol, to 20 to 25 min for ethanol, to 30 to 40 min for propan-1-ol. The fast evaporation of the alcohols compared to water causes an increase in the thermal drift, as well as accelerates the movement of the drifting "forest of peaks". Due to the short timespan it is not possible to wait for the AFM set-up to equilibrate as in the case of measurements in water. In consequence, high-resolution AFM imaging and 3D mapping is severely hampered in the open liquid cell, and stable atomic resolution is very difficult to achieve. 3D maps are often distorted by drift and frequent tip changes. For the experiments presented in this chapter, both photothermal and piezo-acoustic excitation were used. The free amplitude is calculated by using the sensitivity determined after the experiments or an averaged value of 22 $\frac{\text{nm}}{\text{V}}$.

Sample Preparation

Absolute ethanol ($\geq$ 99,8 %) was purchased from Carl-Roth GmbH (Germany) and VWR International GmbH (Germany). Methanol ($\geq$ 99,95 %) and propan-1-ol ($\geq$ 99,5 %) were purchased from Carl-Roth GmbH (Germany). Calcite was purchased from Korth Kristalle GmbH (Germany) and cut into cuboids with a base of $4 \times 4\,\text{nm}^2$ or $4 \times 2\,\text{nm}^2$ by Vario Kristallbearbeitung GmbH (Germany). The [010] direction of the crystals was determined based on the birefringence of the carbonates prior to each measurement [161]. The samples were freshly cleaved before each measurement and immediately immersed into the solution.

5.1 Results and Discussion

Mapping Experiments

3D maps were acquired in methanol, ethanol and propan-1-ol on calcite and analysed by comparing vertical (XZ) slices of amplitude and phase along the [010] direction (fig. 5.2). For a direct comparison, the data obtained in water (discussed in detail in chap. 4) are also included in the figure. The displayed tip-sample distance is corrected for the measured static deflection data as described in sec. 3.2, and the point of closest approach is arbitrarily set to zero distance. For the assignment of the surface position; i.e., the transition between liquid and surface interaction, the previously derived criterion based on amplitude and static deflection is used. For the measurement in water presented in fig. 5.2a, the surface position was assigned to an amplitude of (0.15 ± 0.05) nm. In this (amplitude) regime (around (0.20 ± 0.05) nm distance) an alternating pattern is visible, which is attributed to the corrugation of the surface. Next to the XZ slices of amplitude and phase, line profiles taken between two surface protrusions (blue arrow) and above a surface protrusion (red arrow) are shown. The vertical and lateral order (marked by cycles) for the hydration structure in water, the typical "checker-board" pattern, is clearly visible in amplitude and phase; and the three hydration layers can be readily identified (see fig. 5.2a). Again, the third and second hydration layer can be more easily identified in the line profiles, while the first hydration layer is more visible in the XZ slices.

In fig. 5.2b the experimental data of methanol are presented, and the surface position is assigned at an amplitude of (0.10 ± 0.05) nm. Based on this surface position, the observed minima in the site-specific line profiles are identified and marked with small grey arrows. For comparison, the arrows are also shown at the very same position in the line profiles of the phase signal. The most prominent feature in the amplitude data is the first minimum, clearly visible in both the XZ slice (marked with a red cycle) and the line profile (marked with the number one), which corresponds to a maximum in the phase signal. This feature clearly displays a lateral order and suggests the presence of a highly ordered layer of methanol molecules above the calcite surface. Still, the contrast formation in AFM is very difficult and does not allow for an unambiguous assignment of the observed feature to the positions of the molecules. In the line profiles of both the amplitude and the phase, further minima can be observed. In contrast to water, no lateral order can be observed for these minima in the XZ slices of amplitude and phase. However, in line with the outer hydration layers of water, these minima are much harder to observe. Furthermore, they are much more visible in the XZ slices of the phase than in the amplitude.

(a) Water

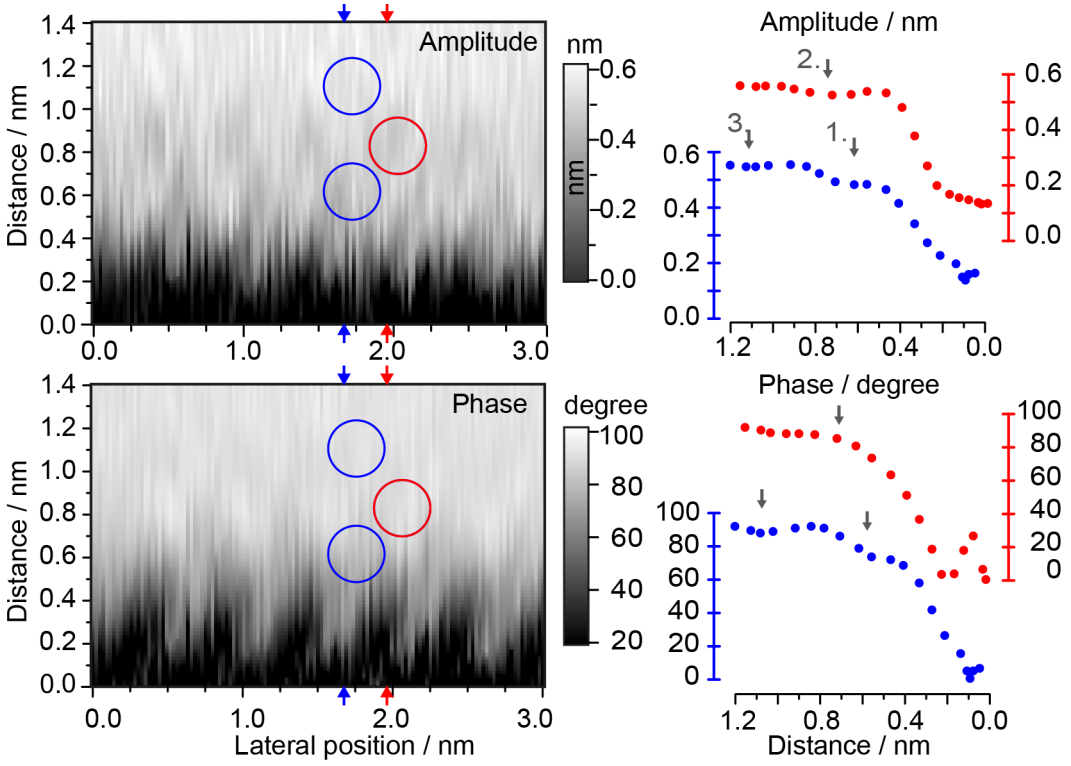

(b) Methanol

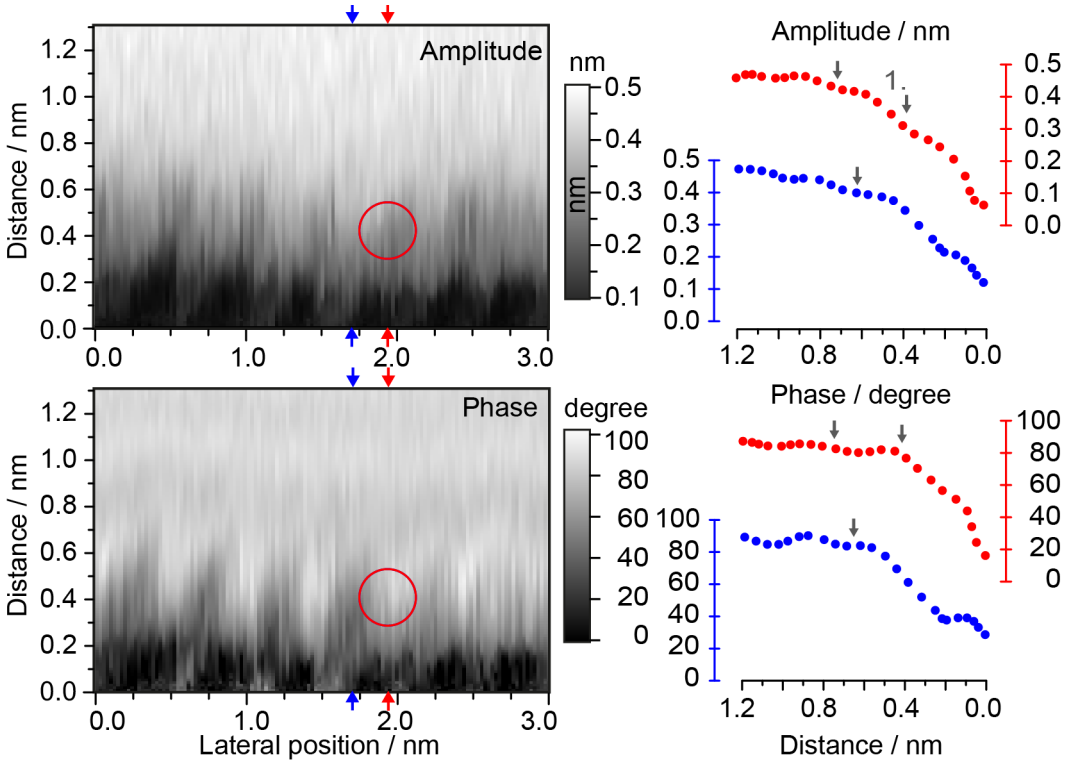

(c) Ethanol

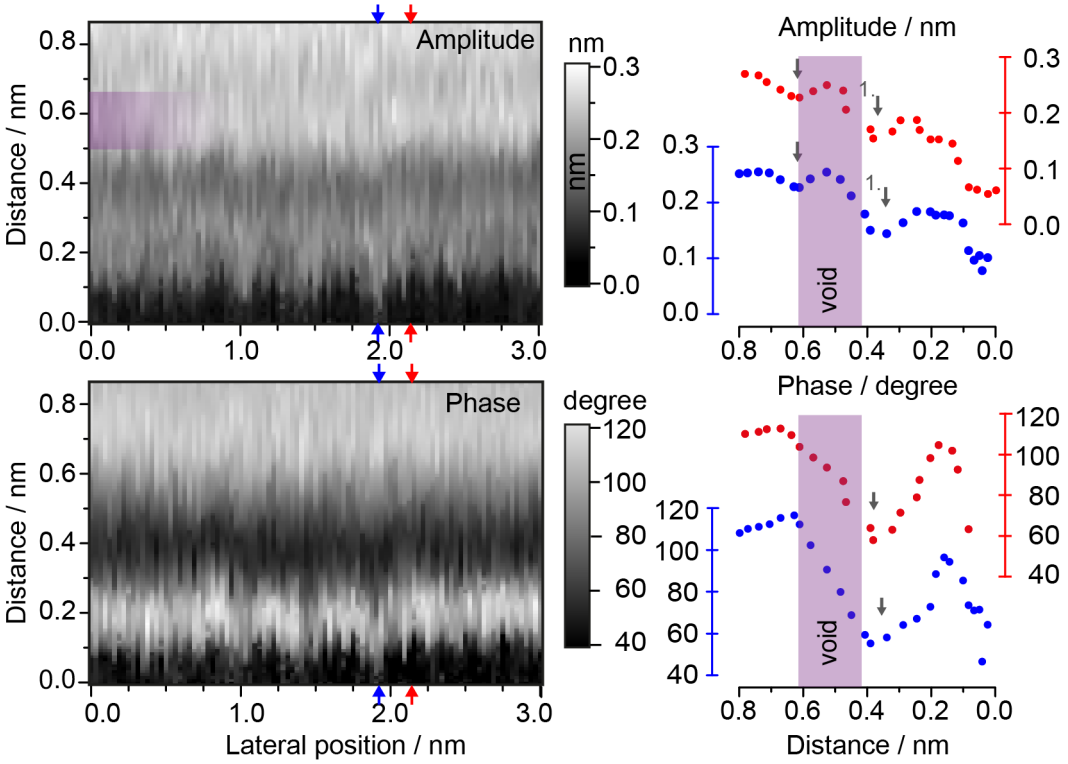

(d) Propan-1-ol

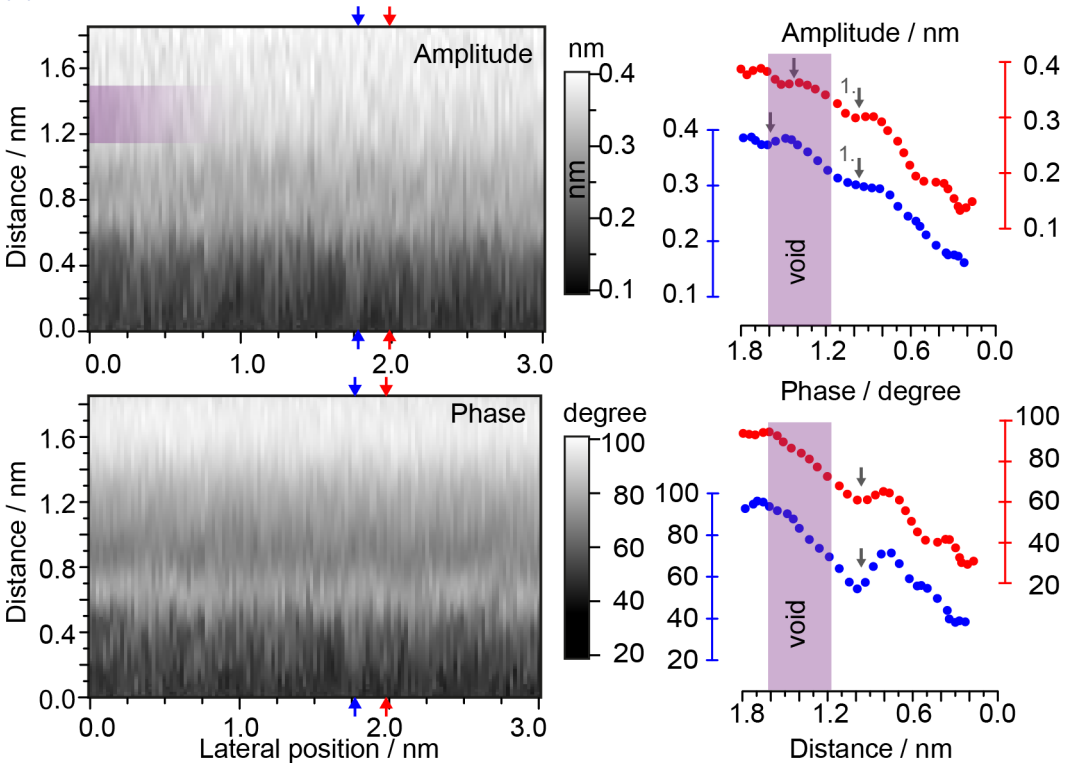

Figure 5.2.: Vertical (XZ) slices along the [010] direction of the (10.4) plane of calcite immersed in (a) water, (b) methanol, (c) ethanol, (d) propan-1-ol. The line profiles in the panels next to the (XZ) slices are taken at the position indicated by the red and blue arrows. The two line graphs are offset with respect to each other to enhance visibility. The displayed tip-sample distances were corrected for the measured static deflection (sec. 3.2).

In fig. 5.2c, AFM data obtained in ethanol are presented, and the surface position is appointed to an amplitude value of (0.05 ± 0.05) nm. In this (amplitude) region, a surface corrugation is visible, and again, corresponding line profiles are taken, one between two surface protrusions (blue arrow) and one above a surface protrusion (red arrow). Based on the surface position, two minima can be assigned in the line profiles of the amplitude signal (marked with two small arrows). The existence of a first minimum (marked with the number one) in the amplitude suggests the formation of a single solvation layer directly above the (10.4) surface. However, the line profiles of the phase signal apparently only show a very broad minimum instead of two minima. This is different from the water and methanol data, where all features are typically visible in both signals. This noticeable difference is marked with a violet box in the XZ slices of the amplitude data. From the XZ slices of both signals it is evident that no lateral, only a vertical order, described as a layer-like structure exists. Thus, in contrast to water and methanol, no site-specific order can be observed.

In the XZ slices for propan-1-ol a layer-like contrast contrast can be observed, similar to ethanol's (fig. 5.2d). The surface position is assigned to an amplitude value of (0.15 ± 0.05) nm and the minima are assigned accordingly in the line profiles. As in the case of ethanol, the second minima is not visible in the phase signal of propan-1-ol and this distinct difference is marked with a violet box in the XZ slice. For instance, the measured apparent distance between the first and second minima increases from methanol, to ethanol, to propan-1-ol. This fits with an intuitive understanding of the solvation layers as upright standing molecules, and one possible explanation is the increase in the alkyl-chains from methanol to propan-1-ol. However, as mentioned in sec. 3.2, the interpretation of the measured apparent distance in AFM measurements remains ambiguous.

Interestingly, deviation from the presented contrast are rarely observed for ethanol, but are frequently found for propan-1-ol. In these measurements, contrast inversion in amplitude and phase and/or additional minima and maxima within a similar tip-sample distance are revealed (not shown). Presumably, these additional contrasts reflect the complex interactions between the highly ordered solvation layer of the surface and the unknown solvation structure of the cantilever tip. Notwithstanding, the two main findings of this section are unaffected by these contrasts. Firstly, in all observed contrasts a layer-like structure is observed, supporting the presence of at least one solvation layer; secondly, none of theses contrasts display a lateral order in the solvation structure.

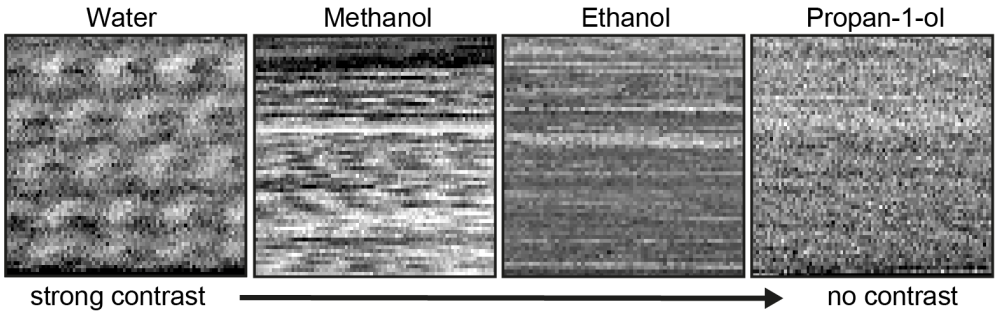

Figure 5.3.: Lateral slices (XY) of the phase signal in different solvents (a) water (b) methanol (c) ethanol (c) propan-1-ol taken at the position of the first solvation layer. These slices are $2 \times 2\,\mathrm{nm}^2$ sections, which are taken from the same 3D maps as the data presented in fig. 5.2.

According to the assignment of the surface and the solvation layers, the XY slice of the first solvation layer; i.e., the first minimum, is extracted from the different solvents (fig. 5.3). As described in chap. 4, a strong lateral order is revealed for the first hydration layer (water), commensurate to the underlying calcite crystal. The data obtained for methanol still show a lateral order, which is within the accuracy of the measurement commensurate to the underlying surface. For ethanol and propan-1-ol no lateral order is visible.

Molecular Dynamic Simulations

To understand the observed vertical and lateral order in the solvation structures in the AFM data, we collaborated with the group of [redacted] (SIN, Aalto University, Finland). The following MD simulations represent the current status of this collaboration and are kindly provided by [redacted] [213]. The molecular dynamic simulations are performed for the (10.4) surface of calcite in a similar setup as described in sec. 4.1, replacing the water with the respective alcohol. The simulations result in consecutive snapshots of the alcohol-calcite system. In fig. 5.4, the findings of the simulation are presented as line graphs showing the vertical atomic density distributions for the alcohol and the water-calcite systems. Within the density profiles of water the hydration layers can be readily identified based on the position of the oxygen atoms of the water molecule (marked by little numbers). For the alcohols, tightly bounded molecules are forming a single solvation layer. The molecules are standing upwards and the hydrophobic chain is pointing into the (alcohol) bulk while the hydroxyl group is anchored on the surface. The hydroxyl group of the ethanol forms two bonds with the surface, one towards the surface carbonate group and one to the calcium cation (a hydrogen bond).

A characteristic feature is the low density region; i.e., the roughly 2 nm wide void between the first structured alcohol layer and the bulk alcohol. The thickness of the solvation layer increases with the length of the alcohol molecule, hence the position of the void shifts away from the surface. The general results of these simulations are in accordance with previous MD studies of different alcohols, mainly with ethanol, on calcite [207, 208, 210, 211, 214].

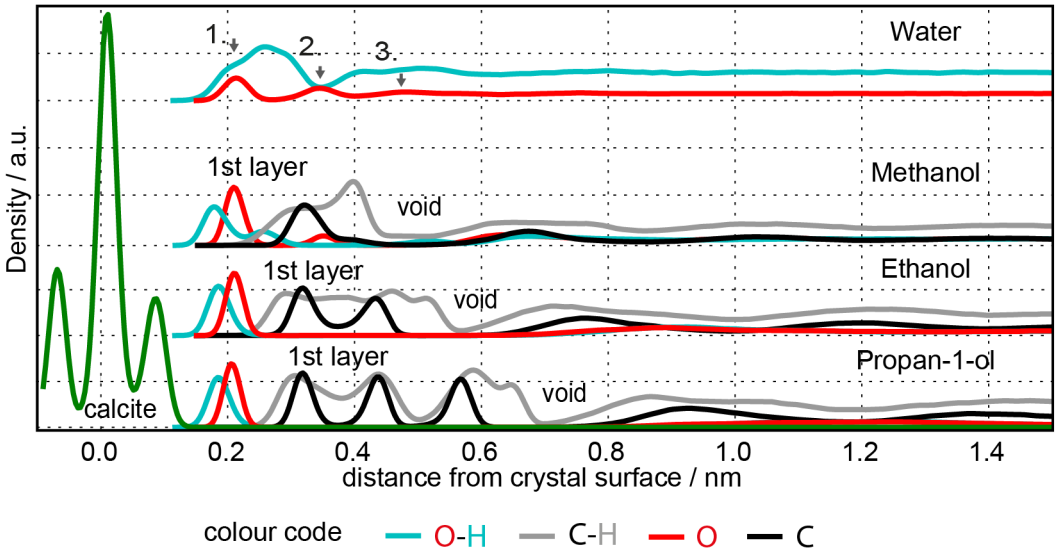

Figure 5.4.: Line graphs of the vertical density distributions of the atoms in the methanol, ethanol and propan-1-ol solution, averaged over the entire (10.4) surface of calcite. To enhance the visibility, the curves are arbitrarily offset. The atom density of the calcite crystal is scaled to fit the figure dimensions and only indicates the surface position.

Based on these density plots, the first observed minimum in the amplitude data of the alcohols is assigned to the first solvation layer. This further suggests that the observed feature for ethanol and propan-1-ol above the first solvation layer corresponds to the void region followed by the bulk. For methanol, the assignment of the void region remains difficult within the force sensitivity of the presented AFM experiments. Here, the MD simulations provide a possible explanation because in the case of methanol, the difference in the density between the void and the bulk is considerably smaller than the larger alcohols, therefore it is expected to be much harder to detect.

Since only the hydroxyl groups are bound to the calcite surface, the alkyl-chains of the (longer) alcohols still possess many degrees of freedom; i.e., the alkyl-chains might move aside when the tip (and its solvation structure) approaches. This may serve as an explanation to why no lateral contrast is observed within the first solvation layer of ethanol and propanol.

5.2 Summary and Conclusion

In this chapter, high-resolution real-space measurements of various alcohol-calcite interfaces are presented for the first time. They reveal a distinct *vertical* and *lateral* order for methanol and a *vertical* order for ethanol and propan-1-ol.

MD simulations provided density plots (of the atoms) of the studied alcohols which allows for an assignment of the observed first minima in the amplitude to the first solvation layer of the alcohols. Furthermore, the MD supports the assignment of the void and the bulk region in the experimental data.

The present study demonstrates the drastic change of the solvation structure above the calcite surface from water to solvent molecules that also contain a hydroxyl group but furthermore (an increasing) hydrophobic component.

6 3D Mapping on Calcite in the Presence of Alizarin Red S

The investigation of molecular structure formation on insulating surfaces is a growing research field in the non-contact atomic force microscopy (NC-AFM) community. Molecular structure formation is a versatile strategy, which has a huge potential to build up electrically decoupled nano-structures on insulating surfaces. Several investigations under UHV conditions have been performed to study molecular structure formation on ionic crystals such as KBr [215–223], NaCl [224, 225], CaF_2 [226] and $CaCO_3$ [201–204, 227–229]. However, there are only a few known examples of structure formation of organic molecules in liquid that are observed on the (10.4) surface of carbonates [205, 230–233]. One of the first published high-resolution FM-AFM studies investigated the molecular structure formation of Alizarin Red S (ARS) on the calcite(10.4) surface [205]. The ARS molecule was chosen because it is a known staining agent for distinguishing between calcite and other calcium-containing materials [234]. This long-known fact made ARS a promising candidate for molecular structure formation in liquid because the selective staining indicates a very specific adsorption of the ARS molecule to the calcite(10.4) surface.

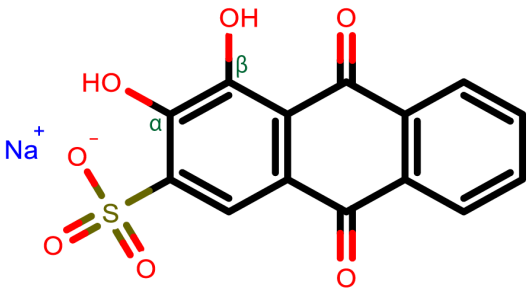

Figure 6.1.: The chemical structure of ARS; IUPAC: 3,4-Dihydroxy-9,10-dioxo 2-anthracenesulfonic acid sodium salt.

The ARS molecule (fig. 6.1) is an anthraquinone derivative and contains two acidic protons at the two hydroxyl groups (pKs_1 = 5.8 β-OH and pKs_2 = 11 α-OH) [235–238]. From the aforementioned study by Schreiber *et. al.*, it is known that the formation of ARS structures on the calcite(10.4) surface is pH-dependent [205]. Two structures, namely molecular islands with a (3 x 3) superstructure ($5 < pH < 8$) and needle-like structures with a $(3 \times n)$ superstructure oriented along the $[010]$ direction ($8 < pH < 11$), have been presented. These two structures are devoted to two different moieties of ARS with a very different binding geometry on the (10.4) surface [205]. Since mapping with the AFM has succeeded in visualising hydration layers on the calcite surface, it can be the foremost tool to investigate the molecular structure formation of ARS on calcite.

Experimental Preparation

Instrumental Set-up

The AFM experiments are performed under ambient conditions on the Cypher AFM with the very same set-up as described in chap. 3. In brief, Arrow UHV cantilevers with typical resonance frequencies of 350 kHz and quality factors Q between 4 and 7 are used. The free amplitude is calculated by using an average sensitivity of 22 $\frac{\text{nm}}{\text{V}}$. The amplitude set-pointand the z-modulation range are noted in figure captions for the presented 3D experiments.

Sample Preparation

ARS was purchased from Merck KGaA (Germany) in *pro analysis* quality and used without further purification. The pH of the solution used in the experiment was adjusted with standard solutions of 0.1 $\frac{\text{mol}}{\text{l}}$ NaOH (from Sigma-Aldrich) or HCl (from Carl-Roth GmbH). The pH-electrode (BlueLine 14 pH, Schott, Germany) of the pH-meter (CG 842, Schott, Germany) was calibrated by a two-point calibration (using standard solutions from HANNA instruments, Germany, type Hi6004 and Hi6007). The carbonate solutions used in the AFM measurements were prepared by mixing corresponding quantities of $NaHCO_3$ ($\geq$ 99.5 % from Carl-Roth) and $CaCl_2$ (*pure analysis* from Sigma-Aldrich) with Milli-Q water. In the open liquid cell of the Cypher AFM the solution continuously evaporates and the concentration of ARS molecules increases rapidly. For high-resolution imaging, concentrations of around 0.5 $\frac{\text{g}}{\text{l}}$ ARS have proven to be suitable. However, some experiments are done with even smaller concentrations of ARS. Here, the solution was prepared by diluting the 0.5 $\frac{\text{g}}{\text{l}}$ standard solution with the corresponding carbonate solution. The pH was not measured again but estimated by only taking the dilution factor into account. Calcite crystals were purchased from Korth Kristalle GmbH (Germany) and cut into cuboids with a base of $4 \times 2\,\text{nm}^2$ or $2 \times 2\,\text{nm}^2$ by Vario Kristallbearbeitung GmbH (Germany).

6.1 Results and Discussion

Standard and High-resolution Imaging

The measurement of ARS structures with AM-AFM has proven to be very challenging and only the island-like structures (see fig. 6.2 (a)) have been successfully imaged. The island-like structures are often observed as multi-layer structures, which even grow over several terraces of the calcite surface. From the line profile in fig. 6.2 (b) an apparent height of 1.3 nm for the first layer and 2.5 nm for the second layer is determined. The value for the monolayer is in perfect agreement with the value reported by Schreiber *et al.* [205]. However, the island-like structures could not be reproducibly imaged in a series of both up and down AM-AFM images and no internal (super-)structure was observed. The difficulty in imaging is most likely caused by the drifting "forest of peaks" (sec. 2.2). The piezo-acoustic excitation in the AFM introduces a constant change in the amplitude response of the cantilever that constantly changes the imaging conditions without changing the experimental parameters, e.g., the amplitude set-point. Therefore, the experimental control of the actual tip-sample interaction is rather poor, and the scanning cantilever tip is often either pushing the ARS molecules away, or does not interact with the sample system at all.

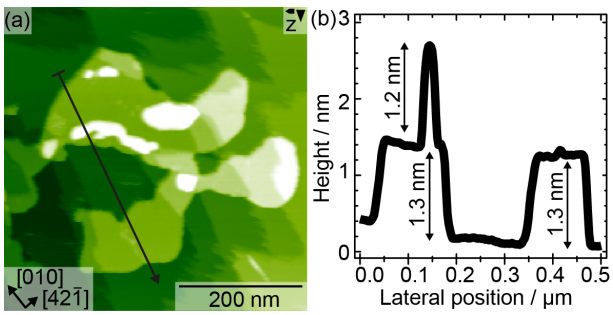

Figure 6.2.: (a) Island structures (multilayer) at a pH of 5.5 measured in an oversaturated solution of $CaCO_3$ and 0.54 $\frac{g}{l}$ ARS. The image was taken at a scan rate of 2.4 Hz and post processed by applying a simple plane subtraction. (b) Height profile (taken from (a)) showing the apparent height of the island-like structures.

In fig. 6.3 (a)-(c), three examples of AFM images with very strong atomic contrast on the (10.4) surface of calcite, which can routinely be obtained in the presence of ARS molecules are shown. In particular, fig. 6.3 (c) still displays the atomic lattice of the calcite surface with several step edges in a scan range of 100 nm. In terms of imaging this means a significant improvement in comparison with the resolution obtained by the very same AFM instrument in aqueous solutions (see chap. 4). The most striking result to emerge from these AFM images is the enhanced resolution and contrast on the calcite surface itself - almost independent of the chosen pH and ARS concentration.

The improved AFM contrast is very likely due to ARS molecules that are attached to the cantilever tip and which contribute significantly to the imaging process. This phenomenon is, for example, very well-known for CO tips under UHV conditions, and tip functionalisation is a common strategy to investigate certain tip-sample interaction forces [239].

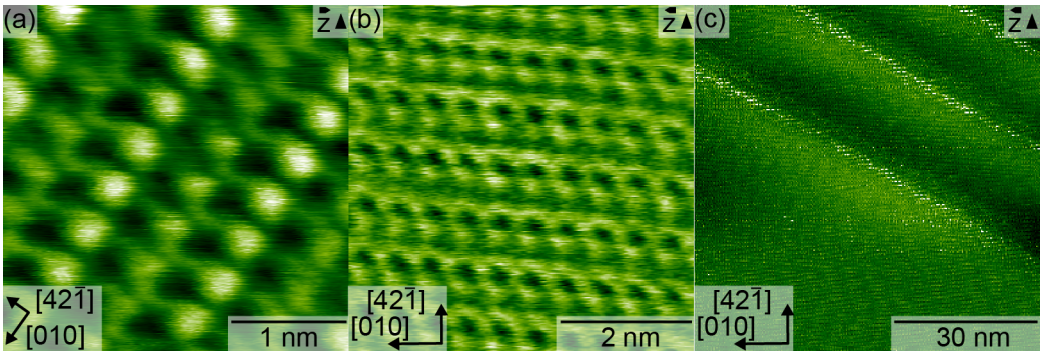

Figure 6.3.: High-resolution AFM images of the calcite surface in a solution of ARS and highly oversaturated calcium carbonate not corrected for thermal drift. The imaging conditions are in (a) pH = 6.91, 0.5 $\frac{g}{l}$ ARS and a saturated solution of $CaCO_3$, in (b) pH = not determined, 0.1 $\frac{g}{l}$ ARS, oversaturated solution of $CaCO_3$, in (c) pH = 9.13, 1 $\frac{g}{l}$ ARS, oversaturated solution of $CaCO_3$. The AFM images are post processed by applying a simple plane subtraction. Image (a) is further treated by a line-by-line subtraction to correct for imaging artefacts.

3D Mapping Experiments

The influence of the ARS onto the hydration layer structures above calcite was studied by 3D AM-AFM mapping experiments. Unfortunately, it was not possible to perform a 3D map directly above the island-like structures induced by the ARS molecules without destroying it. Therefore, the focus for the mapping experiments is set on the bare calcite (10.4) surface and the enhanced contrast formation. In fig. 6.4 one obtained 3D AM-AFM map (at pH = 6.11) is presented, showing that the oscillation amplitude (a) and phase (b) decrease monotonously when approaching the surface and reveal no oscillatory features (fig. 6.4 (c)). The average of the oscillation amplitude and phase in fig. 6.4 (c) illustrate that within this experiment the cantilever tip is barely entering the transient regime (sec. 3.2). The position of the calcite surface is assigned according to the criterion defined in fig. 2.8 at position A. The 2D layer (fig. 6.4 (d)) is extracted close to the turning point at the position A and displays only slight distortions. The observed unit cell fits quite nicely to the unit cell expected for the bare calcite surface.

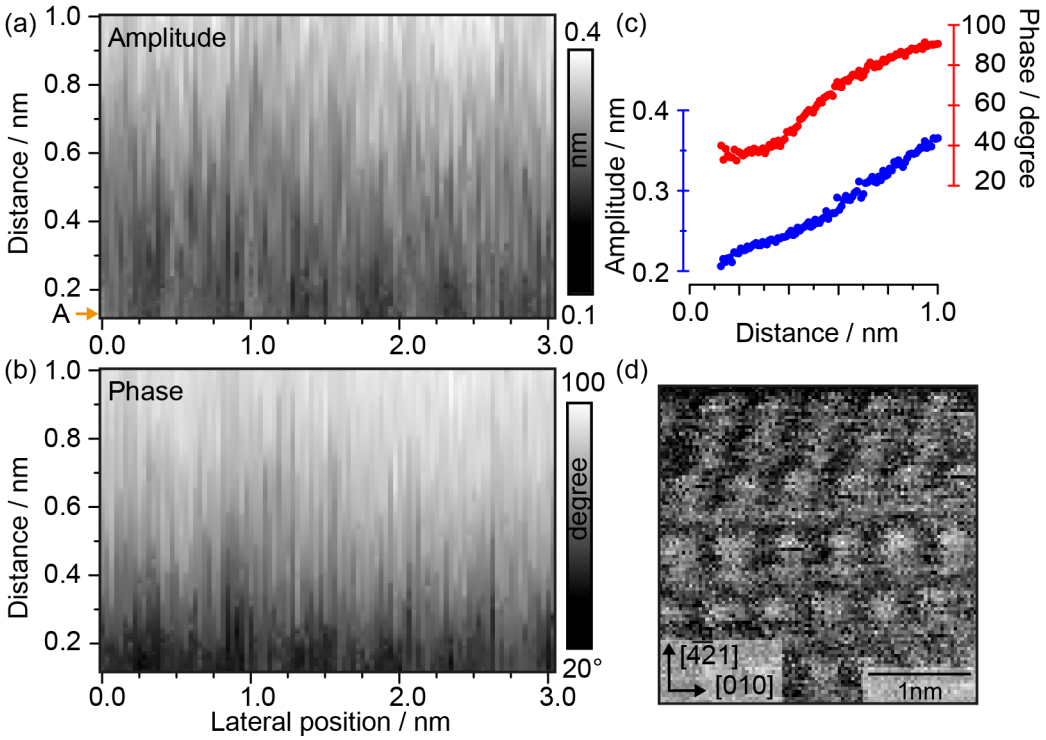

Figure 6.4.: Oscillation amplitude (a) and phase (b) of a vertical 2D slice along the [010] direction of the (10.4) surface of calcite captured in the presence of ARS. (c) The average for the oscillation amplitude and the phase over the entire slice. The red and blue line graphs are offset with respect to each other to enhance visibility (d) A horizontal 2D slice in the transient regime. The measurement was performed in a 0.5 $\frac{g}{l}$ solution of ARS in oversaturated $CaCO_3$ solution at a pH of 6.11. The 3D map was acquired with a free amplitude of 0.45 nm, a set-point of 0.7 and a modulation range of ±0.5 nm at a temperature of 300 K. The displayed tip-sample distances were corrected for the measured static deflection (sec. 3.2).

A limitation of the presented experimental mapping data is the small sample number, so the statistical significance is not sufficient in order to make a conclusive statement. However, the experiments performed on calcite in an aqueous solution have been done with very similar experimental parameters and settings and clearly show hydration layers on carbonate surfaces (chap. 3 and 4). Therefore, it is somewhat surprising that no oscillatory features could be observed in the presence of ARS. From the presented experiments it is not possible to deduce whether the tip-sample interaction at the water-mineral interface changes due to (one or more) adsorbed ARS molecule on the cantilever tip, or the structure of the hydration layer changes itself due to the presence of ARS molecules at the calcite surface. The observation of both the outstanding atomic resolution and the apparent disappearance of the hydration layers suggests that they share the same underlying mechanism. Further experimental investigations are needed to clarify the role of the ARS molecules in AFM imaging and their effect on the hydration layers. This observation emphasizes the difficulties when investigating structure formation directly in a liquid environment.

6.2 Summary and Conclusion

The findings of this work confirm reported formation of island-like like structures of ARS in a pH range of ($5 < \mathrm{pH} < 8$) on the (10.4) surface of calcite. The obtained apparent heights for the monolayer islands is in good agreement with recently reported value. Interestingly, in the presence of ARS the imaging contrast on the bare calcite surface is significantly enhanced compared to the results on calcite. However, no oscillatory hydration layer forces could be successfully detected with the experimental settings used on the carbonates in aqueous solutions. Despite the exploratory nature of this study, one can speculate about a connection between the image quality in standard AFM investigations and the structural order of the solvation molecules. Such a connection would be highly relevant for further AFM investigations; thus, it is suggested that the possible connection of these factors is investigated in future studies.

7 2D Mapping on the Pristine X-Cut of Lithium Niobate

Lithium niobate (LN) ($LiNbO_3$) is a man-made, ferroelectric transparent oxide displaying numerous properties such as birefringence, piezoelectricity, pyroelectricity, photovoltaics, photoelectricity and photoreactivity [240, 241]. Consequently, LN is used in various fields of industrial applications, such as non-linear optics [242–244], thin-films [245], second-harmonic generators [246, 247], non-volatile memory [240] and surface acoustic wave (SAW) devices [248].

Single crystals of LN are mainly produced via the Czochralski-method [249], which is most famous for the production of high-purity silicon. The composition of a growing LN crystal depends significantly on the starting composition of the melt [241, 250]. However, like many other oxides, stoichiometric lithium niobate (SLN), melts incongruently. Therefore, single crystals are mostly produced from the congruent melt, which consists of 48.45 mol LiO_2 and 51.55 mol Nb_2O_5 [251, 252]. The relative excess of Nb^{5+} and the deficit of Li^+ ions in the melt promotes lithium vacancies; consequently, congruent LN has a high tendency for intrinsic defects [253, 254]. Fortunately for many applications, the lattice symmetry of congruent LN is not affected by these intrinsic defects [241]. SLN can be produced by the double crucible Czochralski-method [255] or the vapour transport equilibration technique [256].

LN crystallises in a trigonal crystal structure (space group R3c) [240, 257]. In SLN, the oxygen atoms form a distorted hexagonal close structure with Li^+ and Nb^{5+} occupying the same number of octahedral sites. The structure of LN is dominated by the fact that Li^+ and Nb^{5+} have a very similar ionic radius and are arranged in a similar chemical environment, but differ significantly in the amount of their charge and binding strength to oxygen [258]. Therefore, the combination of Li^+ and Nb^{5+} leads to strong elastic forces in the LN crystal [259] and changes the stacking distance of the alternating Li^+ and Nb^{5+} cations along the *c*-axis to 0.30 nm and 0.39 nm, respectively (see fig. 7.1 (a)). This intrinsic displacement of the cations is the reason for the spontaneous polarisation of LN. The polarity of LN can be reversibly switched by an external electric field which may lead to very interesting applications [260], e.g., chemical sensors [261].

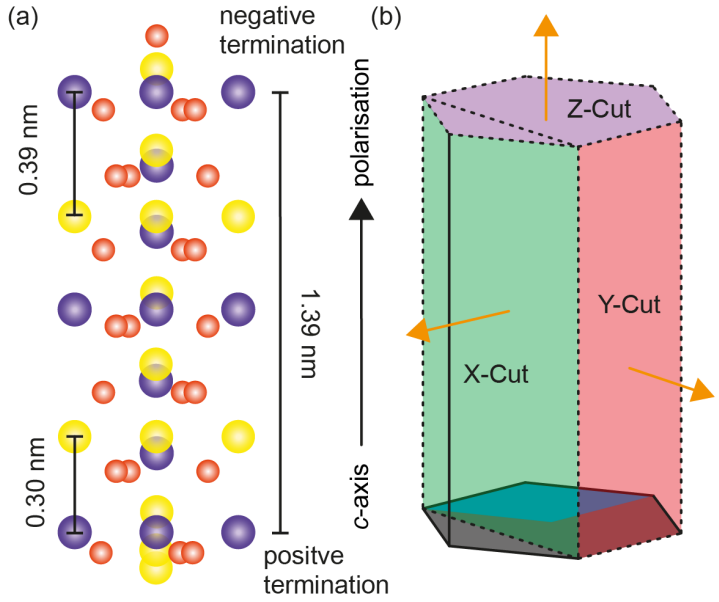

Figure 7.1.:
(a) Schematic representation of LN along the *c*-axis indicating the bulk structure (uncharged) and the positive and negative surface terminations (charged). (b) The planes of the most typical wafers X-, Y- or Z-Cut are indicated within the hexagonal unit cell of LN by their normal vectors [262].

Commercially available LN is often prepared as polished X-, Y- or Z-Cut wafers, using a Cartesian coordinate system to describe the surface direction. Here, the z-axis coincides with the c-axis of the rhombohedral description, the x-axis is chosen to be parallel to one of the basis vectors (a_1, a_2, a_3), and the remaining y-axis is oriented orthogonally and right-handed to the x-axis (see fig. 7.1 (b)). Among the industrial relevant surfaces of LN, the Z-Cut is the most studied one, because the surface plane is oriented perpendicular to the direction of the spontaneous polarisation [263–267]. The two possible polarisations along the c-axis are typically marked on industrial used LN wafers with a plus or a minus sign [261, 268, 269]. Both sides of the Z-Cut are polar and the strong surface charge of the Z-Cut severely hinders AFM measurements in an UHV environment. However, in a liquid environment impurities, such as dust particles, ions, organic, and even solvent molecules, can shield this surface charge, and high-resolution FM-AFM images of the Z-Cut in aqueous solution have been presented [17].

The X-Cut is also used in industrial applications and, in this context is the only relevant surface of LN, which is neither polar nor piezoelectric. The surface plane of the X-Cut is oriented perpendicular to a mirror plane; thus, any charge is mirrored with respect to this plane and the plus and minus X-Cut are completely equivalent. The X-Cut is used for optical wave [270] and SAW guides, [271] and compared to the Z-Cut, is still relatively unexplored. Only recently high-resolution FM-AFM images of the X-Cut in pure water have been presented in combination with density function theory (DFT) calculations, revealing a rectangular unit cell with a non-stoichiometric and lithium-enriched termination [272]. For this investigation, the focus is set on the X-Cut . Here, the first investigation of the hydration structures above the X-Cut of LN with an AFM mapping technique is reported.

Experimental Preparation

Instrumental Set-up

The measurements of the LN samples were performed in the group of [redacted] at Kyoto University under the supervision of [redacted]. Their optimised FM-AFM consists of (a) self-built electronics and (b) a modified AFM from the Shimdazu Corporation (fig. 7.2). The AFM features a low-noise cantilever beam deflection sensor with a deflection noise density in the range of 13 to 30 fm/$\sqrt{\text{Hz}}$ [35]. It is equipped with an optimized analogue FM detector [273] and photothermal excitation [274]. The scan software was written using LabVIEW™ from National Instruments, and the incorporated mapping function is based on the "curve-by-curve" approach. The imaging mode can be easily switched from standard scanning to 2D mapping. Here, the AFM acquires one force-distance curve (FDC) and then moves to the next position before starting the next FDC. While the cantilever is ramped towards the surface, the frequency shift of the cantilever is precisely measured. If a predefined frequency shift set-point is reached, the FDC is stopped in order to protect the cantilever tip from crashing into the surface [48].

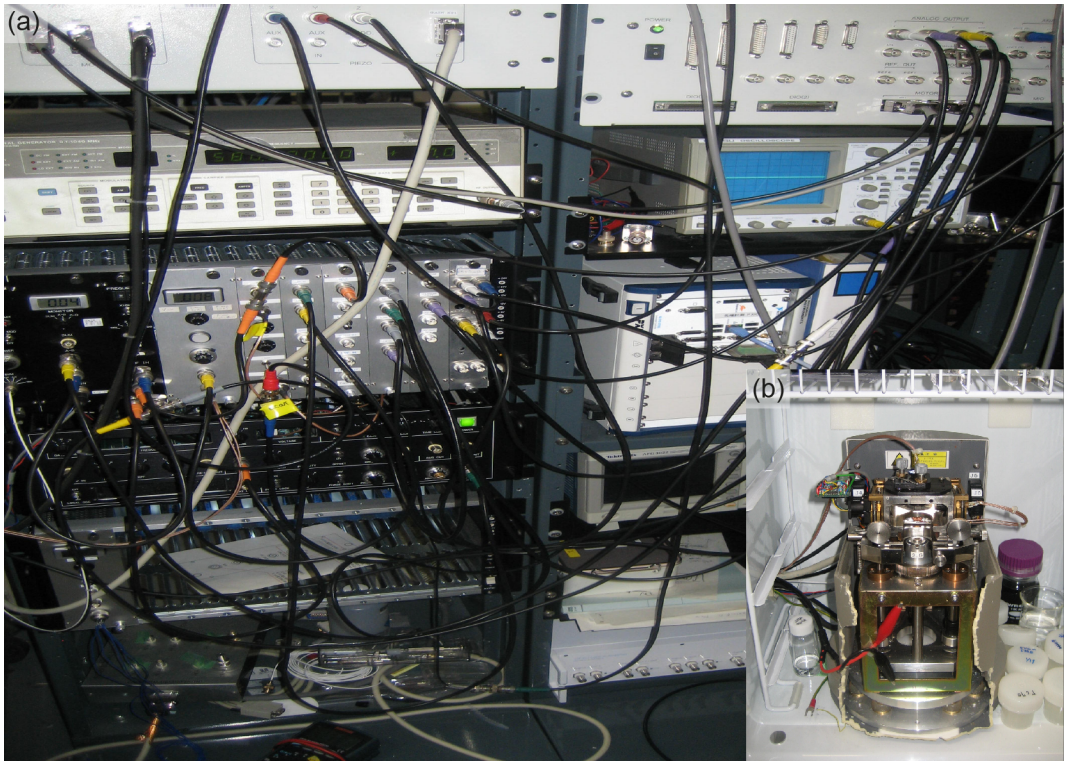

Figure 7.2.: Photograph of (a) the self-builtelectronics and (b) the modified AFM from the Shimdazu Corporation. The pictures were taken with the kind permission of [redacted].

The experiments were performed using PP-NCH Nanosensor™ cantilevers from NanoWorld AG (Switzerland). The first resonance frequency is typically in the range of 100 to 130 kHz, and the quality factor Q between 5 and 10. The thermal noise method was used to characterise the cantilever before every measurement. Based on an estimation of 40 $\frac{\mathrm{N}}{\mathrm{m}}$ for the spring constant, the oscillation amplitudes were determined to be in the range of tens of pm up to a few nm.

Sample Preparation

The single crystal LN X-Cut wafers used in this thesis are commercially available wafers, purchased from the distributor EQ Photonics GmbH (Germany), and made by Gooch and Housego Palo Alto, formerly Crystal Technology (United States). The company cut the wafers (about 0.5 nm thick) from a large boule perpendicular to the x-axis with a precision of 0.5°, polished both sides with colloidal silica particles (trade name Syton (DuPont)) to optical grade, and rinsed them in water and a 5 % w HF solution for a few minutes to remove the silica particles. To insert the samples into the AFM, it is necessary to cut the large wafers with a diamond cutter into smaller pieces to a size of about $1 \times 1\,\mathrm{cm}^2$. The AFM measurements were taken in an aqueous solution of 1 $\frac{\mathrm{mol}}{\mathrm{l}}$ KCl (made from *pure analysis* KCl from Sigma-Aldrich and deionised water).

Although the wafers were polished, it is known that commercial wafers are still very rough and dirty on the nano scale and need further cleaning for high-resolution imaging with the AFM [3]. In the first step, the small sample pieces were washed in a clean room environment for 15 to 30 minutes in an ultrasonic bath, once in acetone and once in ethanol. In step two, the samples were heated in muffle furnace KDF S-70 (Denken Co. Ltd., Japan) for 5 hours at 1000 °C in order to further smooth the surface [264, 265, 275]. After the heating process, the samples cooled down over night. On a µm scale, the annealing at this temperature results in a wide variety of terrace-and-step structure. The terraces are due to the imperfect cutting of the crystal boule with respect to the surface normal of the desired X-Cut wafer [3].

7.1 Results and Discussion

High-resolution AFM Imaging

Ideally, mapping experiments are performed on the basis of high-resolution AFM images. A high-resolution, drift-corrected FM-AFM image of the X-Cut is shown fig. 7.3. The post-correction for thermal drift was done using a unit cell obtained by averaging FFT data from a series of up and down images. Fig. 7.3 (a) reveals a very pronounced "row-pairing " reconstruction where every second row is imaged brighter or darker, respectively. This feature of the surface is occasionally observed on the X-Cut and is directly evident from the FFT analysis shown in Fig. 7.3 (b) [263]. Interestingly, this reconstruction is also observed with the AFM for the calcite surface [16, 142].

The acquired real-space information reveals a rectangular unit cell with lattice constants of a = (0.75 ± 0.04) nm and b = (0.45 ± 0.02) nm with an angle of $\alpha = (92 \pm 2)°$. In contrast, the aforementioned study by Sanna *et al.* [263] reports a rectangular surface unit cell with lattice dimensions of 0.75 × 0.55 nm forming an angle of α = 94.8°. Both unit cells cannot be explained by a bulk truncated model. The most surprising aspect of the finding is that only one side is significantly shorter than expected from the reported results. The surface unit cell was reproducibly obtained on different samples that were not aligned within a particular direction in the AFM. Thus, there is no indication for a wrong calibration of one of the scanning piezos.

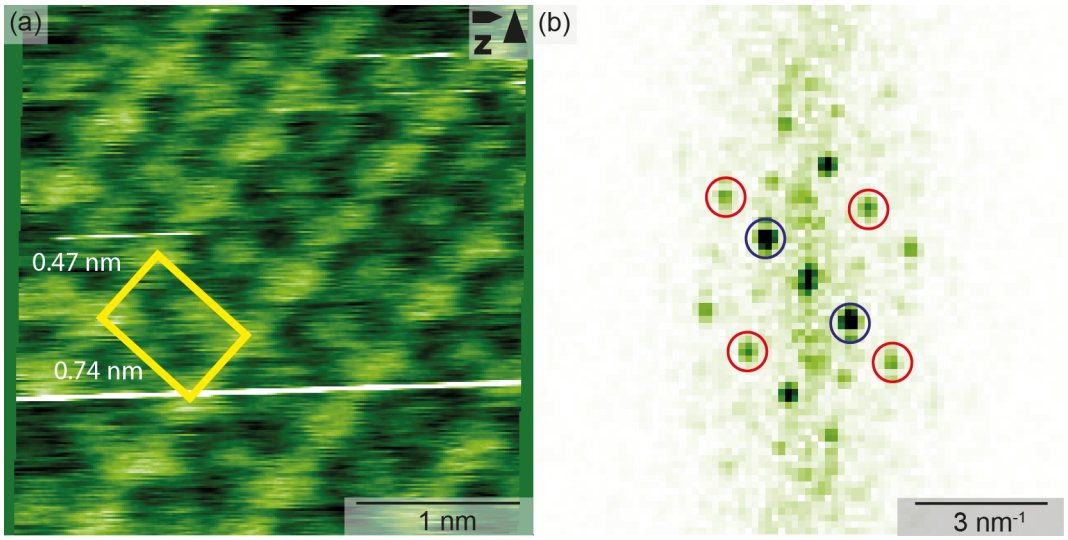

Figure 7.3.: (a) A high-resolution FM-AFM image of the X-Cut taken in an aqueous solution of 1 $\frac{\text{mol}}{\text{l}}$ KCl and corrected for drift and tilt by a plane level subtraction. The surface unit cell is indicated by a yellow box. (b) The two-dimensional FFT analysis featuring the corresponding unit cell and the "row-paring" of the X-Cut surface.

It is difficult to explain this unexpected result, but it could be due to an unknown surface termination or reconstruction of Li, Nb or O ions. The sample preparation and cleaning procedure in this work was very similar to the earlier study, with the only exception that in this study, the sample was measured in an aqueous solution of 1 $\frac{\text{mol}}{\text{l}}$ KCl instead of pure water [272]. Although ions are known to enhance the contrast on an atomic scale for an AFM image [276], so far an induced change of the surface termination by K^+ and Cl^- ions (possibly by adsorption) is neither known nor suggested for the LN X-Cut within the literature. The cutting process by the manufacturer is a very direction-sensitive process and even a slight misalignment on this macroscopic scale might explain large deviations on a smaller scale. Still, in the first place, a larger inclination error should affect the sample by decreasing the size of the observed not the surface termination. However, this question addresses further calculations and simulations, which are beyond the scope of this thesis.

2D Mapping Experiments

In order to determine the structure of the hydration layers,2D force mapping in FM-AFM mode was performed. The experimental results are summarised in fig. 7.4. The distance scale corresponds to the z-piezo modulation, which is arbitrarily set to zero at the point of closest approach. In this AFM setup the closest distance between tip and surface is only determined by the frequency shift set-point. A small value of the frequency shift set-point corresponds to a larger tip-sample distance compared to a larger frequency shift set-point (within one experiment). The frequency shift set-point cannot be set to arbitrarily large values in FM-AFM experiments, because at a certain limit, the cantilever oscillation becomes unstable [151]. An assignment of the surface position based on the frequency shift data remains ambiguous in this experiment and no reliable surface criterion has been derived.

In fig. 7.4 (b) and (e) a clear modulation of the frequency shift above the surface can be identified. For both images, the collected approach data (not shown) do not differ notably from the retracted data shown. The features within the images are tilted, which is either due to the thermal drift of the sample relative to the cantilever tip or a tilt of the sample within the AFM. The average profiles of the frequency shift in fig. 7.4 (a) and (d) clearly show two minima in the frequency shift data (A and B). In fig. 7.4 (b) this modulation forms a distinct, periodic and very pronounced pattern, while in fig. 7.4 (e), the second minimum B is not imaged with the same intensity and resolution, forming a layer rather than alternating patches. Furthermore, the minimum A directly above the surface is differently shaped in both images. Both observations can be assigned to different tip conditions; i.e., the interaction

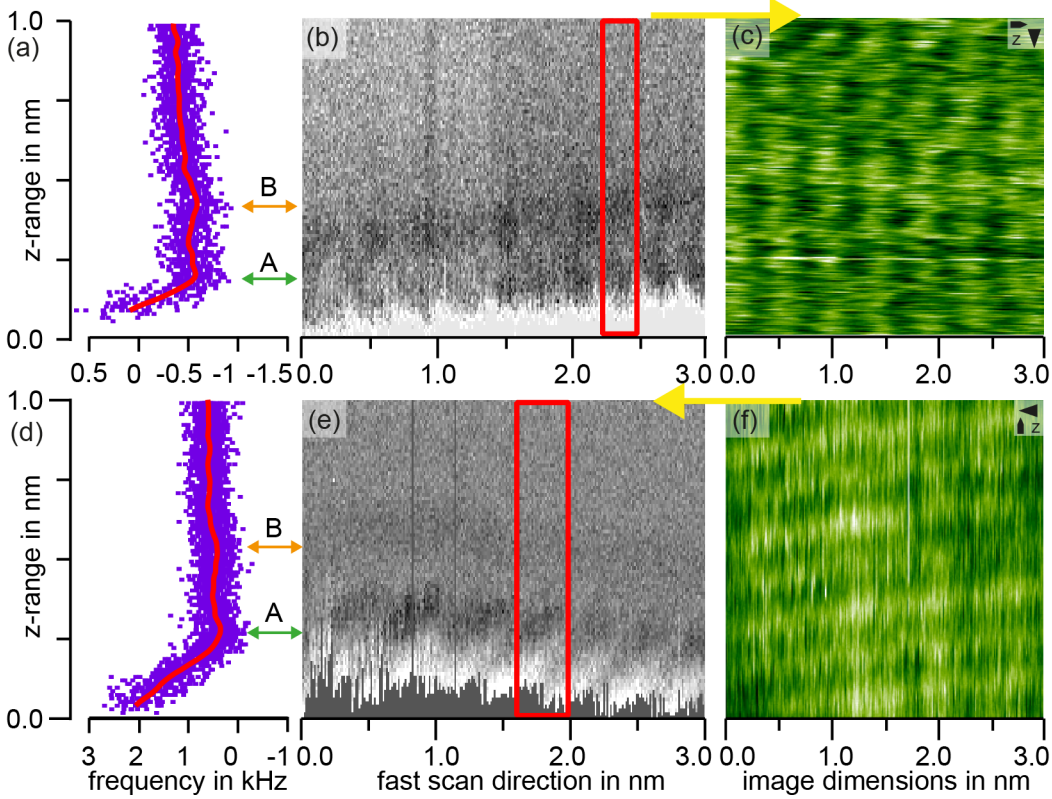

Figure 7.4.: The 2D frequency shift slices (b) and (e) of the X-Cut surface are imaged with a scan speed of 9.7 Hz on different samples with different cantilevers with an amplitude, a sensitivity and a frequency shift set-point of (b) 0.29 nm, 105 $\frac{\text{nm}}{\text{V}}$ and 510 Hz and (e) 0.02 nm, 21 $\frac{\text{nm}}{\text{V}}$ and 2400 Hz. (a) and (d) are 1D averages over the area indicated by the red lines. (c) is an AFM image shortly captured before slice (b) and (f) an AFM is image shortly captured after slice (e). The modulations devoted to the hydration forces are marked with arrows A and B. The yellow arrow is indicating the slow imaging direction of the 2D slices relative to the standard AFM images. The AFM images are corrected by a plane and a line-by-line subtraction.

with the hydration layers within the experiment. Although, the direct relationship between the recorded frequency shift data and the water density distribution above LN cannot be determined from experiments alone, it is fair to assign the features themselves to the presence of hydration layers. When inspecting fig. 7.4 (a) and (d) in detail, a significantly different range of the frequency shift and noise level can be identified. This is due to the great difference in the chosen oscillation amplitude. In the presented data, the apparent distance between the two observed minimum in the frequency shifts is (0.25 ± 0.04) nm. The AFM images captured shortly before or after the 2D slices (fig. 7.4 (c) and (f)) illustrate that the relative orientation of the recorded frequency shift maps (aligned along prominent crystal directions) are aligned along prominent crystal directions.

7.2 Summary and Conclusion

The surface of X-Cut was reproducibly imaged with high-resolution FM-AFM in a liquid environment. A rectangular unit cell was imaged, however, the obtained lattice parameter does not match the reported values within the literature. This unanticipated finding suggest that a so far unknown surface termination develops under the preparation conditions.

The most important finding originates from the 2D mapping experiments that reveal a commensurate structure of the water above the X-Cut surface. Up to two minima in the frequency shift data can be clearly distinguished and are assigned to two hydration layers. However, in this study the precise determination of the surface position is not addressed and the existence of more hydration layers is not preluded.

Further research should be conducted to investigate the solid-liquid interface of LN, because its ferroelectric properties may provide a unique way to tune the formation of hydration layers on a pristine insulation surface and; thus, providing fundamental insights into the general formation process of hydration structures.

Conclusion and Outlook

8

The presented work takes advantage of the recent progress in the development of high-resolution *in-situ* AFM to investigate the solid-liquid interface. I report on the successful implementation of a state-of-the art 3D mapping routine that combines the easy-to-use AM-AFM technique with reliable high-speed data acquisition for solvation layer mapping. The issue of free amplitude variations due to the drifting "forest of peaks" is addressed and solved by periodically adjusting the excitation amplitude during the data acquisition. Furthermore, a reliable criterion for the surface position is derived based on the static deflection and the amplitude signal, allowing for an unambiguous assignment of the observed solvation structures.

The described implementation of this technique is not limited to the used AFM instrument, but is generally applicable for any AFM instrument. Such an easy-to-use 3D mapping routine, without using advanced but pricey techniques like photothermal excitation or FM-AFM, is expected to meet the needs of researchers in various fields. The use of AM-AFM allows the routine to work beyond the harmonic approximation and is, therefore, capable of investigating even very strongly bound hydration layers. However, the theoretical explanation of the obtained AM-AFM data can be far more challenging compared to data acquired with FM-AFM.

This thesis addressed the demanding task of obtaining reliable image quality in 3D mapping and the potential of the routine is successfully benchmarked by imaging the hydration layers on the calcite(10.4) surface in aqueous solution. The results indicate that the presence of hydration layers significantly contribute to the contrast observed in high-resolution dAFM measurements in a liquid environment. The 3D mapping routine has been further tested in an investigation of the complex interactions of Alizarin Red S molecules with the calcite surface in water. The study demonstrated an enhanced atomic contrast on the calcite(10.4) surface in the presence of ARS.

The main purpose of this study is to investigate the arrangement of different solvent molecules at pristine surfaces, such as man-made lithium niobate (LN) and the natural carbonates, calcite, dolomite and magnesite. The study of LN in the group of [redacted] at Kyoto University demonstrated atomic resolution on the X-Cut surface and 2D mapping experiments revealed a commensurate structure of the water above the X-Cut in registry to the surface protrusion. Up to two minima in the frequency shift data can be clearly distinguished and are assigned to two hydration layers.

High-resolution 3D AM-AFM maps of the interfaces of three natural carbonates, namely calcite, dolomite and magnesite have been obtained. Despite their different lattice constants, the experimental AM-AFM data display a "checker-board" pattern with three hydration layers and a commensurate lateral pattern, templated by the underlying surface. This study clearly demonstrates the importance of the surface lattice dimensions for the formation of the hydration layer. The 3D mapping results were compared to theoretical studies using MD simulations, which confirm a vertically and laterally ordered water structure above these three carbonate surfaces. Beyond the experimental results, the simulations revealed that due to the different lattice spacings, intra-layer hydrogen bonds between the water molecules are only possible for magnesite and largely prohibited for calcite and dolomite. This again demonstrates that the lattice dimensions are a crucial parameter for the formation of the hydrogen network within the hydration layers.

This investigation is complemented by a systematic high-resolution 3D study on the formation of solvation layers above the calcite surface immersed in three different alcohols, namely, methanol, ethanol and propanol. These alcohols are the most simple approach to studying the interaction of the surface with molecules possessing a hydroxyl group. Interestingly, the experimental data reveal for methanol only one solvation layer but also vertical and lateral order. In sharp contrast, for ethanol and propan-1-ol a layer-like structure, with only vertical order, is found. The experimental data suggest the existence of one strongly bound solvation layer followed by a region of low molecular density (the void) for ethanol and propan-1-ol. These findings are supported by supplementary MD calculations.

The high-resolution capabilities of 3D AM-AFM mapping is demonstrated and high quality 3D AM-AFM maps are obtained on different relevant surfaces. The obtained experimental AFM data in this thesis reflect the intrinsic solvation structure, that is a fundamental prerequisite for understanding and tailoring surface reactivity at the solid-liquid interface. The AFM mapping technique has proven to be irreplaceable for studying the solid-liquid interface with atomic-scale site-specificity and is ideally suited to investigate the knowledge gaps in this field of research. For instance, the impact of ions on the structure and formation of hydration layers is considered an essential further step when aiming for an accurate description of interfacial processes.

3D Data Acquisition and Processing

A

The data acquisition and evaluation in this thesis was performed by the extensive use of the Igor Pro software (WaveMetrics, USA). This technical appendix is meant to explain the code structure and major challenges during the development. This includes the 3D mapping routine, and for the analysis part, the distance correction for the static deflection. Together with the detailed manual of the Igor Pro software, this appendix aims to provide further insights for those interested in studying the solid-liquid interface with 3D AFM mapping.

Structure of the 3D Mapping Code

The code of the 3D mapping routine consists mainly of four distinct blocks, a simplified pseudo code version is shown in fig. A.1. The experimentalist starts the 3D routine by loading the procedure file and running the Initialisation() function. This sets up most of the needed parameters and settings within the Asylum Research software. The Pre-acquisition() function is called every time before the 3D measurements starts, in order to respond to the user inputs and synchronise the settings between the Asylum Research software and the 3D routine. All experimental parameters are stored within the DataVolumeParm wave that is automatically created and updated by the Pre-acquisition() function. The original Cypher AFM software provides several user interfaces to directly interact with the Cypher AFM. The 3D mapping code relies on the UserOutAndTrigger() function that is called every time an AFM image is started by the experimentalist. To switch among the different imaging modes the corresponding start variable in the DataVolumeParm wave has to be set manually to one (3D mode) or zero (2D standard imaging). Between the standard scanning and the 3D mapping, the cantilever tip remains close to the surface to prevent the z-piezo from building up creep. After the data acquisition, the 3D routine converts the time-dependent raw signal into a spatial-dependent 3D map. Every captured channel is saved in a separate data volume that contains the unfiltered data collected during the entire experiment, including the free amplitude adjustment. The conversion process keeps the spatial information relative to the sample surface; e.g., for a scan down 3D map the corresponding axis is reversed.

Initialisation()

- writes 3D settings into the scan software
- checks if all requirements are met
- disables interfering software functions
- creates all needed variables and waves
- sets all default values
- wires the crosspoint of the AFM
- sets up a table with all important parameters

PreAcquisition()

- clears old data and kills all graphs
- checks the most important initialisation steps
- applies and updates the mapping parameters
- creates the modulation wave
- saves imaging parameters
- checks and sets the acquired channels

UserOutAndTrigger()

- fixes amplitude and phase to the predefined values
- ramps the cantilever to the starting position
- sets the callbacks up; e.g., stops the data acquisitions at the right time
- calls the graph for the raw data
- provides a diagnostic mode for error analysis
- performs the mapping; e.g., sends the modulation to the z-piezo and sets the feedback loop for the free amplitude

ScanEnd()

- clean up after the measurement; e.g., resets the imaging parameters
- transforms the acquired data to three dimensional waves
- calls graphs to present the data

Figure A.1.: Concept of the 3D routine implemented on Cypher AFM. The 3D mapping routine is structured in four main parts: 1. The Initialisation() function (only executed once while the routine is loaded). 2. The PreAcquisition() function (executed shortly before every measurement). 3. The User Interface UserOutAndTrigger() that actually performs the measurement and 4. The clean up and data presentation functions summarised in ScanEnd().

Correction of the Tip-Sample Distance

In the presented high-resolution AFM set-up the static deflection not only displays a distinct corrugation within the transient regime, but also reaches (for a typically used set-point of 0.7) values in the range of up to 30 % of the applied z-piezo modulation. Therefore, the correction of the tip-sample distance for the measured static deflection is of major importance for determining the relative position of the measured solvation structures.

In this thesis, the captured 3D data are presented as XZ slices along prominent crystal directions, or as XY slices at or above the surface position. If the static deflection only displays slight site-specific variations and very little noise, the simplest approach to correcting the data (all signals) is based on averaging the static deflection data. The average, which can be obtained for the presented slice only, or for the entire 3D volume, transforms the information in a 1D offset. This offset can be directly added to the applied piezo modulation. Here, one Igor Pro Feature comes in handy, which allows to directly plot 2D data versus non-linear axis. This keeps the programming effort to a minimum. However, this approach is limited to low-drift data with no or only a little noise.

In 3D maps with large noise and tip changes, which typically occur along the slow scan direction, the relative position between different features in amplitude and phase may significantly depend on the static deflection. Here, a point by point correction provides a far better, however, computational more demanding solution. This approach has been used for the data presented in chap. 4 and 5. The procedure is split into two parts as shown in fig. A.2. In the first step, the Igor functions ImageFromXYZ() is used to position the acquired data on their new vertical position by placing them on a grid that is chosen to have three times the number of the original data. Based on these new slices, profiles at interesting surface positions are extracted (see fig. A.2 (c)). These line profiles still only contain collected data; however, these XZ slices are hard to analyse and linear interpolation (Igor Function: Interpolate2()) is used to enhance the visibility of the hydration layers (see fig. A.2 (d)). These interpolated data also provide the ability to average the data over certain areas of interest (see fig. A.2 (e)). Such an average is not easily accessible to the corrected data without interpolation because here the data points in different profiles are typically not equally spaced. Interpolation is a typical source of artefacts and errors in the data evaluation. However, great care has to be take by the interpretation of these data averages. Thus, the averaged line profiles presented in chap. 6 have been carefully checked by comparing them with arbitrarily picked single line profiles.

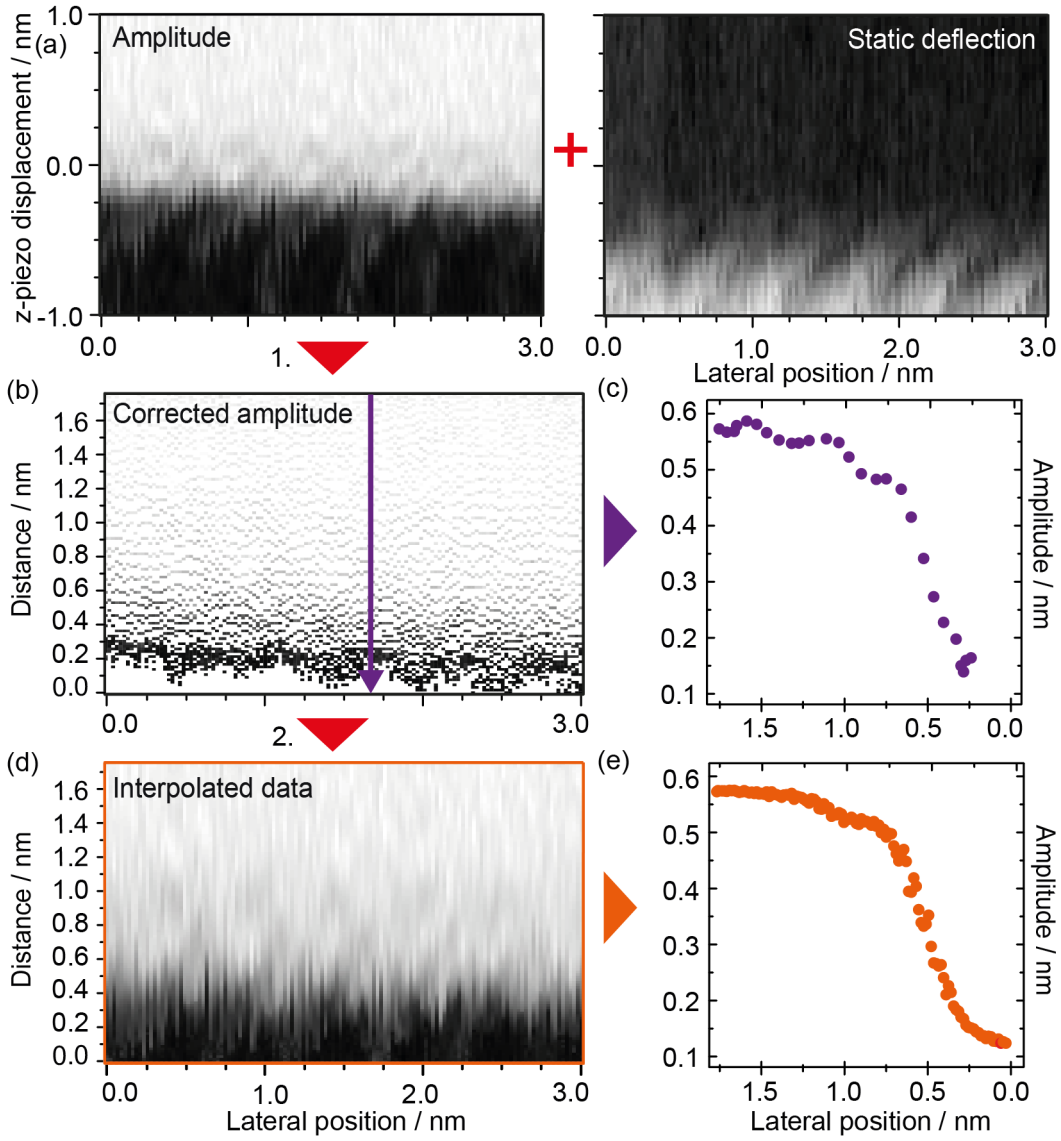

Figure A.2.: (a) A XZ slice of amplitude (colour scale from 0.1 to 0.2 nm) and static deflection channel (colour scale from 0 to 0.6 nm) taken from a 3D map capturing the hydration layers above the (10.4) surface of calcite. The measurement was performed with a modulation range of ±1.0 nm. (b) The amplitude data corrected for the static deflection data. (c) A single line profile of the amplitude taken at the position of the purple line in b. (d) The interpolated amplitude data. (e) An averaged line profile taken for the hole amplitude slice.

Bibliography

[1] T. Fukuma, K. Kobayashi, *et al.*, *Appl. Phys. Lett.* **2005**, *87*, 34101.

[2] T. Fukuma, S. P. Jarvis, *Rev. Sci. Instrum.* **2006**, *77*, 43701.

[3] S. Rode, PhD thesis, Optimization of an Atomic Force Microscope and its Application for Highest-Resolution Imaging in Liquid Environments, Johannes Gutenberg-Universität Mainz, **2011**.

[4] C. Marutschke, D. Walters, *et al.*, *Nanotechnology* **2014**, *25*, 335703.

[5] F. C. Meldrum, R. P. Sear, *Science* **2008**, *322*, 1802.

[6] G. E. Brown, G. Calas, *Geochemical Perspectives* **2012**, *1*, 483.

[7] K. Henriksen, Young, *et al.*, *Palaeontology* **2004**, *47*, 725.

[8] M. Ricci, J. J. Segura, *et al.*, *Langmuir* **2015**, *31*, 7563.

[9] G. Binnig, H. Rohrer, *et al.*, *Phys. Rev. Lett.* **1982**, *49*, 57.

[10] G. Binnig, C. Quate, *et al.*, *Phys. Rev. Lett.* **1986**, *56*, 930.

[11] H.-J. Butt, B. Cappella, *et al.*, *Surf. Sci. Rep.* **2005**, *59*, 1.

[12] F. J. Giessibl, *Science* **1995**, *267*, 68.

[13] Y. Sugawara, M. Ohta, *et al.*, *Science* **1995**, *270*, 1646.

[14] M. Bammerlin, R. Lüthi, *et al.*, *Appl. Phys. A* **1998**, *66*, S293.

[15] T. Fukuma, K. Kobayashi, *et al.*, *Appl. Phys. Lett.* **2005**, *86*, 193108.

[16] S. Rode, N. Oyabu, *et al.*, *Langmuir* **2009**, *25*, 2850.

[17] S. Rode, R. Hölscher, *et al.*, *Phys. Rev. B* **2012**, *86*, 75468.

[18] L. Gross, *Nat. Chem.* **2011**, *3*, 273.

[19] F. Mohn, L. Gross, *et al.*, *Nat. Nanotechnol.* **2012**, *7*, 227.

[20] Y. Sugimoto, P. Pou, *et al.*, *Phys. Rev. B* **2006**, *73*, 205329.

[21] M. Ternes, C. P. Lutz, *et al.*, *Science* **2008**, *319*, 1066.

[22] J. Welker, F. J. Giessibl, *Science* **2012**, *336*, 444.

[23] T. Kunstmann, *Phys. Rev. B* **2005**, *71*, 121403.

[24] S. Ido, K. Kimura, *et al.*, *ACS Nano* **2013**, *7*, 1817.

[25] T. Uchihashi, R. Iino, *et al.*, *Science* **2011**, *333*, 755.

[26] N. Kodera, D. Yamamoto, *et al.*, *Nature* **2010**, *468*, 72.

[27] A. M. Baró, R. G. Reifenberger, *Atomic Force Microscopy in Liquid*, 1st ed., Wiley-VCH, Weinheim, Germany, **2012**.

[28] B. Bhushan, *Nanotribology and Nanomechanics: An Introduction*, 2nd ed., Springer, Heidelberg, Germany, **2008**.

[29] F. J. Giessibl, *Rev. Mod. Phys.* **2003**, *75*, 949.

[30] M. Binggeli, G. Kotrotsios, *et al.*, *Rev. Sci. Instrum.* **1993**, *64*, 2888.

[31] M. Tortonese, R. C. Barrett, *et al.*, *Appl. Phys. Lett.* **1993**, *62*, 834.

[32] F. J. Giessibl, *Appl. Phys. Lett.* **1998**, *73*, 3956.

[33] G. Meyer, N. M. Amer, *Appl. Phys. Lett.* **1988**, *53*, 1045.

[34] K. Kobayashi, H. Yamada, *et al.*, *Rev. Sci. Instrum.* **2009**, *81*, 43708.

[35] T. Fukuma, M. Kimura, *et al.*, *Rev. Sci. Instrum.* **2005**, *76*, 53704.

[36] A. Putnis, *Science* **2014**, *343*, 1441.

[37] G. E. Brown, *Science* **2001**, *294*, 67.

[38] S. Mann, D. D. Archibald, *et al.*, *Science* **1993**, *261*, 1286.

[39] F. C. Meldrum, *Int. Mater. Rev.* **2003**, *48*, 187.

[40] J. J. de Yoreo, Gilbert, Pupa U. P. A., *et al.*, *Science* **2015**, *349*, aaa6760.

[41] B. W. Ninham, T. T. Duignan, *et al.*, *Curr. Opin. Coll. Interface Sci.* **2011**, *16*, 612.

[42] F. J. Giessibl, *Phys. Rev. B* **1997**, *56*, 16010.

[43] J. N. Israelachvili, *Intermolecular and surface forces*, 3rd ed, Academic Press, Burlington, United States, **2011**.

[44] P. Debye, E. Hückel, *Phys. Z.* **1923**, *24*, 185.

[45] M. Gouy, *J. Phys. Theor. Appl.* **1910**, *9*, 457.

[46] D. L. Chapman, *Philos. Mag. 6* **1913**, *25*, 475.

[47] R. García, *Amplitude Modulation Atomic Force Microscopy*, 1st ed., Wiley-VCH, Weinheim, Germany, **2010**.

[48] K. Kimura, S. Ido, *et al.*, *J. Chem. Phys.* **2010**, *132*, 194705.

[49] D. J. Müller, D. Fotiadis, *et al.*, *Biophys. J* . **1999**, *76*, 1101.

[50] I. Y. Sokolov, G. S. Henderson, *et al.*, *Appl. Phys. Lett.* **1997**, *70*, 844.

[51] D. F. Parsons, M. Bostrom, *et al.*, *Phys. Chem. Chem. Phys.* **2011**, *13*, 12352.

[52] B. Kim, S. Kwon, *et al.*, *Sci. Rep.* **2014**, *4*, 6499.

[53] V. A. Parsegian, T. Zemb, *Curr. Opin. Coll. Interface Sci.* **2011**, *16*, 618.

[54] J. Israelachvili, H. Wennerström, *Nature* **1996**, *379*, 219.

[55] K. Voïtchovsky, J. J. Kuna, *et al.*, *Nat. Nanotechnol.* **2010**, *5*, 401.

[56] R. G. Horn, J. N. Israelachvili, *J. Chem. Phys.* **1981**, *75*, 1400.

[57] S. J. O'Shea, M. E. Welland, *et al.*, *Appl. Phys. Lett.* **1992**, *60*, 2356.

[58] S. J. O'Shea, M. E. Welland, *Langmuir* **1998**, *14*, 4186.

[59] S. Jeffery, P. M. Hoffmann, *et al.*, *Phys. Rev. B* **2004**, *70*, 54114.

[60] P. Hoffmann, S. Jeffery, *et al.*, *Phys. Rev. Lett.* **2001**, *87*, 24.

[61] T. Uchihashi, M. J. Higgings, *et al.*, *Appl. Phys. Lett.* **2004**, *85*, 3575.

[62] T. Uchihashi, M. Higgins, *et al.*, *Nanotechnology* **2005**, *16*, S49.

[63] G. B. Kaggwa, J. I. Kilpatrick, *et al.*, *Appl. Phys. Lett.* **2008**, *93*, 11909.

[64] A. Maali, T. Cohen-Bouhacina, *et al.*, *Phys. Rev. Lett.* **2006**, *96*, 86105.

[65] S. J. A. de Beer, D. van den Ende, *et al.*, *Nanotechnology* **2010**, *21*, 325703.

[66] K. Ueno, M. Kasuya, *et al.*, *Phys. Chem. Chem. Phys.* **2010**, *12*, 4066.

[67] S. J. A. de Beer, W. K. d. Otter, *et al.*, *EPL* **2012**, *97*, 46001.

[68] K. Kočevar, R. Blinc, *et al.*, *Phys. Rev. E* **2000**, *62*, R3055.

[69] E. T. Herruzo, H. Asakawa, *et al.*, *Nanoscale* **2013**, *5*, 2678.

[70] T. Fukuma, Y. Ueda, *et al.*, *Phys. Rev. Lett.* **2010**, *104*, 16101.

[71] M. Watkins, A. L. Shluger, *Phys. Rev. Lett.* **2010**, *105*, 196101.

[72] M. Watkins, M. L. Berkowitz, *et al.*, *Phys. Chem. Chem. Phys.* **2011**, *13*, 12584.

[73] B. Reischl, M. Watkins, *et al.*, *J. Chem. Theory Comput.* **2013**, *9*, 600.

[74] M. Harada, M. Tsukada, *Phys. Rev. B* **2010**, *82*, 35414.

[75] M. Watkins, B. Reischl, *J. Chem. Phys.* **2013**, *138*, 154703.

[76] Y. Martin, C. C. Williams, *et al.*, *J. Appl. Phys.* **1987**, *61*, 4723.

[77] T. R. Albrecht, P. Grütter, *et al.*, *J. Appl. Phys.* **1991**, *69*, 668.

[78] T. Fukuma, J. I. Kilpatrick, *et al.*, *Rev. Sci. Instrum.* **2006**, *77*, 123703.

[79] H. Hölscher, U. D. Schwarz, *Int. J. Non Linear Mech.* **2007**, *42*, 608.

[80] N. A. Burnham, O. P. Behrend, *et al.*, *Nanotechnology* **1997**, *8*, 67.

[81] F. Ohnesorge, G. Binnig, *Science* **1993**, *260*, 1451.

[82] K. Schröter, A. Petzold, *et al.*, *Macromol.* **2009**, *42*, 1114.

[83] J. P. Cleveland, S. Manne, *et al.*, *Rev. Sci. Instrum.* **1993**, *64*, 403.

[84] J. E. Sader, I. Larson, *et al.*, *Rev. Sci. Instrum.* **1995**, *66*, 3789.

[85] C. A. van Eysden, J. E. Sader, *J. Appl. Phys.* **2006**, *100*, 114916.

[86] R. W. Stark, W. M. Heckl, *Surf. Sci.* **2000**, *457*, 219.

[87] E. I. Green, *American Scientist* **1955**, *43*, 584.

[88] B. Gotsmann, C. Seidel, *et al.*, *Phys. Rev. B* **1999**, *60*, 11051.

[89] S. N. Magonov, V. Elings, *et al.*, *Surf. Sci.* **1997**, *375*, L385.

[90] J. Tamayo, R. García, *Appl. Phys. Lett.* **1997**, *71*, 2394.

[91] M.-h. Whangbo, G. Bar, *et al.*, *Surf. Sci. Lett.* **1998**, *411*, 794.

[92] J. P. Cleveland, B. Anczykowski, *et al.*, *Appl. Phys. Lett.* **1998**, *72*, 2613.

[93] B. Anczykowski, B. Gotsmann, *et al.*, *Appl. Surf. Sci.* **1999**, *140*, 376.

[94] J. Tamayo, R. García, *Appl. Phys. Lett.* **1998**, *73*, 2926.

[95] R. García, J. Tamayo, *et al.*, *Surf. Interface Anal.* **1999**, *27*, 312.

[96] S. Santos, K. R. Gadelrab, *et al.*, *Nanotechnology* **2012**, *23*, 125401.

[97] H. Hölscher, *Appl. Phys. Lett.* **2006**, *89*, 123109.

[98] M. Lee, W. Jhe, *Phys. Rev. Lett.* **2006**, *97*, 36104.

[99] A. J. Katan, M. H. van Es, *et al.*, *Nanotechnology* **2009**, *20*, 165703.

[100] A. F. Payam, D. Martin-Jimenez, *et al.*, *Nanotechnology* **2015**, *26*, 185706.

[101] H. Hölscher, B. Gotsmann, *et al.*, *Phys. Rev. B* **2001**, *64*, 75402.

[102] P. Rahe, R. Bechstein, *et al.*, *Phys. Rev. B* **2008**, *77*, 195410.

[103] J. E. Sader, S. P. Jarvis, *Appl. Phys. Lett.* **2004**, *84*, 1801.

[104] F. J. Giessibl, *Appl. Phys. Lett.* **2001**, *78*, 123.

[105] C. Loppacher, R. Bennewitz, *et al.*, *Phys. Rev. B* **2000**, *62*, 13674.

[106] R. García, R. Pérez, *Surf. Sci. Rep.* **2002**, *47*, 197.

[107] S. Morita, F. J. Giessibl, *et al.*, *Noncontact Atomic Force Microscopy: Volume 2*, 1st ed., Springer, Heidelberg, Germany, **2009**.

[108] W. A. Hofer, A. S. Foster, *et al.*, *Rev. Mod. Phys.* **2003**, *75*, 1287.

[109] P. K. Hansma, J. P. Cleveland, *et al.*, *Appl. Phys. Lett.* **1994**, *64*, 1738.

[110] T. E. Schäffer, Cleveland, J. P., *et al.*, *J. Appl. Phys.* **1996**, *80*, 3622.

[111] A. Labuda, K. Kobayashi, *et al.*, *Aip Advances* **2011**, *1*, 22136.

[112] P. E. Hillner, S. Manne, *et al.*, *Ultramicroscopy* **1992**, *42*, 1387.

[113] K.-i. Umeda, N. Oyabu, *et al.*, *Appl. Phys. Express* **2010**, *3*, 65205.

[114] N. Umeda, S. Ishizaki, *et al.*, *J. Vac. Sci. Technol. B* **1991**, *9*, 1318.

[115] G. C. Ratcliff, D. A. Erie, *et al.*, *Appl. Phys. Lett.* **1998**, *72*, 1911.

[116] A. Labuda, K. Kobayashi, *et al.*, *Rev. Sci. Instrum.* **2012**, *83*, 53703.

[117] C. Carrasco, P. Ares, *et al.*, *Rev. Sci. Instrum.* **2008**, *79*, 126106.

[118] A. Schwarz, H. Hölscher, *et al.*, *AIP Conf. Proc.* **2003**, *696*, 68.

[119] M. Z. Baykara, T. C. Schwendemann, *et al.*, *Adv. Mater.* **2010**, *22*, 2838.

[120] B. J. Albers, T. C. Schwendemann, *et al.*, *Nanotechnology* **2009**, *20*, 264002.

[121] H. Hölscher, S. M. Langkat, *et al.*, *Appl. Phys. Lett.* **2002**, *81*, 4428.

[122] Y. Sugimoto, T. Namikawa, *et al.*, *Phys. Rev. B* **2008**, *77*, 195424.

[123] K. Ruschmeier, A. Schirmeisen, *et al.*, *Nanotechnology* **2009**, *20*, 26.

[124] K. Ruschmeier, A. Schirmeisen, *et al.*, *Phys. Rev. Lett.* **2008**, *101*, 15.

[125] A. Schirmeisen, D. Weiner, *et al.*, *Phys. Rev. Lett.* **2006**, *97*, 13.

[126] M. Heyde, G. H. Simon, *et al.*, *Appl. Phys. Lett.* **2006**, *89*, 263107.

[127] M. Ashino, D. Obergfell, *et al.*, *Nanotechnology* **2009**, *20*, 26.

[128] B. J. Albers, T. C. Schwendemann, *et al.*, *Nat. Nanotechnol.* **2009**, *4*, 307.

[129] P. Rahe, J. Schütte, *et al.*, *Rev. Sci. Instrum.* **2011**, *82*, 63704.

[130] T. Hiasa, K. Kimura, *et al.*, *J. Phys. Chem. C* **2010**, *114*, 21423.

[131] K. Suzuki, N. Oyabu, *et al.*, *Appl. Phys. Express* **2011**, *4*, 125102.

[132] R. Nishioka, T. Hiasa, *et al.*, *J. Phys. Chem. C* **2013**, *117*, 2939.

[133] T. Hiasa, K. Kimura, *et al.*, *Phys. Chem. Chem. Phys.* **2012**, *14*, 8419.

[134] K. Suzuki, K. Kobayashi, *et al.*, *J. Chem. Phys.* **2014**, *140*, 54704.

[135] H. Asakawa, S. Yoshioka, *et al.*, *ACS Nano* **2012**, *6*, 9013.

[136] T. Fukuma, M. J. Higgins, *et al.*, *Biophys. J* . **2007**, *92*, 3603.

[137] T. Hiasa, K. Kimura, *et al.*, *J. Phys. Chem. C* **2012**, *116*, 26475.

[138] T. Hiasa, K. Kimura, *et al.*, *Colloids Surf. A* **2012**, *396*, 203.

[139] J. P. Dunne, B. Hales, *et al.*, *Global Biogeochem. Cycles* **2012**, *26*, GB3023.

[140] A. Khusainova, S. M. Nielsen, *et al.*, *J. Pet. Sci. Eng.* **2015**, *127*, 53.

[141] S. L. S. Stipp, C. M. Eggleston, *et al.*, *Geochim. Cosmochim. Acta* **1994**, *58*, 3023.

[142] J. Schütte, P. Rahe, *et al.*, *Langmuir* **2010**, *26*, 8295.

[143] A. L. Rachlin, G. S. Henderson, *et al.*, *Am. Mineral.* **1992**, *77*, 904.

[144] G. Raina, R. W. Gauldie, *et al.*, *Ferroelectr. Lett. Sect.* **1994**, *17*, 65.

[145] Y. Liang, A. S. Lea, *et al.*, *Surf. Sci.* **1996**, *351*, 172.

[146] D. L. Graf, *Am. Mineral.* **1961**, *46*, 283.

[147] P. Geissbühler, P. Fenter, *et al.*, *Surf. Sci.* **2004**, *573*, 191.

[148] P. Fenter, N. C. Sturchio, *Geochim. Cosmochim. Acta* **2012**, *97*, 58.

[149] F. Heberling, T. P. Trainor, *et al.*, *J. Colloid Interface Sci.* **2011**, *354*, 843.

[150] H. Imada, K. Kimura, *et al.*, *Chem. Phys.* **2013**, *419*, 193.

[151] K. Kobayashi, N. Oyabu, *et al.*, *J. Chem. Phys.* **2013**, *138*, 184704.

[152] D. S. Wastl, M. Judmann, *et al.*, *ACS Nano* **2015**, *9*, 3858.

[153] S. Kerisit, S. C. Parker, *Chem. Commun.* **2004**, 52.

[154] T. D. Perry, R. T. Cygan, *et al.*, *Geochim. Cosmochim. Acta* **2007**, *71*, 5876.

[155] P. Raiteri, J. D. Gale, *et al.*, *J. Phys. Chem. C* **2010**, *114*, 5997.

[156] P. Fenter, S. Kerisit, *et al.*, *J. Phys. Chem. C* **2013**, *117*, 5028.

[157] T. Fukuma, *Sci. Technol. Adv. Mater.* **2010**, *11*, 33003.

[158] J. E. Bresenham, *IBM Syst. J.* **1965**, *4*, 25.

[159] J. Lübbe, M. Temmen, *et al.*, *Beilstein J. Nanotechnol.* **2013**, *4*, 227.

[160] P. Rahe, PhD thesis, The Calcite (10-14) Surface: A Versatile Substrate for Molecular Self-Assembly, Johannes Gutenberg-Universität Mainz, **2011**.

[161] S. Kuhn, M. Kittelmann, *et al.*, *Phys. Rev. B* **2014**, *90*, 195405.

[162] P. Rahe, R. Bechstein, *et al.*, *J. Vac. Sci. Technol. B* **2010**, *28*, C4E31.

[163] D. Nečas, P. Klapetek, *Cent. Eur. J. Phys.* **2011**, *10*, 181.

[164] M. X. Jin, E. Shimada, *et al.*, *J. Ceram. Soc. Jpn.* **1999**, *107*, 1166.

[165] A. S. Foster, C. Barth, *et al.*, *Phys. Rev. Lett.* **2001**, *86*, 2373.

[166] A. Labuda, K. Kobayashi, *et al.*, *Phys. Rev. Lett.* **2013**, *110*, 66102.

[167] S. Kawai, T. Glatzel, *et al.*, *Phys. Rev. B* **2009**, *80*, 85422.

[168] S.-H. Loh, S. P. Jarvis, *Langmuir* **2010**, *26*, 9176.

[169] A. E. Ingerson, *Geochim. Cosmochim. Acta* **1995**, *59*, 1217.

[170] J. A. Mckenzie, C. Vasconcelos, *Sedimentology* **2009**, *56*, 205.

[171] J. Xu, C. Yan, *et al.*, *PNAS* **2013**, *110*, 17750.

[172] L. S. Land, *Aquat. Geochem.* **1998**, *4*, 361.

[173] O. Liebermann, *Nature* **1967**, *213*, 241.

[174] N. H. de Leeuw, S. C. Parker, *Phys. Chem. Chem. Phys.* **2001**, *3*, 3217.

[175] P. Fenter, Z. Zhang, *et al.*, *Geochim. Cosmochim. Acta* **2007**, *71*, 566.

[176] R. W. Fairbridge in *Regional Aspects of Carbonate Deposition*, (Eds.: R. LeBlanc, J. Breeding), Spec. Publ.-SEPM, p. 125.

[177] C. M. Pina, C. Pimentel, *et al.*, *Surf. Sci.* **2010**, *604*, 1877.

[178] J. W. Morse, R. S. Arvidson, *Earth-Sci. Rev.* **2002**, *58*, 51.

[179] J. W. Morse, R. S. Arvidson, *et al.*, *Chem. Rev.* **2007**, *107*, 342.

[180] O. S. Pokrovsky, S. V. Golubev, *et al.*, *Chem. Geol.* **2005**, *217*, 239.

[181] D. W. Finneran, J. W. Morse, *Chem. Geol.* **2009**, *268*, 137.

[182] D. K. Gledhill, J. W. Morse, *Geochim. Cosmochim. Acta* **2006**, *70*, 5802.

[183] A. L. McEvoy, F. Stevens, *et al.*, *Langmuir* **2006**, *22*, 6931.

[184] A. J. Gratz, P. E. Hillner, *et al.*, *Geochim. Cosmochim. Acta* **1993**, *57*, 491.

[185] S. R. Higgins, G. Jordan, *et al.*, *Geochim. Cosmochim. Acta* **2002**, *66*, 3201.

[186] O. S. Pokrovsky, J. Schott, *et al.*, *Geochim. Cosmochim. Acta* **1999**, *63*, 3133.

[187] H. E. King, C. V. Putnis, *Geochim. Cosmochim. Acta* **2013**, *109*, 113.

[188] M. Urosevic, C. Rodriguez-Navarro, *et al.*, *Geochim. Cosmochim. Acta* **2012**, *80*, 1.

[189] S. R. Higgins, X. Hu, *Geochim. Cosmochim. Acta* **2005**, *69*, 2085.

[190] E. Ruiz-Agudo, M. Urosevic, *et al.*, *Chem. Geol.* **2011**, *281*, 364.

[191] P. Fenter, P. Geissbühler, *et al.*, *Geochim. Cosmochim. Acta* **2000**, *64*, 1221.

[192] T. Fukuma, B. Reischl, *et al.*, *Phys. Rev. B* **2015**, *92*, 155412.

[193] K. Wright, R. T. Cygan, *et al.*, *Phys. Chem. Chem. Phys.* **2001**, *3*, 839.

[194] S. Kawai, C. M. Pina, *et al.*, *Nanotechnology* **2013**, *24*, 55702.

[195] C. Marutschke, P. Spijker, *et al.*, *in preparation*.

[196] S. Plimpton, *J. Comp. Phys.* **1995**, *117*, 1.

[197] W. Humphrey, A. Dalke, *et al.*, *J. Mol. Graphics* **1996**, *14*, 33.

[198] N. Michaud-Agrawal, E. J. Denning, *et al.*, *J. Comp. Chem.* **2011**, *32*, 2319.

[199] H. Tomono, H. Nada, *et al.*, *J. Phys. Chem. B* **2013**, *117*, 14849.

[200] Y. Wu, H. L. Tepper, *et al.*, *J. Chem. Phys.* **2006**, *124*, 24503.

[201] J. L. Neff, M. Kittelmann, *et al.*, *Phys. Chem. Chem. Phys.* **2014**, *16*, 15437.

[202] M. Kittelmann, M. Nimmrich, *et al.*, *J. Phys. Chem. C* **2013**, *117*, 23868.

[203] C. M. Hauke, R. Bechstein, *et al.*, *ACS Nano* **2013**, *7*, 5491.

[204] F. Kling, M. Kittelmann, *et al.* in *Advances in Atom and Single Molecule Machines*, (Eds.: P. Moriarty, S. Gauthier), in press.

[205] M. Schreiber, M. Eckardt, *et al.*, *Soft Matter* **2013**, *9*, 7145.

[206] C. A. Orme, A. Noy, *et al.*, *Nature* **2001**, *411*, 775.

[207] I. S. Pasarín, M. Yang, *et al.*, *Langmuir* **2011**, *28*, 2545.

[208] N. Bovet, M. Yang, *et al.*, *Phys. Chem. Chem. Phys.* **2015**, *17*, 3490.

[209] K. K. Sand, S. L. S. Stipp, *et al.*, *Mineral. Mag.* **2008**, *72*, 353.

[210] D. J. Cooke, R. J. Gray, *et al.*, *Langmuir* **2010**, *26*, 14520.

[211] K. K. Sand, M. Yang, *et al.*, *Langmuir* **2010**, *26*, 15239.

[212] H. Imada, K. Kimura, *et al.*, *Langmuir* **2013**, *29*, 10744.

[213] C. Marutschke, P. Spijker, *et al.*, *in preparation*.

[214] Keller, K. S., Olsson, M. H. M., *et al.*, *Langmuir* **2015**, *31*, 3847.

[215] L. Zimmerli, S. Maier, *et al.*, *J. Phys.: Conf. Ser.* **2007**, *61*, 1357.

[216] J. M. Mativetsky, S. A. Burke, *et al.*, *Small* **2007**, *3*, 818.

[217] M. Fendrich, T. Kunstmann, *Appl. Phys. Lett.* **2007**, *91*, 23101.

[218] S. Maier, L.-A. Fendt, *et al.*, *Small* **2008**, *4*, 1115.

[219] O. Pakarinen, J. Mativetsky, *et al.*, *Phys. Rev. B* **2009**, *80*, 085401.

[220] A. Hinaut, A. Pujol, *et al.*, *Beilstein J. Nanotechnol.* **2012**, *3*, 221.

[221] J. M. Mativetsky, S. A. Burke, *et al.*, *Nanotechnology* **2007**, *18*, 105303.

[222] B. Such, T. Trevethan, *et al.*, *ACS Nano* **2010**, *4*, 3429.

[223] A. Hinaut, K. Lekhal, *et al.*, *J. Phys. Chem. C* **2011**, *115*, 13338.

[224] S. A. Burke, J. M. LeDue, *et al.*, *Adv. Mater.* **2009**, *21*, 2029.

[225] S. Fremy, A. Schwarz, *et al.*, *Nanotechnology* **2009**, *20*, 405608.

[226] M. Körner, F. Loske, *et al.*, *Phys. Rev. Lett.* **2011**, *107*, 016101.

[227] J. Schütte, R. Bechstein, *et al.*, *Phys. Rev. B* **2009**, *80*, 205421.

[228] P. Rahe, R. Lindner, *et al.*, *Phys. Chem. Chem. Phys.* **2012**, *14*, 6544.

[229] P. Rahe, M. Nimmrich, *et al.*, *Small* **2012**, *8*, 2968.

[230] R. Momper, bachelor thesis, Einfluss des pH-Werts auf die Komplexbildung von Farbstoffmolekülen auf Calcitoberflächen, Johannes Gutenberg-Universität Mainz, **2014**.

[231] M. Nalbach, diploma thesis, Untersuchung der Wechselwirkungen zwischen Dihydroxybenzoesäuren und Kalziumkarbonat in Flüssigkeiten, Johannes Gutenberg-Universität Mainz, **2014**.

[232] H. Söngen, bachelor thesis, Molecular self-assembly of Alizarin Red S on dolomite and magnesite in aqueous solution, Johannes Gutenberg-Universität Mainz, **2015**.

[233] R. Momper, M. Nalbach, *et al.*, *Langmuir* **2015**, *31*, 7283.

[234] G. M. Friedman, *J. Sediment. Petrol.* **1959**, *29*, 87.

[235] H. E. Zittel, T. M. Florence, *Anal. Chem.* **1967**, *39*, 320.

[236] A. Holmgren, L. Wu, *et al.*, *Spectrochim. Acta Part A* **1999**, *55*, 1721.

[237] V. M. Ivanov, E. M. Adamova, *et al.*, *J. Anal. Chem.* **2010**, *65*, 473.

[238] A. Turcanu, T. Bechtold, *Dyes Pigm.* **2011**, *91*, 324.

[239] N. Moll, L. Gross, *et al.*, *New J. Phys.* **2010**, *12*, 125020.

[240] R. S. Weis, T. K. Gaylord, *Appl. Phys. A* **1985**, *37*, 191.

[241] K.-K. Wong, *Properties of lithium niobate*, 1st ed., INSPEC/IEE, London, United Kingdom, **2002**.

[242] J. Krausslich, C. Dubs, *et al.*, *Phys. Stat. Sol. (a)* **2007**, *204*, 2585.

[243] L. Arizmendi, *Phys. Stat. Sol. (a)* **2004**, *201*, 253.

[244] T. Kishino, R. F. Tavlykaev, *et al.*, *Appl. Phys. Lett.* **2000**, *76*, 3852.

[245] H. Junhui, Y. Zhizhen, *Chin. Sci. Bull.* **2003**, *48*, 2290.

[246] P. Franken, A. Hill, *et al.*, *Phys. Rev. Lett.* **1961**, *7*, 118.

[247] L. Gui, H. Hu, *et al.*, *Opt. Express* **2009**, *17*, 3923.

[248] L. Y. Yeo, J. R. Friend, *Biomicrofluidics* **2009**, *3*, 12002.

[249] K. Nassau, H. J. Levinstein, *et al.*, *J. Phys. Chem. Solids* **1966**, *27*, 983.

[250] J. R. Carruthers, *J. Appl. Phys.* **1971**, *42*, 1846.

[251] R. L. Byer, J. F. Young, *et al.*, *J. Appl. Phys.* **1970**, *41*, 2320.

[252] K. Kitamura, Y. Furukawa, *et al.*, *J. Appl. Phys.* **1997**, *82*, 1006.

[253] N. Zotov, H. Boysen, *et al.*, *J. Phys. Chem. Solids* **1994**, *55*, 145.

[254] H. Donnerberg, Tomlinson, S. M., *et al.*, *Phys. Rev. B* **1989**, *40*, 11909.

[255] K. Kitamura, J. K. Yamamoto, *et al.*, *J. Cryst. Growth* **1992**, *116*, 327.

[256] P. F. Bordui, R. G. Norwood, *et al.*, *J. Appl. Phys.* **1992**, *71*, 875.

[257] R. Hsu, E. N. Maslen, *et al.*, *Acta Cryst. B* **1997**, *53*, 420.

[258] O. F. Schirmer, O. Thiemann, *et al.*, *J. Phys. Chem. Solids* **1991**, *52*, 185.

[259] W. E. Story, *Am. J. Math.* **1878**, *1*, 177.

[260] C. Canalias, V. Pasiskevicius, *Nat. Photon.* **2007**, *1*, 459.

[261] Y. Yun, E. I. Altman, *J. Am. Chem. Soc.* **2007**, *129*, 15684.

[262] H. D. Megaw, *Acta Cryst. A* **1968**, *24*, 583.

[263] S. Sanna, R. Hölscher, *et al.*, *Appl. Surf. Sci.* **2014**, *301*, 70.

[264] H. Nagata, K. Shima, *et al.*, *J. Am. Ceram. Soc.* **1997**, *80*, 1203.

[265] A. Saito, H. Matsumoto, *et al.*, *Jpn. J. Appl. Phys.* **2004**, *43*, 2057.

[266] K. Tabata, T. Choso, *et al.*, *Surf. Sci.* **1998**, *402*, 487.

[267] E. V. Rakova, *Surf. Sci.* **1993**, *287*, 400.

[268] B. Rosenblum, *Appl. Phys. Lett.* **1974**, *25*, 17.

[269] Y. Yun, L. Kampschulte, *et al.*, *J. Phys. Chem. C* **2007**, *111*, 13951.

[270] G. G. Bentini, M. Bianconi, *et al.*, *J. Appl. Phys.* **2002**, *92*, 6477.

[271] T.-C. Lee, J.-T. Lee, *et al.*, *Appl. Phys. Lett.* **2003**, *82*, 191.

[272] S. Sanna, W. G. Schmidt, *et al.*, *Phys. Rev. B* **2014**, *89*, 075403.

[273] K. Kobayashi, H. Yamada, *et al.*, *Rev. Sci. Instrum.* **2001**, *72*, 4383.

[274] D. Kiracofe, K. Kobayashi, *et al.*, *Rev. Sci. Instrum.* **2011**, *82*, 13702.

[275] G. Lee, *Opt. Express* **2002**, *10*, 556.

[276] M. Ricci, P. Spijker, *et al.*, *Langmuir* **2013**, *29*, 2207.

List of Figures

List of Acronyms

1D one-dimensional
2D two-dimensional
3D three-dimensional

AFM atomic force microscopy
AM amplitude modulated
AM-AFM amplitude modulation atomic force microscopy
ARC Asylum Research Controller
ARS Alizarin Red S
ATC Air Temperature Control

dAFM dynamic atomic force microscopy
DFT density function theory
DLVO Derjaguin-Landau-Verwey-Overbeek
DNA deoxyribonucleic acid

EDL electrostatic double layer

FDC force-distance curve
FFT Fast Fourier transformation
FM frequency modulated
FM-AFM frequency modulation atomic force microscopy

InvOLS inverse optical lever sensitivity
IUPAC International Union of Pure and Applied Chemistry

LN lithium niobate
LVDT linear variable displacement transformer

MD molecular dynamics

NC-AFM non-contact atomic force microscopy

PLL phase-locked loop
PM phase modulated
PSD position sensitive photo diode

sAFM static atomic force microscopy
SAW surface acoustic wave
SFA surface force apparatus
SLN stoichiometric lithium niobate
SNR signal to noise ratio
SPM scanning probe microscopy
STM scanning tunnelling microscopy

UHV ultra high vacuum

vdW van-der-Waals

XPS X-ray photoelectron spectroscopy
XR X-ray reflectivity

Acknowledgements

An dieser Stelle möchte ich mich bei allen Menschen bedanken, die es mir ermöglicht haben, diese Arbeit zu schreiben und mich bei der Promotion unterstützt haben.

[Removed to protect privacy]

Publications & Presentations

Publications in Peer-reviewed Journals

S. Sanna, S. Rode, R. Hölscher, S. Klassen, C. Marutschke, K. Kobayashi, H. Yamada, W. G. Schmidt and A. Kühnle
Charge compensation by long-period reconstruction in strongly polar lithium niobate surfaces
Phys. Rev. B 88 (2013) 115422

C. Marutschke, D. Walters, J. Cleveland, I. Hermes, R. Bechstein and A. Kühnle
Three-dimensional hydration layer mapping on the (104) surface of calcite using amplitude modulation atomic force microscopy
Nanotechnology 25 (2014) 335703

C. Marutschke, P. Spijker, I. Hermes, R. Bechstein, S. Klassen, J. Tracey, A.S. Foster, A. Kühnle
Arrangement of Interfacial Water: The Impact of Lattice Dimensions on the Water Network Structure on Naturally Omnipresent Carbonate Surfaces
in preparation

C. Marutschke, P. Spijker, I. Hermes, R. Bechstein, S. Klassen, J. Tracey, A.S. Foster, A. Kühnle
Structure of different alcohols on calcite probed by high-resolution amplitude modulation atomic force microscopy
in preparation

Talks

C. Marutschke, D. Walters, J. Cleveland and A. Kühnle
2D mapping on the (104) surface of calcite
4th International Workshop on Advanced Atomic Force Microscopy Techniques, 2013, Karlsruhe

C. Marutschke, D. Walters I. Hermes, J. Cleveland and A. Kühnle
Three-dimensional mapping on the (104) surface of calcite
4th Euro AFM Forum, 2014, Göttingen

C. Marutschke, D. Walters I. Hermes, J. Cleveland and A. Kühnle
Three-dimensional mapping on the (104) surface of calcite
Physics Boat Workshops, 2014, Helsinki/Stockholm

Poster Presentations

S. Rode, S. Klassen, C. Marutschke, K. Kobayashi, H. Yamada, R. Hölscher, S. Sanna, W. G. Schmidt, A. Kühnle
Atomic-Resolution in aqueous solution of the polar (0001) and (000-1) surfaces of Lithium Niobate by frequency modulates atomic force microscopy
15th NC-AFM conference, 2012, Czech republic

C. Marutschke, D. Walters I. Hermes, J. Cleveland and A. Kühnle
Three-dimensional hydration layer mapping on the (104) surface of calcite using amplitude modulation atomic force microscopy
15th NC-AFM conference, 2014, Japan

C. Marutschke, D. Walters I. Hermes, J. Cleveland and A. Kühnle
Three-dimensional hydration layer mapping on the (104) surface of calcite using amplitude modulation atomic force microscopy
563rd Wilhelm and Else Heraeus-Seminar, 2014, Germany

Curriculum Vitae (educational)

[Removed to protect privacy]

Colophon

This thesis was typeset with LaTeX 2_ε. It uses the *Clean Thesis* style developed by Ricardo Langner. The design of the *Clean Thesis* style is inspired by user guide documents from Apple Inc.

Download the *Clean Thesis* style at `http://cleanthesis.der-ric.de/`.